©Copyright 2022
Xiaotian Shi

Topological States in Ordered and Disordered Mechanical Metamaterial

Xiaotian Shi

A dissertation
submitted in partial fulfillment of the
requirements for the degree of

Doctor of Philosophy

University of Washington

2022

Reading Committee:

Jinkyu Yang, Chair

Marco Salviato

Jiun-Haw Chu

Program Authorized to Offer Degree:

Aeronautics and Astronautics

University of Washington

Abstract

Topological States in Ordered and Disordered Mechanical Metamaterial

Xiaotian Shi

Chair of the Supervisory Committee:
Jinkyu Yang
Department of Aeronautics and Astronautics

Topological mechanical metamaterials have emerged as an active research field with the rapid development of topological phases in condensed matter physics. By incorporating robust topological features and highly customizable nature, topological mechanical metamaterials offer unprecedented power to manipulate acoustic and elastic waves and show great potential in a variety of engineering applications, such as low-loss devices, high-precision sensors, and quantum information processing. In this dissertation, we explore the topological phases in ordered three-dimensional (3D) mechanical metamaterials and investigate the disorder induced topological phase transition in both one-dimensional (1D) and two-dimensional (2D) mechanical metamaterials. First, we design an elastic structure made of beam elements with $AA-$stacked honeycomb lattice. The chiral interlayer couplings induce Weyl points with opposite topological charges (± 1) in the bulk bands. We also demonstrate the elastic Fermi arcs, and topologically protected surface states through full-scale numerical simulations. Then, we proposed a chiral phononic crystal based on a 3D Lieb lattice that carries spin-1 Weyl points of topological charge ± 2. We observe special straight-type acoustic Fermi arcs and numerically demonstrate dual-band topologically protected and collimated surface waves in the spin-1 Weyl structure. Next, we investigate the interplay between topology and disorder in a 1D spring-mass chain. Three types of topological invariants defined in real space are implemented to characterize the topological properties in disordered 1D mechanical setups. Our findings reveal that disorder can both destroy and establish a topological state, depending on

the type and strength of the disorder. Finally, we extend the disorder study to 2D mechanical systems and demonstrate disorder induced topological phase transition in both discrete and continuous quantum spin Hall mechanical systems.

TABLE OF CONTENTS

LIST OF FIGURES

ACKNOWLEDGMENTS

First of all, I would like to express my deepest appreciation to Professor Jinkyu Yang for his constant encouragement and support throughout my doctoral study. Professor Yang, with his excellent professional ability and charming personality, has not only been a great advisor but a perfect role model. His understanding and recognition have been and will always be a great source of motivation for me to become a better version of myself. I would also like to thank my Ph.D. committee members, Prof. Marco Slaviato, Prof. Antonino Ferrante, Prof. Lucas R. Meza, and Prof. Jiun-Haw Chu, for their constructive comments and suggestions on my research.

I would like to extend my sincere thanks to all my collaborators, Prof. Feng Li, Prof. Kaiping Yu, Prof. Georgios Theocharis, Prof. Huaqing Huang, Prof. Rajesh Chaunsali, Prof. Ying Wu, Dr. Hyunryung Kim, Dr. Vassos Achilleos, Ioannis Kiorpelidis, Dr. Chun-Wei Chen, Timothy Gormley, and Shuaifeng Li. Special thanks go to Prof. Rui Zhu and all his students for their warm and generous hosting during my stay at the Beijing Institute of Technology due to the Covid-19 pandemic. This work couldn't have been possible without all your input.

It was my great pleasure to work with a group of talented colleagues and nice friends at the Laboratory for Engineered Materials and Structures (LEMS). I want to thank Dr. Hyunryung Kim for initiating me into the experiment work and Dr. Rajesh Chaunsali for your inspirational mentoring. I am also grateful to the lab members and visitors: Dr. Hiromi Yasuda, Dr. Seunghyun Ko, Dr. Chun-Wei Chen, James O'Neil, Tim Gormley, Shuaifeng Li, Yasuhiro Miyazawa, Koshiro Yamaguchi, Balakumaran Gopalarethinam, Qingqian Li, Rohith Jayaram, Kosei Tsujikawa, Dr. Gil-Yong Lee, Aman Thakkar, Dr. Yang Nan, Zhisong Chen, Kyle Johnson, Vicente Arroyos for all your kind support and friendly company.

Last but not least, I would like to thank my parents and my wife for their unconditional love

and support over these years. You are the only reason for my happiness.

DEDICATION

to my lovely family, my wife, Bryna, and my son, Miles

Chapter 1

INTRODUCTION

1.1 Metamaterial

Metamaterials are artificial materials that exhibit unique properties hard to find in nature. Once proposed, metamaterials have attracted great interest and shown tremendous potential in many disciplines of science and technology. They usually consist of periodically arranged building blocks (unit cells). Metamaterials obtain their special properties not from the properties of the constituting material but from their carefully designed internal structures. Such a feature gives us large freedom to tailor the properties of metamaterials, such as the geometry of the unit cell and the pattern of spacial arrangement. One of the pioneer studies on metamaterials is conducted by Veselago [1] in 1968, where the wave propagation in materials with simultaneously negative permeability and permittivity was discussed. It was not until about 30 years later Smith *et al*. [2] proposed and demonstrated the first composite material with double negative parameters in the microwave regime. Following the early work on electromagnetic waves, the studies of metamaterials start to spread to other classical wave systems including the optical [3], acoustic [4] and elastic waves [5].

Mechanical metamaterials have been designed to exhibit unusual material properties, such as negative Poison's ratio [6], negative effective modulus [7], effective density [8], and extreme compressibility [9]. This promises wide applications in manipulating acoustic and stress waves, including wave guiding [10, 11], noise/vibration reduction [12, 13], cloaking [14, 15], and energy harvesting [16, 17]. Particularly, inspired by the ground-breaking discovery of topological phases in condensed matter physics, a new class of mechanical metamaterial with nontrivial properties has become one of the most active r esearch areas [18].

1.2 Topology and topological band theory

Topology, which originated from mathematics, studies the intrinsic geometric properties that stay invariant under continuous deformations. That is, objects that belong to the same topological class can be transformed into each other by stretching, compressing, or smooth distorting. The most famous example to illustrate the concept of topology is that we can smoothly deform one sphere into an ellipsoid or a bowl but not a torus, since cutting and gluing are not allowed in this process. Actually, one can assign an integer number, a so-called topological invariant, to a certain space to character its topological property. In the case of sphere and torus, we can use the Genus g value to classify these two geometries, which is equal to the number of 'holes' in the object. Here, one can derive the Genus g value through Euler characteristic χ obtained by integrating the Gaussian curvature over a surface, given as:

$$\chi = \frac{1}{2\pi}\iint_S K\mathrm{d}A \tag{1.1}$$

$$g = 1 - \frac{\chi}{2} \tag{1.2}$$

Following Eq. 1.1, we can know that the genus values of a sphere and a torus are $g = 0$ and $g = 1$, respectively.

Later on, the idea of topology was introduced to solid-state physics to characterize the phase of matters. Quantum Hall effect (QHE) discovered in 1980 by Klitzing.*et al* [19] appeared to be the first topological phase, where conductance plateaus were observed in a two-dimensional electron gas in the presence of a strong perpendicular magnetic field. Such integer quantization of the Hall conductance was then successfully explained by the topological invariant, Chern number, and turned out to be topologically protected which remains unchanged by a small disorder in the sample. In analogue to Genus g of surface in real space, the Chern number characterizes the geometric phase of the energy bands in the momentum space, which can be calculated by integrating the Berry curvature over a surface in the Brillouin zone:

$$C = \frac{1}{2\pi} \iint_S F(\mathrm{k}) \mathrm{d}s \tag{1.3}$$

where $F(\mathrm{k}) = \nabla_{\mathrm{k}} \times A(\mathrm{k})$ is the Berry curvature and $A(\mathrm{k}) = i < u(\mathrm{k}) | \nabla_{\mathrm{k}} | u(\mathrm{k}) >$ is the Berry connection. Equation. 1.3 defines the Chern number of a particular band in the energy spectrum. To calculate the Chern number of the certain band gap, we can then sum the Chen numbers of all bands below the band gap. Although the Chen number is obtained purely from the bulk bands, it can tell us what is going on at the boundary through the bulk-edge correspondence [20]. The quantum Hall system with a non-zero Chern number supports a gapless edge state within the energy gap and carries the nondissipative unidirectional electric current at the edge of a finite size sample[21, 22].

Since then, the study of topological phases has taken the center stage in condensed matter physics. A series of novel topological states were discovered, such as quantum spin Hall Effect (QSHE) [23, 24, 25], quantum anomalous Hall Effect (QAHE) [26, 27, 28], quantum valley Hall effect (QVHE) [29], 3D topological insulator [30], and Weyl semimetals [31].

1.3 Topological Mechanical Metamaterial

The huge success of topological materials in condensed matter physics also sparks the explosion of explorations of topological phases in classical wave systems [32, 33, 34]. Bloch's theorem, which is the foundation of electronic band structures, can be adopted to calculate the frequency band structures of the classical wave metamaterials. This provides the theoretical basis for emulating topological materials to classical systems. However, there exist fundamental differences between electronic and classical wave systems. On the one hand, due to the lack of intrinsic spin and failure to respond to magnetic fields in classic waves, it usually requires extra effort to make an analogy to the electronic system. For example, zone folding mechanism [35] is introduced to construct pseudospin modes to demonstrate QSHE-like phenomenons. On the other hand, classical topological metamaterials can break the limitation of the Fermi level and thus easily take advantage of the whole frequency regime of the band structure without worrying about the filling ratio. In addi-

tion, thanks to the large scale in both time and space, experimental verifications in classical wave systems tend to be much more feasible. In this way, the topology study in classical systems goes beyond the simple generation of electronic counterparts and starts to broaden the understanding and impact of topological science.

In this dissertation, I focus on the topological mechanical metamaterials that support unprecedented acoustic and elastic wave phenomena. Specifically, this research addresses two major problems in current studies on topology and metamaterials in mechanical systems:

I. **Exploration of topological phases in ordered 3D mechanical metamaterial**. To date, most existing works on topological mechanical metamaterial are limited to lower dimensions. For example, my colleagues have reported topologically non-trivial band-gaps in a one-dimensional(1D) phononic crystal [36], topological Band Transition in 1D cylindrical granular chains [37], QVHE in a 2D Stewart Platform based structure [38], and pseudospin Hall effect for flexural waves in bolted plates [39, 40]. However, there is very little research studying the topological properties of 3D mechanical metamaterial. It is meaningful to extend the topology study to 3D and demonstrate many important topological physics effects. Particularly, the recent developments in advanced manufacturing technologies make it feasible to fabricate 3D structures with complex architectures, which promotes the applications of 3D topological mechanical metamaterials in the real world.

II. **Investigation on the effect of disorder in topological mechanical metamaterials**. Topological mechanical metamaterials have traditionally focused on perfect periodic structures, whose topological properties can be well explained by the topological band theory and are protected by certain symmetries in the system. However, disorders are ubiquitous in real structure due to manufacturing defects, which inevitably destroys the translational symmetry of the system. Therefore, it is important to understand the behavior of topological phases in the presence of disorders. Theoretically, topological phases are immune to weak disorders and can be suppressed when the disorder is strong enough to close the bulk band gaps. Besides destroying topological nature, a disorder induced topological phase, the so-called topological Anderson insulator [41, 42], attracts enormous interest to study the relationship between disorder and topology. Despite the tremendous efforts in electronic and photonic systems [41, 42, 43, 44, 45], its counterparts in mechanical systems remain

less explored.

1.4 Outline of the dissertation

In chapter 2, we design the 3D structure with the AA-stacked honeycomb lattice composed of only space beams and carries a pair of Weyl points, with topological charges ± 1, which can be successfully explained by the two-band Hamiltonian of AA-stacked graphene. We address a fundamental issue in topological elastic systems, which is to efficiently manipulate multiple wave modes that can coexist in the same system. With the help of the local resonance of the space beams, we can filter other modes and create a complete topological band gap for a certain k_z range. We numerically demonstrate the elastic Weyl points and surface arc states in the proposed 3D system. Here, we use the beam elements to model the elastic structure, since they have fewer degrees of freedom and are far more computationally efficient than the 3D solid elements, which thereby facilitates the Finite element analysis (FEA) simulation on the full-scale structure.

In chapter 3, we design a 3D chiral phononic crystal that supports spin-1 Weyl points by stacking up two-dimensional acoustic Lieb waveguides and introducing chiral interlayer couplings. The spin-1 Weyl points carry high order topological charges ±2, which can be successfully explained by the three band Hamiltonian of a tight-binding model with a 3D chiral Lieb lattice. We also numerically demonstrate the associated acoustic Fermi arcs and topological surface states in the proposed 3D system. The unique straight-type acoustic Fermi arcs indicate that we can simultaneously realize the robust one-way propagation and collimation effect of the acoustic waves within multiple frequency ranges in the structure.

In chapter 4, we design a spring-mass dimer chain with ground springs to explore the interplay between disorder and topology in a 1D mechanical system. We numerically investigate the topological phase transition induced purely by the disorder. Three kinds of real space topological invariants are calculated to characterize the topological properties in a disordered mechanical lattice. We demonstrate the bilateral topological phase transition by imposing disorder and realize a mechanical Topological Anderson Insulator. The critical boundary of topological transition is accurately highlighted by the localization length.

In chapter 5, we investigate the disorder induced topological phase transition in both discrete and continuous 2D quantum spin Hall (QSH) systems. We generalize the spin Bott index to a discrete mechanical setup, which can work as a topological invariant to characterize the topological properties in a disordered 2D mechanical lattice. We quantitatively demonstrate the disorder induced topological phase transition by monitoring the evolution of the spin Bott index with the increase of disorder strength. We verify the disorder induced topological phase transition in both discrete lattice and phononic crystal by comparing the pseudospin dependent topologically protected edge state along the interface between a disordered QSH insulator and a trivial insulator.

In chapter 6, we summarize the main findings of this research and give an outlook on potential future directions.

Chapter 2

ELASTIC WEYL POINTS AND SURFACE ARC STATES IN 3D STRUCTURES

The study of Weyl points in electronic systems has inspired many recent researches in classical systems such as photonic and acoustic lattices. Here we show how the Weyl physics can also inspire the design of novel elastic structures. We construct a single-phase 3D structure, an analogue of the AA-stacked honeycomb lattice, and predict the existence of Weyl points with opposite topological charges (± 1), elastic Fermi arcs, and the associated gapless topologically protected surface states. We employ full-scale numerical simulations on the elastic 3D structure and present a clear visualization of topological surface states that are directional and robust. Such designed lattices can pave the way for novel vibration control and energy harvesting on structures that are ubiquitous in many engineering applications.

2.1 Introduction

Phononic crystals and metamaterials have shown new and exciting ways to control the flow of wave propagation in the medium [46, 47, 48, 49]. Recently, the topology of band structures has emerged as a new design tool in this context. The essential idea is to characterize the bulk dispersion topologically and predict its implications on the edges/surfaces of the system. A nonzero topological invariant of the bulk usually implies the existence of edge or surface waves with nontrivial properties, such as directionality and robustness [50, 51, 20]. Several interesting strategies to manipulate elastic waves have thus been shown [52, 18]. However, the studies so far focused mainly on 1D and 2D systems. It is not clear how a 3D elastic structure could be designed to support topological surface states. What special characteristics those surface state would have and how they could be harnessed in engineering settings are some key questions. In this study, we attempt to address these

questions by taking inspiration from the Weyl physics.

Weyl semimetals [31, 53, 54, 55, 56] have recently attracted significant attention for their exotic features. In Weyl semimetals, the Weyl point refers to the degeneracy point of two bands having linear dispersion in all directions in the 3D reciprocal space. The effective Weyl Hamiltonian is, in general, given by $H(\mathbf{k}) = f(\mathbf{k})\sigma_0 + v_x k_x \sigma_x + v_y k_y \sigma_y + v_z k_z \sigma_z$, where $f(\mathbf{k})$ is an arbitrary real function, v_i, k_i, and σ_i represent group velocity, momentum, and Pauli matrix, respectively. Weyl points behave as the sources or the sinks of the Berry curvature in the reciprocal space. By integrating the Berry flux on a sphere surrounding a Weyl point, we can get the non-vanishing topological charge (or Chern number) associated with it [57]. The Weyl point is robust against small perturbations and cannot be easily gapped unless it is annihilated with another Weyl point with the opposite topological charge [58]. For electronic systems, previous researches have shown many unusual phenomena associated with Weyl points, such as robust surface states [31] and chiral anomaly [59]. Later on, the Weyl physics has shown to be useful in the classical systems of photonic [58, 60, 61, 62] and acoustic lattices [63, 64, 65, 66, 67, 68, 69].

The implementation of the Weyl physics in elastic structures, however, has been challenging so far. Recently, a self-assembled double gyroid structure that contains Weyl points for both electromagnetic and elastic waves was proposed [70]. Later, a design consisting of a thin plate and beams, which carries both Weyl and double-Weyl points, was also proposed [71]. In spite of these, the experimental demonstrations of elastic Weyl points remain elusive to date. Furthermore, there has not been even a study reporting full-scale numerical simulations in the elastic setting, by which the Weyl physics can be directly visualized and appreciated. This is due to the fact that such structures are extremely intricate to fabricate. At the same time, it is very demanding to computationally simulate their full-scale wave dynamics, because it involves with several types of elastic modes.

In this research, we design a 3D elastic lattice made entirely of beams, which allow both translational and rotational degrees of freedom along their length directions. We employ the finite element analysis (FEA) to obtain a dispersion diagram for the unit cell and discuss its topological features in relation to the Weyl physics. Inspired by widely used 3D hollow structures in engineering, e.g., fuselage, we construct a full-scale hollow structure and show the existence of topological

surface states in it. We also elucidate the relation of their directionality with the elastic Fermi arcs in the reciprocal space. We perform a transient simulation of the structure with a surface defect to numerically demonstrate the robust propagation of nontrivial surface waves. This study therefore paves the way for future research on the design and fabrication of Weyl physics-based structures for engineering applications, such as vibration control and energy harvesting.

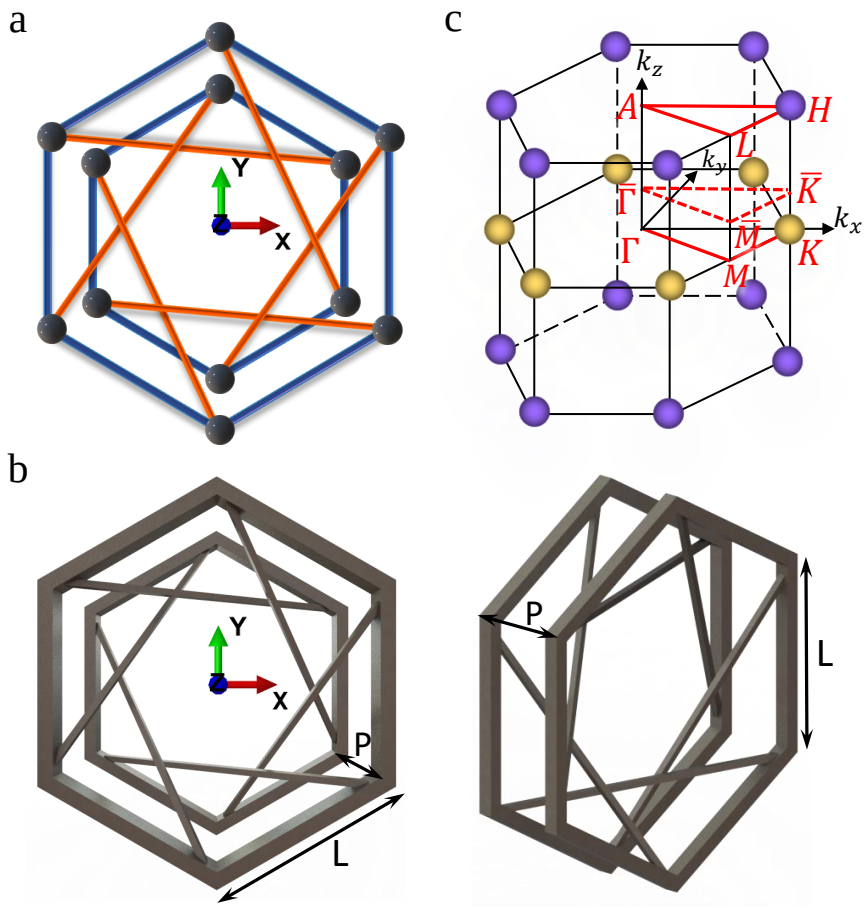

Figure 2.1: (a) AA-stacked hexagonal lattice (blue) with chiral inter-layer hopping (orange). (b) Top (left panel) and slanted (right) view of the unit cell of the 3D elastic structure. (c) Illustration of the first Brillouin zone and Weyl points with opposite topological charges indicated by the yellow and purple spheres.

2.2 Design of Weyl Structure

Previous studies in acoustics demonstrated the existence of Weyl points in a AA-stacked honeycomb lattice with chiral interlayer hopping [63]. A schematic of its nearest-neighbor tight-binding model is illustrated in Fig. 2.1(a). To make an equivalent mechanical system, we would need to use masses and springs that are connected by hinge joints. However, for the more realistic design, we deviate from spring-mass description and propose a unit cell made of beams as shown in Fig. 2.1(b). We take beam length $L = 20$ mm and height $P = 10$ mm. All in-plane beams (parallel to xy plane) have square cross section of width 3.0 mm, while out-of-plane beams have square cross section of width 0.7 mm to reduce the inter-layer stiffness. Note that we can still calculate the effective tight-binding Hamiltonian to analyze topological properties of our elastic structure. In Fig. 2.1(c), we show the first Brillouin zone with marked Weyl points at the high symmetric points. These are of two opposite charges and will appear in the simulation results shown in the next section. Characterization of the topological charge of Weyl points is discussed in more detail in subsection 2.4.1.

To conduct the numerical simulation, we use the commercial FEA software ABAQUS. We model the beams using the Timoshenko beam elements. We follow the method used in [72] to apply periodic boundary conditions and calculate frequency band diagrams. We use stainless steel 316L as the structural material with elastic modulus $E = 180$ GPa, density $\rho = 7900$ kg/m^3, and Poisson's ratio $\nu = 0.3$, which could be used for current 3D metal printing [73]. We neglect any material dissipation. The out-of-plane beams produce an effective synthetic gauge flux and break the effective time-reversal symmetry at a fixed k_z. Therefore, the system can be treated as an elastic realization of the topological Haldane model [26].

2.3 Result and Discussion

2.3.1 Weyl points in unit-cell dispersion

We show the band structure of the unit cell along the irreducible Brillouin zone at $k_z = 0$ in Fig. 2.2(a). We observe that the 13th and the 14th bands, predominately with out-of-plane polarization

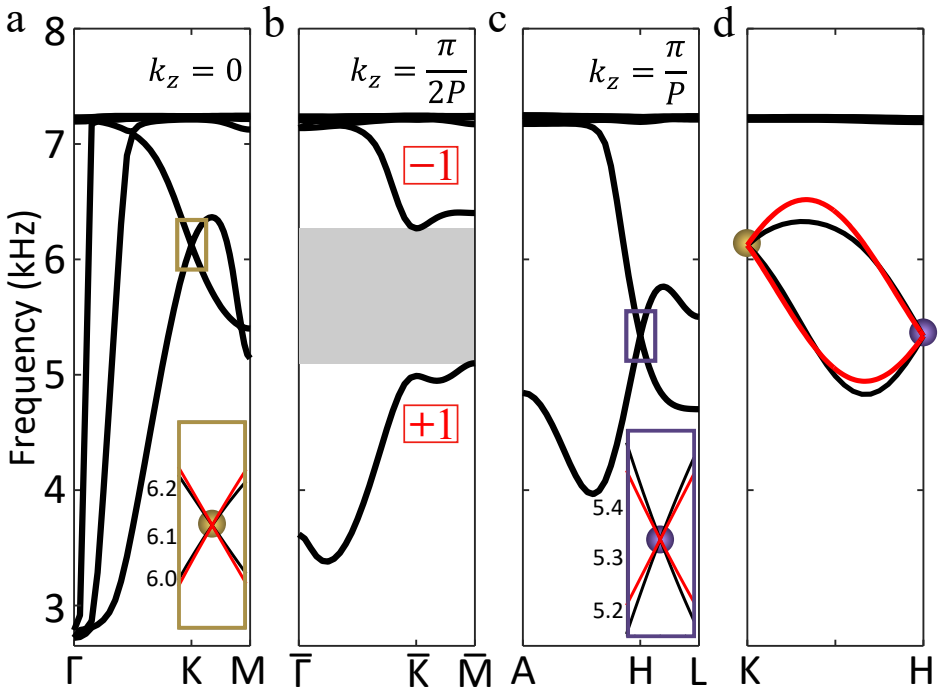

Figure 2.2: Dispersion diagrams on the reduced reciprocal $k_x k_y$ plane with fixed (a) $k_z = 0$, (b) $k_z = \pi/(2P)$, and (c) $k_z = \pi/P$. The yellow (purple) sphere refers to the Weyl point located at the K (H) point with topological charge -1 ($+1$). The grey area in (b) represents a complete band gap. (d) Dispersion diagram along the KH line. The red and black curves are obtained from the two-band Hamiltonian and the FEA simulations, respectively.

(see subsection 2.4.2), are degenerate at the K point around 6.12 kHz [see the rectangular box and its close-up inset in Fig. 2.2(a)]. This is a Weyl point in the system, and it is the same as the yellow spheres in Fig. 2.1(c). We calculate the Weyl charge by fitting the dispersion diagram of a two-band Hamiltonian around the Weyl point (see the red curves in the inset). As a result, we obtain the Weyl charge of -1 from this Weyl point (see subsection 2.4.1).

When we plot the dispersion diagram for $k_z = \pi/(2P)$, the degeneracy of the bands is lifted, and there emerges a band gap between 13th and 14th bands, as shown by the grey region in Fig. 2.2(b). We increase k_z further to plot the dispersion curves at $k_z = \pi/P$ [Fig. 2.2(c)]. We observe that the band gap closes again, and the two bands establish a degeneracy at 5.34 kHz, but at the H point of the Brillouin zone instead of the K point. This is the second Weyl point in the system,

and it corresponds to the purple markers in Fig. 2.1(c). As shown in the inset, we again use the two-band Hamiltonian to represent the dispersion characteristics around this Weyl point and find that the Weyl point has $+1$ topological charge.

In Fig. 2.1(d), we plot the dispersion diagram along the KH direction to clearly visualize the Weyl degeneracy at the K and H points and the existence of a band gap between the 13th and the 14th bands when the k_z value lies somewhere in between. We note that the two-band Hamiltonian (red curves) captures this evolution of the bands obtained through the FEA simulations (black curves) reasonably well. We use this effective Hamitonian to numerically calculate the Chern numbers of the two bands above and below the band gap for a fixed k_z. For positive k_z, these are -1 and $+1$ for the upper and the lower bands, respectively, as marked in Fig. 2.2(b). This indicates that the band gap is topologically nontrivial.

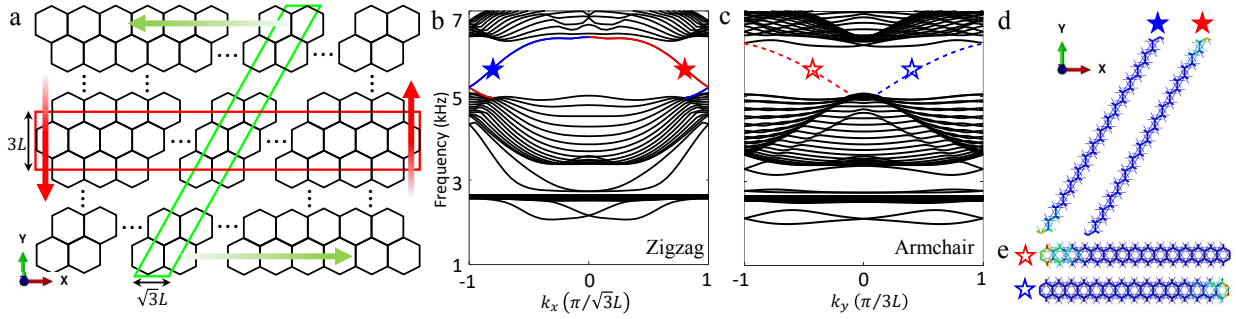

Figure 2.3: (a) Schematic of supercells with zigzag (green box) and armchair (red box) type boundaries. (b)-(c) Band structure with fixed $k_z = \pi/(2P)$ for the zigzag and armchair type supercells, respectively. The red and blue curves represent the topological surface modes at the two opposite ends of the supercell. (d)-(e) Mode shapes of the surface modes at 5.4 kHz corresponding to the solid and hollow stars in (b) and (c). Color intensity represents the magnitude of total displacements.

2.3.2 Directional surface states in supercell

Based on the bulk-edge correspondence of topology, we expect topologically protected boundary modes arising at finite boundaries. To this end, we construct two types of supercells, consisting of 15 unit cells each, having both armchair and zigzag types of finite boundaries. Figure 2.3(a) shows

a schematic of how we choose the two types of the supercells. For the zigzag supercell (see the slanted green box), we apply periodic boundary conditions in both x- and z-directions. We use free boundary conditions at the top and bottom ends. We fix $k_z = \pi/2P$ and plot dispersion diagram in Fig. 2.3(b). We observe two modes inside the band gap, which are localized on the top (red) and the bottom (blue) ends of the supercell [see Fig. 2.3(d)]. Based on their slope we can conclude that the top (bottom) end mode would have a negative (positive) group velocity in the x-direction [see the green arrows in Fig. 2.3(a)].

Similarly, we study another supercell with the armchair type of boundaries [see the horizontal red box in Fig. 2.3(a)]. We show that it supports localized modes on the left and the right ends [see Figs. 2.3(c) and 2.3(e)]. These left and right end modes exhibit negative and positive group velocities, respectively [see the red arrows in Fig. 2.3(a)]. Therefore, it is straightforward to deduce that a wave packet injected at 5.4 kHz (shown as star) on the surface of the full-scale lattice, having simultaneous zigzag and armchair boundaries, would travel counterclockwise for $k_z = \pi/(2P)$. In the same vein, we expect to obtain a traveling surface wave in the clockwise direction for $k_z = -\pi/(2P)$.

2.3.3 Elastic Fermi arcs in full-scale model

We now demonstrate the existence of surface states in a full-scale 3D structure. We choose a hollow structure for two reasons: (1) such structures are ubiquitous in applications; and (2) they require a reduced amount of computational time for numerical simulations, compared to solid ones. Without fixing k_z, we first excite our system at 5.4 kHz in the z-direction. In Figs. 2.4(a) and 2.4(b), we show the z-component of wave displacement when the excitation is placed at the centers of positive xz (denoted as PXZ, see the red star mark in the inset) and negative yz (NYZ) planes, respectively. As we can see, the surface states propagate in particular directions and do not spread all across the whole plane. Especially in Fig. 2.4(b), the wave propagates in the y-direction predominantly reflecting the collimation effect [67].

To investigate further, we perform the fast Fourier transformation (FFT) on the displacement field in the two spatial directions and plot the spectrum in Figs. 2.4(c) and 2.4(d). We observe the

arc-like pattern of the peak spectral density (in yellow). These are called "Fermi arcs", also seen as the counterpart representation of the surface states in the reciprocal space. Since the normal vector to the Fermi arcs would determine the direction of the wave's group velocity, we can deduce from Fig. 2.4(d) that the wave will propagate in the k_y-direction predominantly given the straight posture of the arc. This thus confirms the aforementioned collimation effect [Fig. 2.4(b)] in the wavevector space.

These Fermi arcs could also be obtained from the equi-frequency contour (FEC) analysis on the supercell (see details in subsection 2.4.3). To achieve this, we calculate dispersion characteristics of the supercells, as shown in Figs. 2.3(b) and 2.3(c), for *all* values of k_z inside the first Brillouin zone. We then extract the wave numbers for 5.4 kHz to obtain the red curves in Figs. 2.4(c) and 2.4(d). Here, solid curves correspond to the the solutions on the plane of excitation, while the dashed curves represent those on the opposite surface. Evidently, the red solid curves closely match the spectral density arcs obtained from the full-scale simulation. The Fermi arc generally connects the Weyl points of the opposite charges [65], but here we see that they connect the two Weyl points (in purple and yellow) roughly but not exactly. This is because the system supports the two Weyl points at different frequencies [see the frequency offset of the yellow and purple points in Fig. 2.2(d)]. Since the Weyl points with opposite charges at K and H points will be projected to the same points on the $k_x - k_y$ plane thus cancel each other, which indicates that no topological surface state exists on the XY surface.[56, 65]

2.3.4 Robust one-way propagation

We now proceed to the full-scale, transient numerical study performed at 5.4 kHz, but for a fixed k_z. Figure 2.5(a) shows the entire hollow structure, along with a rectangular defect on the XZ surface, to demonstrate the robustness of surface states. The top view of the structure is shown in figure 2.5(b). We fix all the degrees of freedom of the nodes on the top and bottom layers. To ensure the excitation with the desired k_z, we apply four-point excitation in the z-direction on the 10th to the 13th layers on the YZ plane (marked with the red arrows in Fig. 2.5(a) inset). We use a Gaussian-modulated sinusoidal pulse with the center frequency of 5.4 kHz, and we fix

$k_z = -\pi/(2P)$ by increasing the phase of the input signal by $\pi/2$ from the 10th to the 13th layer. From the discussions above, we expect that the wave packet would propagate *clockwise* when looking from the top (z-axis). In Figs. 2.5(c)–2.5(f), we plot total displacement of the system at time $t = 3.5$ ms, $t = 5.5$ ms, $t = 8$ ms, and $t = 10$ ms, respectively. We observe that the elastic wave remains on the surface of the structure and only travels upward in the clockwise direction (viewing from the top) without obvious scattering or reflection at the corners [see Fig. 2.5(d) and its inset] or near the defects [see Fig. 2.5(e) and its inset]. This, therefore, demonstrates a robust one-way propagation of surface elastic wave in our Weyl structure.

2.4 Additional discussion

2.4.1 Tight-binding Model of AA-stacked Graphene

We consider the tight-binding model of a AA-stacked graphene with chiral interlayer coupling, as depicted in Fig. 2.1(a). The unit cell has an in-plane lattice constant L and out-of-plane lattice constant P in the z-direction [see Fig. 2.1(b)]. Let the intralayer (interlayer) coupling be t_n (t_c). Therefore, we write the Bloch Hamiltonian given by [58, 63, 69]

$$H(\mathbf{k}) = \begin{pmatrix} \varepsilon + t_c f(k_z P) & t_n \beta \\ (t_n \beta)^* & \varepsilon + t_c f(-k_z P) \end{pmatrix},$$

where ε denotes the on-site potential, $\beta = e^{-ik_y L} + 2e^{ik_y L/2}\cos\left(\sqrt{3}k_x L/2\right)$, and $f(k_z P) = 2\cos(\sqrt{3}k_x L - k_z P) + 4\cos(3k_y L/2)\cos(\sqrt{3}k_x L/2 + k_z P)$. By applying the $k \cdot p$ method [58], we can expand the Hamiltonian near the K point [$k_x = 4\sqrt{3}\pi/(9L), k_y = 0, k_z = 0$] and obtain the effective Hamiltonian:

$$H(\triangle\mathbf{k}) = (\varepsilon - 3t_c)\sigma_0 - \frac{3}{2}Lt_n(\triangle k_x \sigma_x - \triangle k_y \sigma_y) - 3\sqrt{3}Lt_c \triangle k_z \sigma_z,$$

Here, $\Delta\mathbf{k} = (\Delta k_x, \Delta k_y, \Delta k_z)$ is a small k-vector deviating from the K point, σ_0 is the 2×2 unit matrix, and σ_x, σ_y, σ_z are the Pauli matrices. We use $\varepsilon = 5.73$ kHz, $t_n = 0.875$ kHz, and $t_c = -0.131$ kHz for fitting the two-band dispersion with the curves obtained from the FEA results seen

in Fig. 2.2. The effective Hamiltonian describes a Weyl point at the K point, whose topological charge is given by $C = \mathrm{sgn}(v_x v_y v_z)$, where Dirac velocities $v_x = -3Lt_n/2$, $v_y = 3Lt_n/2$, and $v_z = -3\sqrt{3}Lt_c$. Therefore, $C = -1$ in this case. Similarly, by expanding the Hamiltonian at the H point $[k_x = 4\sqrt{3}\pi/(9L), k_y = 0, k_z = \pi/P]$, we verify that there is another Weyl point with the topological charge of $+1$ located at the H point.

2.4.2 Unit-cell Dispersion and Mode Polarization

We show the modes that are degenerate at the Weyl points are an *out-of-plane* type with a predominant z component. To this end, we define a polarization factor $P_z = |U_z|^2/(|U_x|^2 + |U_y|^2 + |U_z|^2)$ to distinguish bands with different polarization components, where U_x, U_y, and U_z are the x-, y-, and z- components of the eigenvectors. Therefore, the out-of-plane modes, with predominately U_z component, would have the polarization factor close to a unity, while the polarization factors of the in-plane modes would approach zero. We plot the bulk bands of the unit cell – colored with the information about the polarization factors – on the 2D reciprocal plane at various k_z values in Fig. 2.6. We can clearly see that the Weyl points are formed by the degeneracy of the two bands containing out-of-plane modes (in red).

2.4.3 Equi-frequency Contour Analysis

Equi-frequency contour on the the xz plane, as shown in Fig. 2.4(c), can be obtained by calculating the band structure of the supercell with the zigzag type boundary. At $f = 5.4$ kHz, we vary k_x from $-4\pi/(3\sqrt{3}L)$ to $4\pi/(3\sqrt{3}L)$ and k_z from $-\pi/P$ to π/P, to obtain wavevector plots in green as shown in Fig. 2.7(a). Note that we plot another equi-frequency plot at slightly higher frequency ($f = 5.5$ kHz) in blue to get a sense of the normal vector, i.e., the group velocity shown by red arrows at $k_z = \pm\pi/2P$. Similarly, result of the yz plane, from the supercell with the armchair type boundary, is shown in Fig. 2.7(b). This equi-frequency contour confirms the collimation effect in the k_y direction.

2.5 Conclusion

We design a 3D mechanical structure – analogous to the AA-stacked honeycomb lattice – by using slender beams. We show that this relatively simple design carries Weyl points at the vertices of the Brillouin zone. We use a two-band Hamiltonian model to describe the dynamics around the Weyl points and calculate their topological charges. We show the finite boundaries of this structure, both zigzag and armchair types, host localized states at a fixed k_z. Using numerical simulations on a full-scale 3D structure, we show the existence of the Fermi arcs and compare them with the results obtained from equi-frequency contour analysis. We highlight two unique wave phenomena in our structure: (i) collimation of the propagating elastic waves and (ii) robust one-way transport of elastic energy around the corners and defects. Our design could be easily scaled up or down, and can be relevant to applications, such as sensing, energy harvesting, and vibration control on 3D elastic structures.

2.6 Author contributions

This chapter is adopted from the author's following publication: X. Shi, R. Chaunsali, F. Li, and J. Yang, *Elastic Weyl Points and Surface Arc States in Three-Dimensional Structures*, Phys. Rev. Applied 12, 024058 (2019). [74] X. Shi and J. Yang conceived the idea of the project. X. Shi performed the numerical simulations under the guidance of R. Chaunsali. J. Yang supervised the project. All authors interpreted the results and reviewed the manuscript.

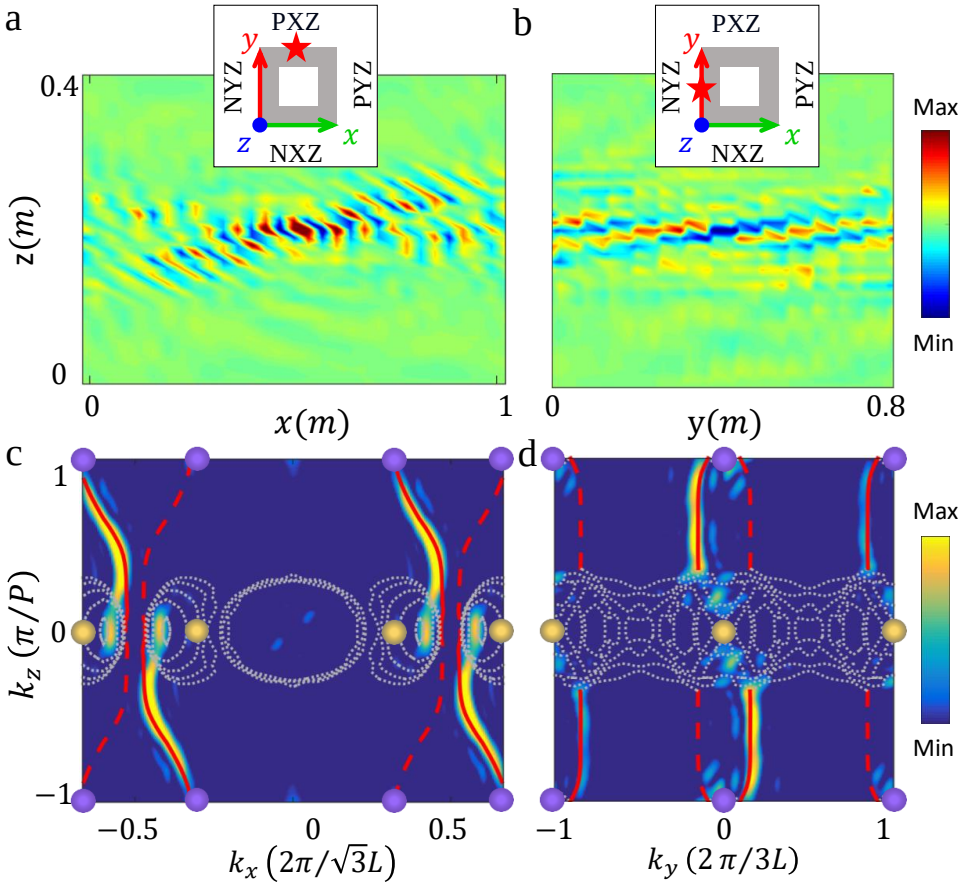

Figure 2.4: Surface states and elastic Fermi arcs in a full-scale 3D hollow structure. (a)-(b) Surface states under the harmonic excitation at 5.4 kHz on the xz and yz planes, respectively. The point sources of excitation are placed in the center of each plane, as shown in the insets. The color intensity represents the nodal displacement in the z-direction (u_z). (c)-(d) Spatial Fourier transforms of the field distributions of the surface states on the xz and yz planes, respectively. Spectral density shows the elastic Fermi arcs that connect the projections of the Weyl points with the opposite topological charges in the reduced 2D Brillouin zone. The red solid curves represent the simulated elastic Fermi arcs on the corresponding surfaces through supercell analysis, while the dashed curves indicate the Fermi arcs on the opposite surfaces. The projected bulk bands are shown as the dotted grey curves.

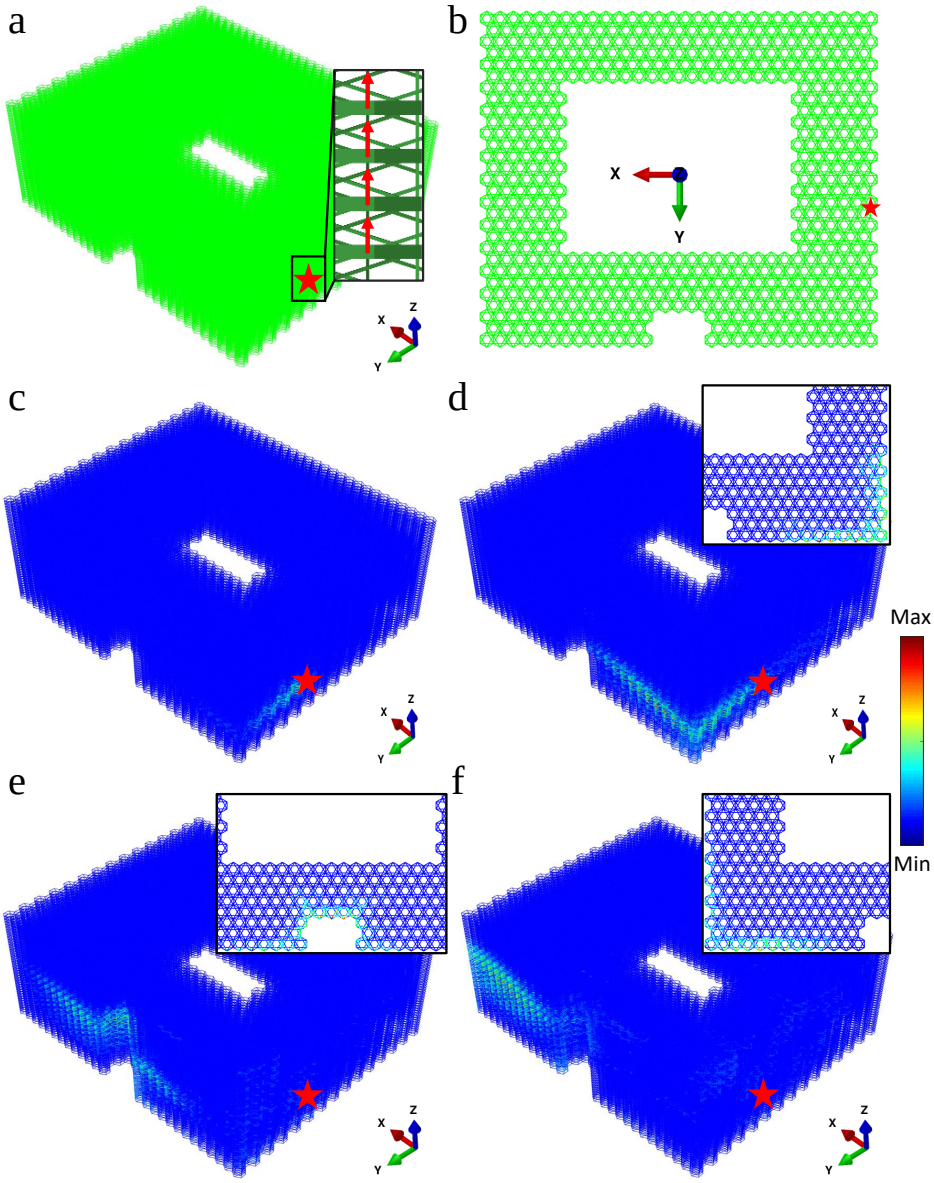

Figure 2.5: Robust one-way surface state propagating in a 3D hollow structure. (a)-(b) A schematic and the top views of the 3D hollow sample with a surface defect on the XZ surface. The red stars highlight the location of multi-point phased excitation. The exact locations of external loads are shown in the inset in (a). (c)–(f) The magnitude of total displacement of the surface elastic states at time $t = 3.5$ ms, $t = 5.5$ ms, $t = 8$ ms, and $t = 10$ ms, respectively. Insets in (d)–(f) show the cut views when the wave travel through the corner or defect at 12th, 18th, and 25th layer, respectively.

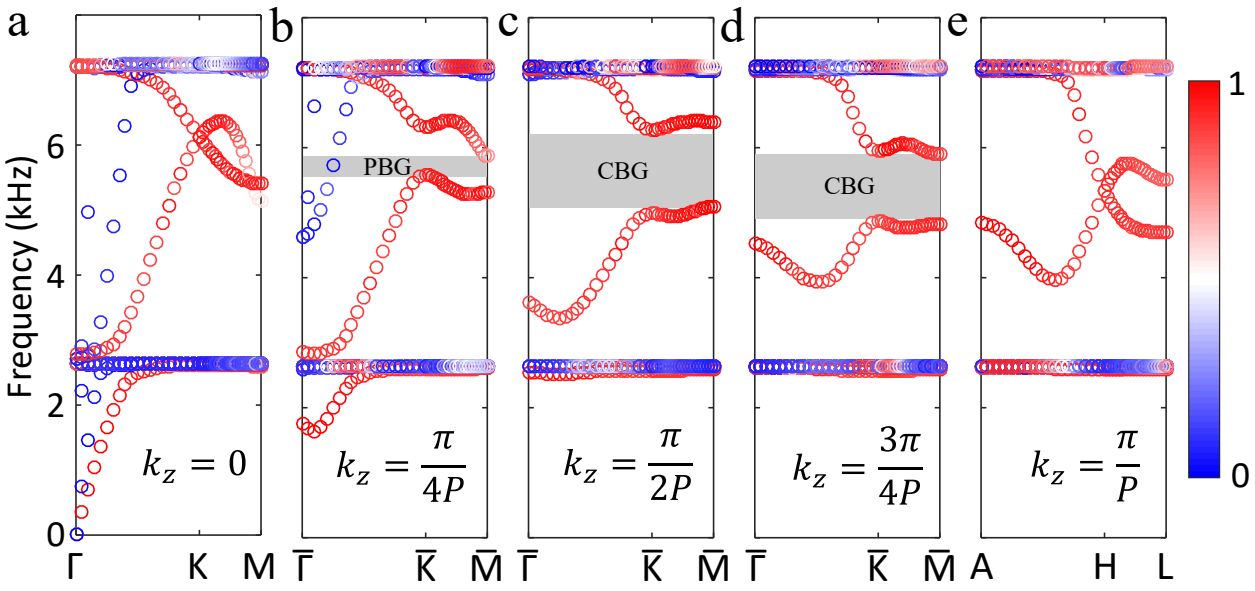

Figure 2.6: Dispersion diagram of the unit cell in the $k_x k_y$ plane at (a) $k_z = 0$, (b) $k_z = \pi/(4P)$, (c) $k_z = \pi/(2P)$, (d) $k_z = 3\pi/(4P)$, and (e) $k_z = \pi/P$, respectively. Colormap represents the polarization factor P_z. The grey area in (b) represents a *partial* frequency band gap (noted as PBG) while the grey zones in (c) and (d) refer to *complete* band gaps (noted as CBG). The flat branches mainly represent the cases when the interlayer beams are locally resonant.

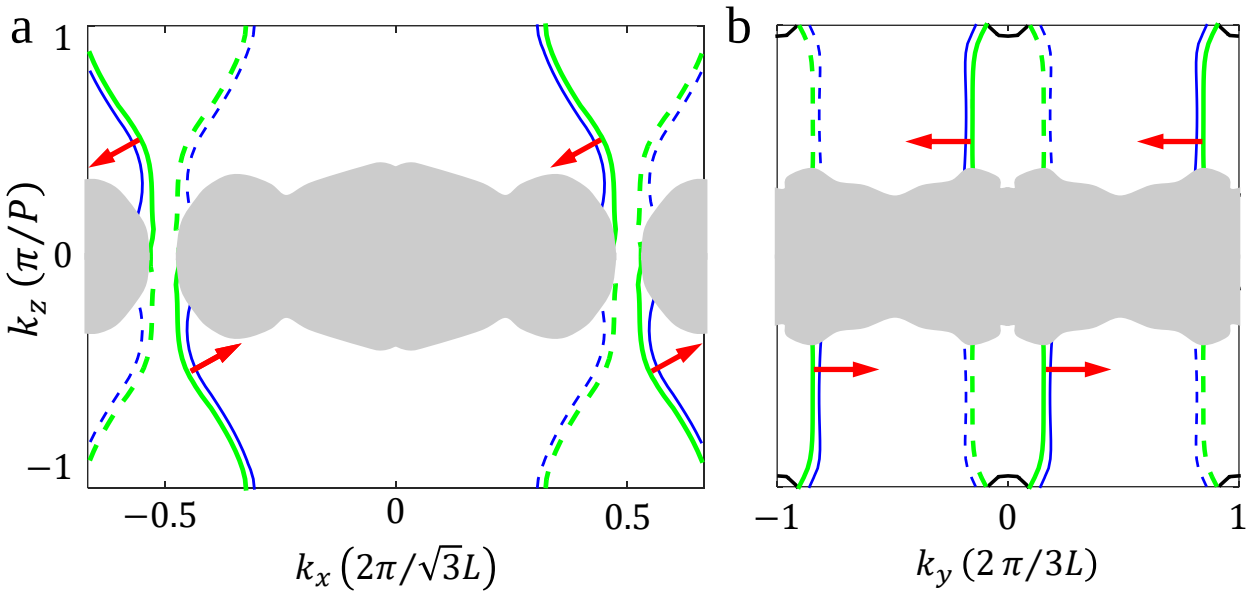

Figure 2.7: (a) Equi-frequency contour of the supercell with the zigzag type boundaries at $f = 5.4$ kHz (green) and $f = 5.5$ kHz (blue). Red arrows show the normal vectors of the dispersion curves. Solid and dashed lines represents the mode in the forward and the opposite planes as indicated in Fig. 2.4. The grey regions refers to the projections of the bulk bands. (b) Similar results of the supercell with armchair type boundaries.

Chapter 3

SPIN-1 WEYL POINT AND SURFACE ARC STATE IN A CHIRAL PHONONIC CRYSTAL

Spin-1 Weyl point is formed by three bands touching at a single point in the three dimensional (3D) momentum space, with two of which show cone-like dispersion while the third band is flat. Such triply degenerate point carries higher topological charge ± 2 and can be described by a three band Hamiltonian. We first propose a tight-binding model of a 3D Lieb lattice with chiral interlayer coupling to form the Spin-1 Weyl point. Then we design a chiral phononic crystal that carries these spin-1 Weyl points and special straight-type acoustic Fermi arcs. We also computationally demonstrate the robust propagation of the topologically protected surface states that can travel around a corner or defect without reflection. Our results pave the new way to manipulate acoustic waves in 3D structures and provide a platform for exploring energy transport properties in 3D spin-1 Weyl systems.

3.1 Introduction

In the past decade, Weyl semimetals [31, 53, 75] have become a research focus in the field of three dimensional (3D) topological states, which are characterized by the touching of two bands with linear dispersion in all directions in the 3D momentum space, namely the Weyl point. Weyl points behave as monopoles of Berry flux in the reciprocal space, which carry a none zero topological charge (or Chern number) [76]. Such topological invariants result in the robustness of the Weyl points that are stable to the small perturbations and cannot be easily gapped. Previous research in Weyl materials has demonstrated a variety of exotic phenomena, such as robust surface states [31] and a chiral anomaly [59]. In parallel, Weyl points have also been realized in other classic systems of electromagnetic [60, 61, 58, 62, 77], acoustic [63, 64, 65, 68, 67, 78], and stress waves [71, 74],

leading to the novel applications, such as negative refraction [68] and collimation effect [67]. In addition to the single Weyl point with topological charge (± 1), double Weyl points carrying higher topological charges (± 2) have also been discovered [53, 58, 62, 68, 71], which are formed by the degeneracy of two bands with quadratic dispersion in a certain momentum plane.

Recently, a new type of triply-degenerate point of topological charge (± 2), referring to the spin-1 Weyl point [79], has started to attract much attention. It is formed by the linear degeneracy of three bands having cone-like dispersion with a flat band located at the touching point, which can be described by a simple three band $\mathbf{k}\cdot\mathbf{S}$ Hamiltonian with the spin-1 vector $\mathbf{S}$ [79]. Spin-1 Weyl points have been theoretically predicted in the condensed mater systems [79, 80, 81, 32], cold atoms [82, 83, 84] and then verified in the real materials [85, 86, 87, 88, 89]. Y. Yang *et al*. designed and fabricated the first 3D phononic crystal with space group $P2_13$ (No. 198) that carries the acoustic spin-1 Weyl point [90]. They experimentally demonstrated the double Fermi arcs and topologically protected negative refraction of the surface states. However, unit cell is fairly complicated with a non-symmorphic structure. Also, the system hosts both charge-2 threefold and fourfold degenerate points in the Brillouin zone, where the wave propagation is affected by both kinds of degenerate points. The question naturally arises as to whether one could design a simple structure to study the acoustic wave transport properties in the 3D spin-1 Weyl systems.

In this chapter, we realize the spin-1 Weyl points in a 3D acoustic system. We start with a tight binding model for a Lieb lattice with chiral interlayer interaction. Previous studies have shown that a 2D Lieb lattice [91], along with other types of 2D lattices such as $\mathscr{T}_3$ lattice [92] and Kagome lattice [93], can form spin-1 Dirac points. We construct 3D Weyl structure by stacking up the 2D subsystems with the help of the synthetic gauge flux, which is introduced by the appropriate coupling in the third dimension [63]. We verify that this 3D chiral Lieb lattice can supports one pair of spin-1 Weyl points of topological charge ± 2 in the first Brillouin zone. The associated Fermi arcs and topological surface states are also demonstrated in the proposed architecture. The nearly straight Fermi arcs indicate that we can realize a collimated and robust propagation of surface waves [67].

3.2 Tight-binging Model of 3D Lieb Lattice

We begin with a tight-binding model of the 3D Lieb lattice with chiral interlayer coupling, as shown in Fig. 3.1(a). The unit cell has an in-plane lattice constant a and out-of-plane lattice constant H, containing three sites A (red sphere), B (blue sphere), and C (green sphere). Therefore, we can write the Hamiltonian of the tight-binding model in the momentum space as:

$$H(\mathbf{k}) = \begin{bmatrix} \varepsilon_1 + \gamma & 2t_{n1}\cos(\frac{k_y a}{2}) & 2t_{n1}\cos(\frac{k_x a}{2}) \\ 2t_{n1}\cos(\frac{k_y a}{2}) & \varepsilon_2 + 2t_{n4}\cos(k_y a) & \alpha + i\beta \\ 2t_{n1}\cos(\frac{k_x a}{2}) & \alpha - i\beta & \varepsilon_2 + 2t_{n4}\cos(k_x a) \end{bmatrix}$$

Here, ε_1 stands for the onsite potential on A sites, while ε_2 denotes the onsite potential on B and C sites, $\alpha = [t_{n2} + 4t_c\cos(k_z H)]\cos(\frac{k_x a}{2})\cos(\frac{k_y a}{2})$, $\beta = 4t_c\sin(k_z H)\sin(\frac{k_x a}{2})\sin(\frac{k_y a}{2})$ and $\gamma = 2t_{n3}[\cos(k_x a) + \cos(k_y a)]$. t_c represents the interlayer hopping, while t_{ni} highlight the intralayer hopping.

Figure 3.1(b) provides more details of the definition of different intralayer hopping parameters. Specifically, t_{n1} and t_{n2} are the short-range hopping, which refers to the nearest-neighbor (between A and B/C sites) and next-nearest-neighbor (between B and C sites) hopping, respectively. In this study, we introduce not only short-, but also long-range hopping to improve the accuracy of the tight-binding model. To this end, we introduce t_{n3} (t_{n4}), which stands for the long-range hopping between A sites (B/C sites). The first Brillouin zone and the reduced 2D reciprocal $k_x - k_y$ plane are given in Figs. 3.1(c) and 3.1(d).

Without loss of generality, we first consider a simplified tight-binding model with only intralayer nearest neighbour hopping t_{n1} and the chiral interlayer hopping t_c. In Fig. 3.1(e), we show a typical band structure of the tight-binding model along the high-symmetry lines in the first Brillouin zone with hopping parameters $\varepsilon_1 = \varepsilon_2 = 0$, $t_{n1} = 1$, and $t_c = 0.1$. Evidently, the three bands degenerate at the M point as indicated by the purple point in Fig. 3.1(e). To investigate the topological property of this triply degenerate point, we expand the Hamiltonian around $M(\frac{\pi}{a}, \frac{\pi}{a}, 0)$ point, which gives:

$$H(\Delta\mathbf{k}) = \varepsilon S_0 - t_{n1}\Delta k_x S_1 - t_{n1}\Delta k_y S_2 - 4t_c\Delta k_z S_3.$$

Here, $\varepsilon = \varepsilon_1 - 4t_{n3} = \varepsilon_2 - 2t_{n4}$ is the eigenenergy of the triply degenerate point, $\Delta\mathbf{k} = (\Delta k_x, \Delta k_y, \Delta k_z)$ is a small k-vector deviating from the M point, S_0 is the 3×3 unit matrix, and S_1, S_2, S_3 are three of the Gell-Mann matrices given as [94]:

$$S_1 = \begin{pmatrix} 0 & 0 & 1 \\ 0 & 0 & 0 \\ 1 & 0 & 0 \end{pmatrix}, S_2 = \begin{pmatrix} 0 & 1 & 0 \\ 1 & 0 & 0 \\ 0 & 0 & 0 \end{pmatrix}, S_3 = \begin{pmatrix} 0 & 0 & 0 \\ 0 & 0 & -i \\ 0 & i & 0 \end{pmatrix}.$$

Such a linearized Hamiltonian describes a spin-1 Weyl points of topological charge +2, which is a natural generalization of the regular weyl point [94, 79]. Note that the triply degenerate points exist only if the system parameters (ε_1, ε_2, t_{n3}, and t_{n4}) satisfy the equation $\varepsilon = \varepsilon_1 - 4t_{n3} = \varepsilon_2 - 2t_{n4}$. This indicates that the spin-1 Weyl point in this model is not guaranteed by the symmetry properties of the unit cell. Instead, it is a result of accidental degeneracy and requires very fine tuning of the system parameters, most importantly the on-site potentials. Near the degenerate point in Fig. 3.1(e), the first and third bands have linear dispersion, while the second band remains nearly flat, which is typical behavior of the spin-1 Weyl point. Similarly, there exists another spin-1 Weyl point with topological charge -2 at the corner of the first Brillouin zone (R point). Figure 3.1(f) shows the $3D$ dispersion surfaces near the two spin-1 Weyl points, which gives a better visualization of the Weyl cones that interact with a nearly flat band in gray.

3.3 Result and Discussion

3.3.1 Spin-1 Weyl point phononic crystal

Although the tight-binding model is just a simple toy model, it provides a keen insight into physics and thus, a guideline for designing realistic phononic systems. Inspired by the recent work on acoustic Type I or Type II Weyl points [63, 65, 67, 78], we design a chiral phononic crystal following the stacking-up approach. Each layer of the structure can be viewed as a 2D Lieb lattice

that carries a Dirac point, which is intersecting with a flat band. By introducing the appropriate interlayer coupling, we can construct the triply degenerate spin-1 Weyl point in the 3D reciprocal space.

Figure 3.2(a) shows the unit cell of the structure with a lattice constant $a = 20$ mm in xy plane. The unit cell consists of a scattering pillar and a perforated plate base with slanted air tubes. Figure 3.2(b) is a top view of the upper pillar, which contains a cylinder (radius = $\sqrt{\frac{b^2+t^2}{2}}$) in the center and four wings. The hollow channels (filled by air) between the neighboring solid pillars form the in-plane acoustic waveguide in analogue to the 2D Lieb phononic lattice. The wings have width $L = 10$ mm and thickness $t = 2$ mm. The distance between the centerlines of the two parallel wings is $b = 5$ mm. The colored letters (A, B, and C) give us rough mapping relations between the in-plane waveguides and the tight-binding model shown in Fig.3.1(a).

Figure 3.2(c) shows the perforated plate base. The four purple regions represent the slanted air tubes that bring the chiral interlayer couplings. These holes are generated by sweeping a surface [shown in Fig. 3.2(c) inset] in a spiral manner for 90 degrees. The details of the intralayer and interlayer waveguides are demonstrated in subsection 3.4.1. Both the upper pillar and the base plate are of height $h_p = h_b = 5$mm, such that the unit cell is of height $H = 10$ mm in total in the z direction.

The distribution of the spin-1 Weyl points in the first Brillouin zone is shown in Fig. 3.2(d). As we can see, there exists a spin-1 Weyl point with topological charge $+2$ at the M point on the $k_z = 0$ plane and a spin-1 Weyl point carrying topological charge -2 located at the R point on the $k_z = \pm\pi/H$ planes. The topological charges of the Weyl points are numerically calculated by the Wilson Loop method [95] (See subsection 3.4.2 for details). Considering the Weyl points at the M (R) points are shared by 4 (8) neighboring Brillouin zones, there are total one pair of spin-1 Weyl points with opposite charges (± 2) existing in the first Brillouin zone.

To confirm the existence of the spin-1 Weyl points, we conduct numerical simulations of the acoustic wave dispersions using the commercial finite element analysis (FEA) software COMSOL. We show the computational results of the frequency band structures of the unit cell on 2D reduced reciprocal plane for fixed $k_z = 0$, $k_z = \pi/2H$, and $k_z = \pi/H$ in Fig. 3.2(e). For comparison,

we also include the results based on the long-range tight-binding model (dashed curves), which are in excellent agreement with the FEA results. See subsection 3.4.3 for details, including the improvement of the tight-binding model's accuracy by implementing long-range model over the short-range one.

In Fig. 3.2(e), we observe that the first three bands of the bulk dispersion diagram degenerate at the M and R points. While k_z is different from 0 and $\pm\pi$, the degeneracy at the Weyl points is broken by the synthetic gauge flux introduced by the chiral interlayer couplings. Such a trend can be observed through the unit cell band structure along the MR line at the boundary of the first Brillouin zone [see Fig. 3.2(f)]. When we fix $k_z = \pi/2H$, the degeneracy is lifted, and two band gaps merge between the first three bands. By evaluating the rotational symmetry of the eigenmodes at the high symmetric points in the reduced 2D Brillouin zone [96], we know that the two band gaps are of nonzero Chern number (-1), which indicates that they are topologically nontrivial. Based on the bulk-edge correspondence of topology, we expect to see topologically protected localized modes at the boundary of the system.

3.3.2 Surface arc states and acoustic Fermi arc

To demonstrate the topologically protected, directional surface arc states in the system, we construct a supercell consisting of 20 unit cells. The strip is finite in the y direction and has hard boundary conditions on the positive and negative y ends. We apply periodic boundary conditions in both x and z directions. By fixing $k_z = \pi/2H$ and varying k_x from $-\pi/a$ to π/a, we obtain the projected band structures in the x direction, as shown in Fig. 3.3(a). We can observe that surface arc states emerge in both of the nontrivial band gaps. The red curves represent the modes that are localized at the bottom ends, while the blue curves stand for the modes localized at the top ends. Four localized eigenmodes corresponding to the stars in Fig. 3.3(a) are plotted in Fig. 3.3(b). By looking at the slope of the bands that represent the surface arc states, we can determine the sign of their group velocities. We know that the bottom-end (top-end) modes will propagate in the positive (negative) x direction. Then the Fermi arc can be obtained by looking at the equifrequency contour of the band structure of the supercell in the 2D Brillouin zone spanned by k_x and k_z. Here, the fixed

frequency works as an equivalent *Fermi energy* in the acoustic systems.

The equifrequency contour at $f = 7.8$ kHz (lying in the first band gap) and $f = 10$ kHz (lying in the second band gap) are plotted in Figs. 3.3(c) and 3.3(d) respectively. The colored lines represent the acoustic Fermi arcs that connect two Weyl points with opposite charges. Specifically, the red (blue) lines stand for the surface Fermi arcs on the positive (negative) xz plane. The grey regions represent the projected bulk bands. As we can see, Fermi arcs exist in both band gap regions, implying that our structure can support unidirectional surface states in multiple frequency bands. Also, the nearly straight Fermi arcs suggest that the wave packages have group velocity parallel to the x directions, which forms the collimation effect of the surface waves.

We then construct an infinite system to verify the robustness of the surface arc states against the defect and sharp bend (Fig. 3.4). Such an infinite structure is periodic in the z direction and has finite boundaries in both x and y directions. We introduce a 3×3 defect on both right and left boundaries. The top boundary is set to be radiative so that the sound waves can leak out to the outside environment, as marked by the green edge in Fig. 3.4. A point source is located at the center of the bottom boundary denoted by the red stars. For fixed $k_z = -\pi/2H$ and $f = 7.8$ kHz, we can see that the surface waves only travel in the clockwise direction and can pass around the defect and right angle corner without back-scattering [See Fig. 3.4(a)]. If we set $k_z = +\pi/2H$, the surface waves will travel to the opposite direction [see Fig. 3.4(b)]. Similarly, the surface arc states at $f = 10$ kHz are demonstrated and confirmed in the subsection 3.4.4.

3.4 Additional discussion

3.4.1 Views of the filling air in the unit cell

In this subsection, we provide more details of the filling air in the unit cell. Figure. 3.5(a) contains the oblique and top views of the chiral interlayer air channels, which introduces the synthetic gauge flux in the system. As we can see, all the top holes rotate 90 degrees in a spiral manner with respect to the bottom holes. Figure. 3.5(b) shows the in-plane 2D acoustic waveguide which is formed by the air between two neighboring perforated plates. The scattering pillars help to form an effective

2D Lieb lattice. Then, these neighboring 2D waveguides are coupled by the interlayer air channels, thereby forming a 3D chiral Lieb lattice.

3.4.2 Calculation of the Chern numbers with Wilson loop method

The Chern number (or topological charge) can be calculated by integrating Berry curvature on a closed surface enclosing a band degenerate point. Following the method in Refs. [75, 77, 90], we numerically determine the Chern number by tracking the evolution of the Wannier centers on a sphere surrounding the spin-1 Weyl point using the Wilson loop method [95]. The calculated Wannier centers on the horizontal loops varying from the north pole to the south pole of the enclosing sphere are presented in Fig. 3.6. As we can see in Fig. 3.6(a), the Wannier centers of the spin-1 Weyl point at the M point for the first, second and third bands shift by $+4\pi$, 0, and -4π, respectively. This implies that such spin-1 Weyl point has a positive charge of $+2$. Similarly, by looking at Fig. 3.6(b), we can conclude that there exists a spin-1 Weyl point of charge -2 located at R point in the first Brillouin zone.

3.4.3 Unit cell band structure calculated by the tight-binding model and full wave simulations

In Fig. 3.7, we compare the frequency band structures of the unit cell obtained by tight-binding models and the full wave simulations using COMSOL. The solid black lines are the results of COMSOL simulations, which are the same as those ploted in Fig. 3.2(e) and 3.2(f). The results of simplified (i.e., short-range model with $t_{n2} = t_{n3} = t_{n4} = 0$) and full three-band (i.e., long-range) tight-binding model are shown as the blue dot lines and red dashed lines respectively. The hopping parameters used in a tight-binding model of both cases are determined by fitting the results with the results of COMSOL full-wave simulations. As we can see in Fig. 3.7, the simplified Hamiltonian (blue dot line) only works within a small range near the spin-1 Weyl point with the fitting parameters given as $\varepsilon_1 = \varepsilon_2 = 8.516$, $t_{n1} = -1.524$ and $t_c = -0.410$. However, by taking into account more hopping terms, the full tight-binding model (red dashed line) can capture the band structures of real phononic crystal very well in the whole Brillouin zone. Here, we set

$\varepsilon_1 = 8.5448$, $\varepsilon_2 = 7.9962$, $t_{n1} = -1.436$, $t_{n2} = -0.509$, $t_{n3} = -0.232$, $t_{n4} = 0.021$, $t_c = -0.448$ in the full tight-binding model calculation.

3.4.4 Surface states at $f = 10$ kHz

Previously, we show the equifrequency contours of supercell at $f = 10$ kHz in Fig. 3.3(d). It is clear that, for several k_z ranges, the structure supports bulk modes and surface modes simultaneously. In this case, we can hardly excite the clear surface modes since they are coupled with the bulk modes and will easily leak to the bulk. To demonstrate such an effect, we conduct numerical simulations under surface excitation at $f = 10$ kHz for $k_z = +\pi/2H$ or $k_z = +\pi/5H$ [see Fig. 3.8]. Similar to the setup in the main context, the structure is infinite in the z direction with a radiative boundary placed on the top edge, denoted by the green line. For $k_z = +\pi/2H$, the surface states can be clearly observed as all the energy is well confined to the boundary of the structure. However, when we set $k_z = +\pi/5H$, we can barely see the surface waves near the excitation point, and the energy quickly leaks into the bulk of the system.

3.5 Conclusion

In conclusion, a three-band tight-binding model of a 3D Lieb lattice is introduced to predict the existence of the spin-1 Weyl points. Guided by the tight-binding model, we designed a 3D chiral phononic crystal that carries spin-1 Weyl points with topological charge ± 2 in the first Brillouin zone. We observed special straight-type acoustic Fermi arcs and the collimated robust propagation of topological surface arc states in the system. The key points of this work can be summarized as follows:

(i) We propose a tight-binding model of a $3D$ Lieb lattice with chiral interlayer hopping. In addition, we include both the short- and long-range hopping terms, which ensures a deeper understanding of the spin-1 Weyl points from the physics aspect.

(ii) While most of the existing structures supporting Weyl points and surface arc states are based on a woodpile- or graphene-based design, our design explores a platform consisting of square-

shaped unit cells to study Weyl physics in acoustic systems. Moreover, the unit cell is of simple geometry and is designed with ease of assembly.

(iii) This study reports dual-band topologically protected and collimated surface waves in the spin-1 Weyl structure.

The present results paved the way for manipulating acoustic waves in a 3D structure, which can be potentially extended to other artificial systems of photonic lattices [97] and mechanical lattices [98].

3.6 Author contributions

This chapter is adopted from the author's following publication: X. Shi and J. Yang, Spin-1 *Weyl Point and Surface Arc State in a Chiral Phononic Crystal*, Phys. Rev. B 101, 214309 (2020). [99] X. Shi and J. Yang designed the research. X. Shi performed the numerical simulation and wrote the manuscript. J. Yang supervised the project and reviewed the manuscript.

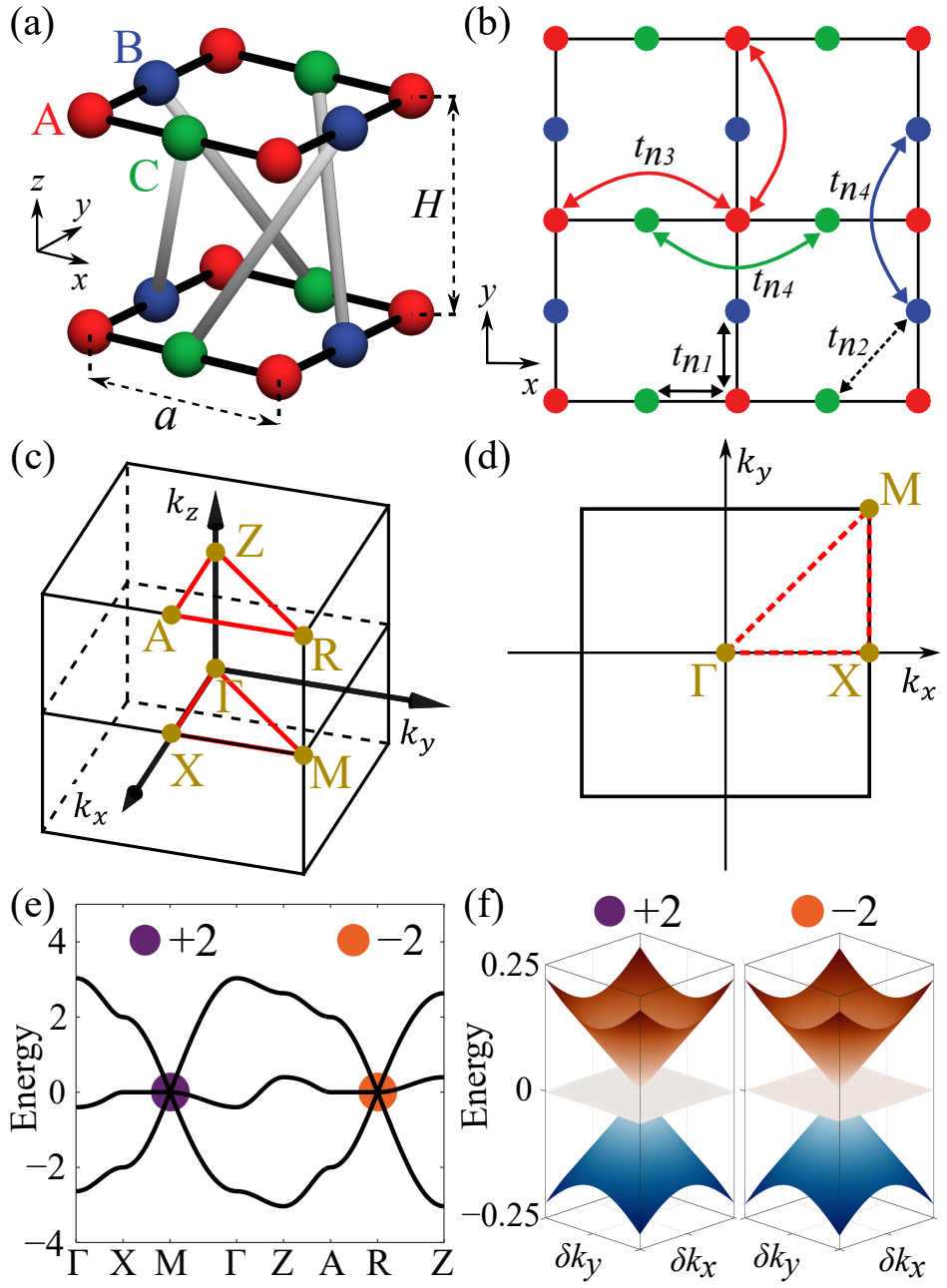

Figure 3.1: (a) Schematic of the 3D Lieb lattice with chiral interlayer couplings. (b) Illustration of in plane short- and long-range intralayer hoppings. (c) First Brillouin zone of the system. (d) 2D reduced reciprocal $k_x - k_y$ plane with fixed $k_z = 0$. (e) Band structure of the three band Hamiltonian with purple and orange points indicating the spin-1 Weyl points. (f) 2D band structure near the spin-1 Weyl points at the M and R points.

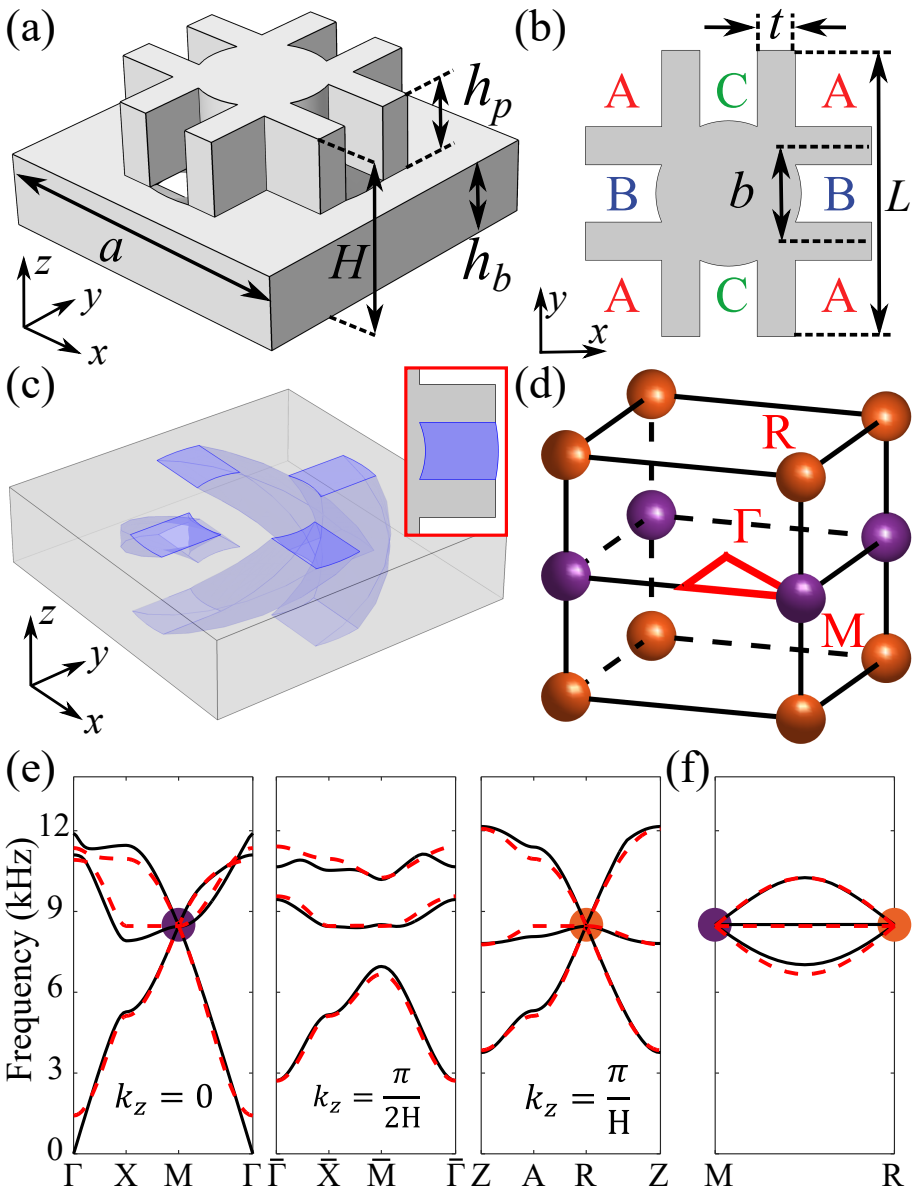

Figure 3.2: (a) Schematic of the unit cell of the chiral phononic crystal. (b) Top view of the upper pillar of the unit cell. (c) Lower perforated plate base of the unit cell. (d) Distribution of the spin-1 Weyl points within the first Brillouin zone. (e) Bulk band structure of the phononic crystal in the reduced 2D reciprocal $k_x - k_y$ plane for fixed $k_z = 0$, $k_z = \pi/2H$, and $k_z = \pi/H$. (f) Bulk band structure along the *MR* direction. The results calculated by full-wave simulation in COMSOL and long-range tight-binding model are shown in (e) and (f) as the solid black lines and dashed red lines, respectively.

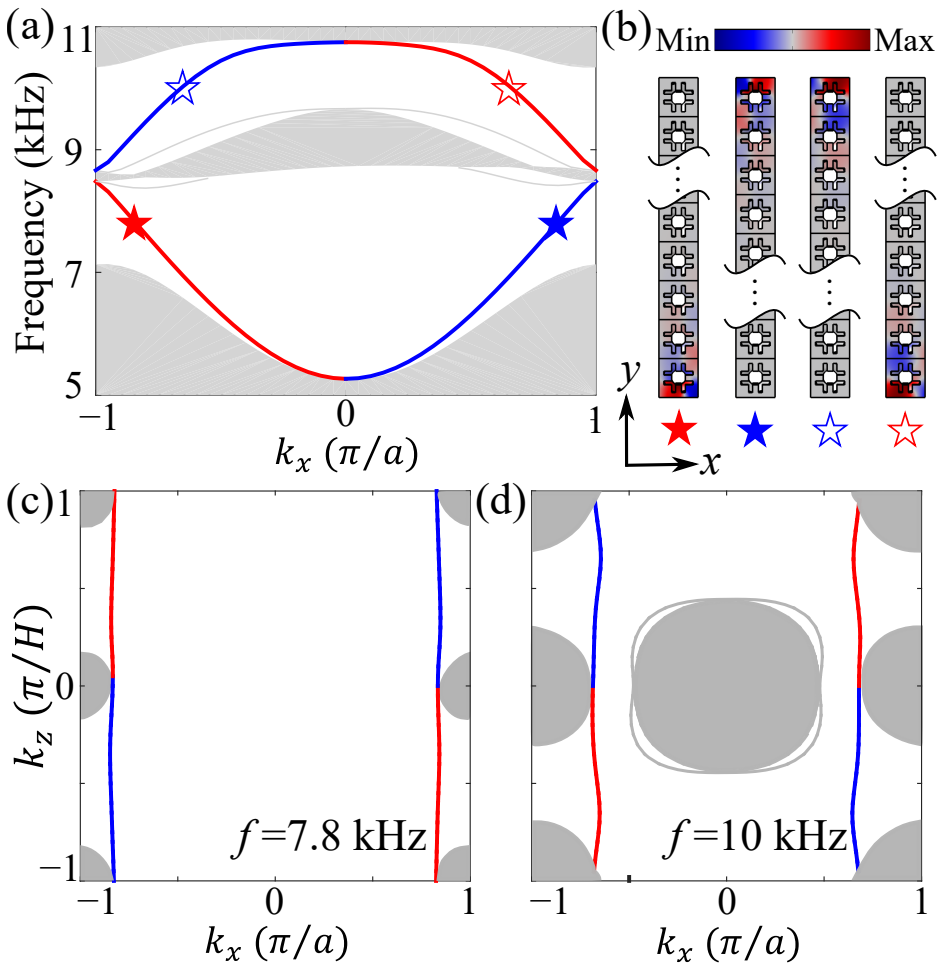

Figure 3.3: (a) Projected band structure of the supercell along the x direction for fixed $k_z = \pi/2H$. (b) Calculated eigenmodes of surface arc states at 7.8 kHz or 10 kHz corresponding to the stars in (a). Color intensity represents the magnitude of the acoustic pressure field. Equifrequency contours at (c) $f = 7.8$ kHz and (d) $f = 10$ kHz, respectively. The red (blue) lines represent the acoustic Fermi arcs on the negative (positive) xz plane.

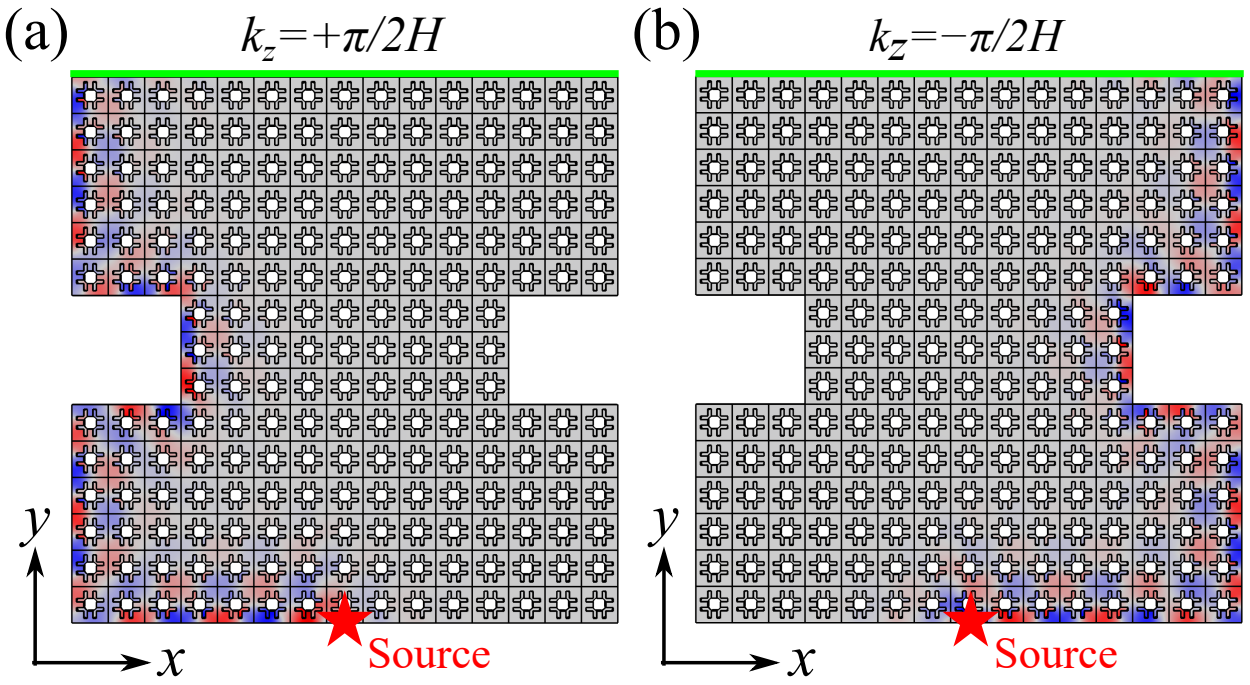

Figure 3.4: One-way propagation of the topologically protected surface arc states at $f = 7.8$ kHz for (a) $k_z = -\pi/2H$ and (b) $k_z = +\pi/2H$. Color intensity represents the magnitude of acoustic pressure field.

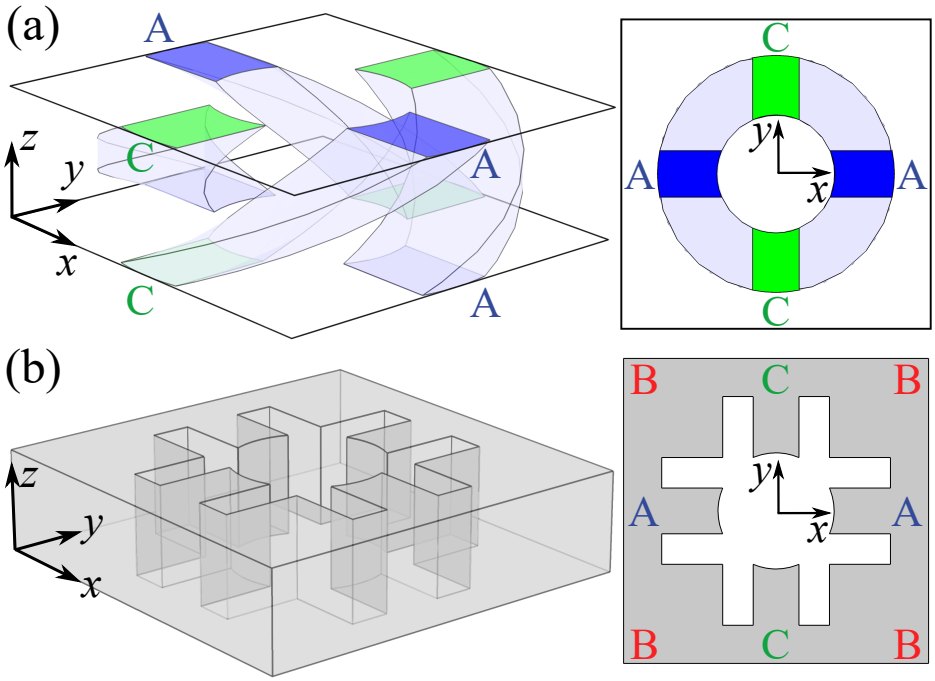

Figure 3.5: Oblique and top views of (a) Interlayer air channels. (b) Intralayer 2D acoustic wave guide with a Lieb lattice formed by the scattering pillars.

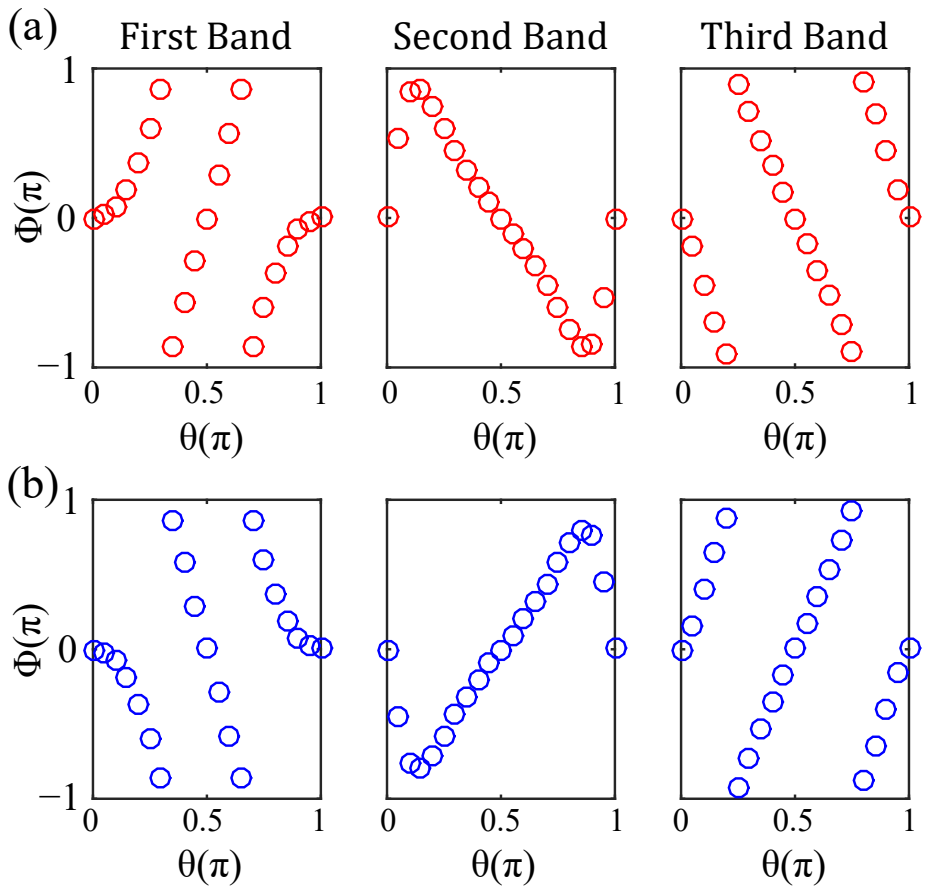

Figure 3.6: Evolution of the Wannier centers on the spheres enclosing the spin−1 point (a) Wannier centers for the first three bands near the *M* point, respectively. (b) for the first three bands near the *R* point, respectively.

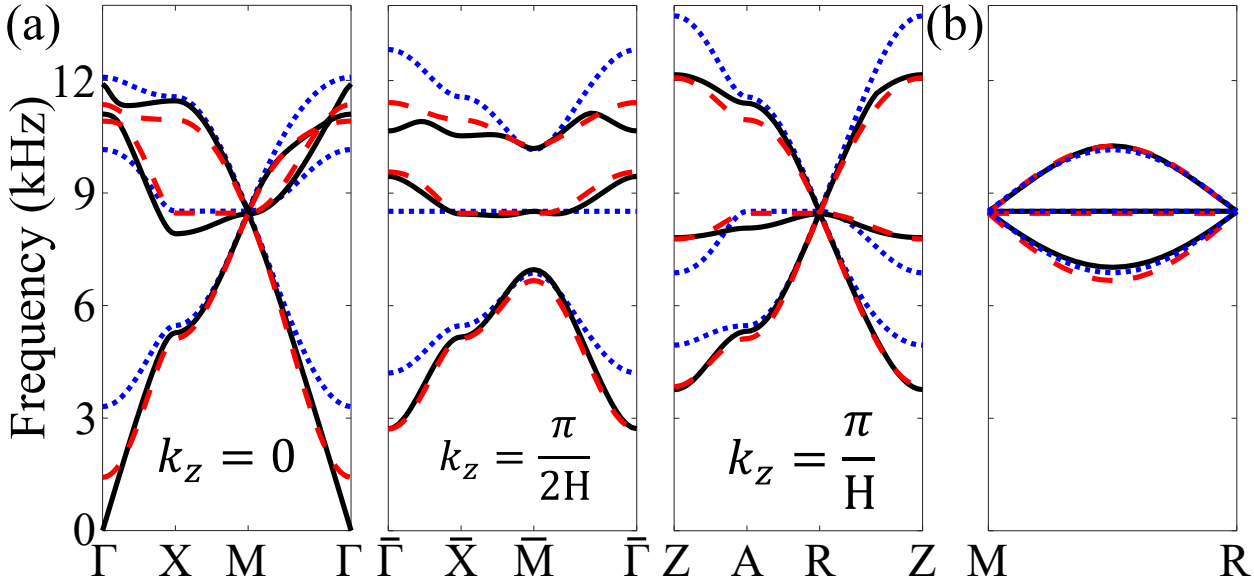

Figure 3.7: Bulk band structure of the unit cell obtained by tight-binding models and full-wave simulations in (a) the reduced 2D reciprocal $k_x - k_y$ planes and (b) $M - R$ lines in the first Brillouin zone.

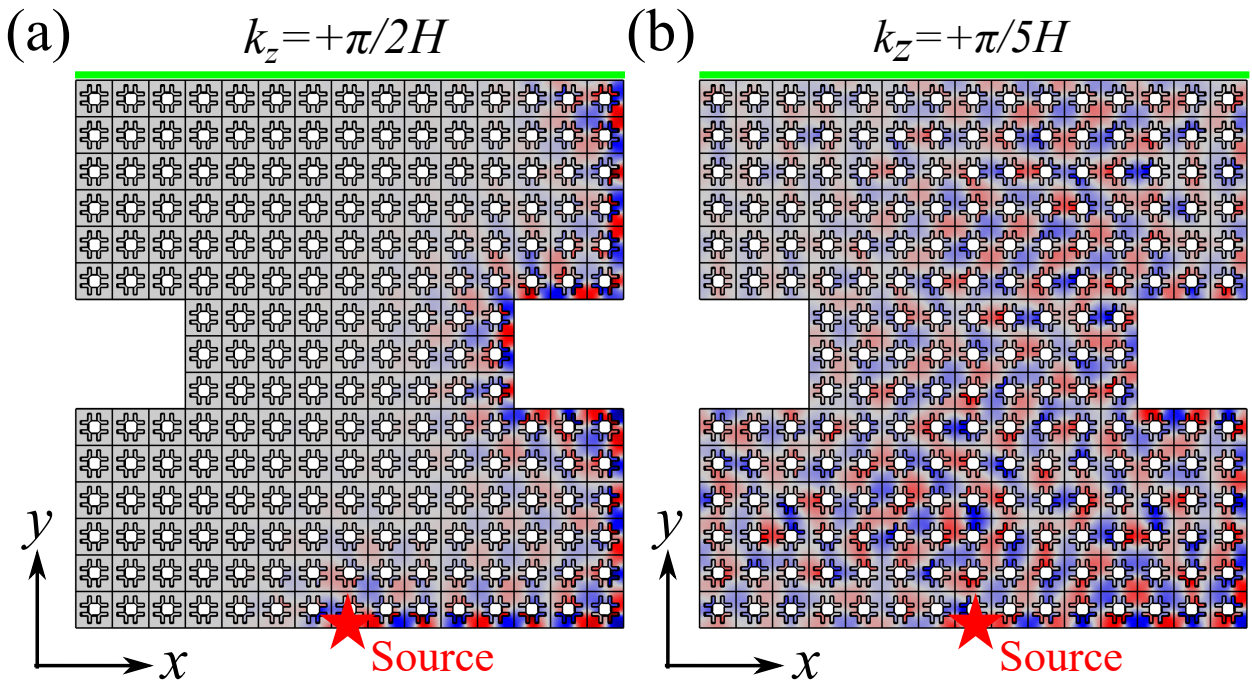

Figure 3.8: Surface arc states at $f = 10$ kHz which lies in the second topological nontrivial band gap for (a) $k_z = +\pi/2H$ and (b) $k_z = +\pi/5H$. Color intensity represents the magnitude of the acoustic pressure field.

Chapter 4

DISORDER-INDUCED TOPOLOGICAL PHASE TRANSITION IN A 1D MECHANICAL SYSTEM

We numerically investigate the topological phase transition induced purely by disorder in a spring-mass chain. We employ two types of disorders – chiral and random types – to explore the interplay between topology and disorder. By tracking the evolution of real space topological invariants, we obtain the topological phase diagrams and demonstrate the bilateral capacity of disorder to drive topological transitions, from topologically nontrivial to trivial and vice versa. The corresponding transition is accompanied by the realization of a mechanical Topological Anderson Insulator. The findings from this study hint that the combination of disorder and topology can serve as an efficient control knob to manipulate the transfer of mechanical energy.

4.1 Introduction

With the discovery of Topological Insulators in condensed matter [50, 51], there have been tremendous efforts to explore topological phases in classical wave systems, including photonic [100, 101, 102, 33], acoustic [103, 104, 18], and elastic [105, 106, 107, 108, 109, 110] systems. Based on the bulk-edge correspondence for topological insulators, one can predict the existence of topological states on the boundary of the system by characterizing the bulk of a material with an invariant. Such states are protected by internal symmetries and are immune to certain types and levels of disorder [20]. As disorder inevitably destroys the periodicity of the system, it is natural to think that the presence of disorder tends to suppress topological properties. However, the discovery of Topological Anderson Insulators (TAI) [42, 111, 41, 112, 113, 114, 115] suggests that disorder can actually induce the abnormal transition from topologically trivial to nontrivial states, which brings the studies on the interplay of topology and disorder into a new era. Later, the concept of TAI

has been further illustrated and experimentally verified in atomic wires [116], photonic systems [117], and recently in acoustic waveguides [118]. In all these cases, the tight binding model of 1D Su-Schrieffer-Heeger (SSH) was used. However, the interplay of both topology and disorder in lattices described by a second order differential equations in time, capable of describing the dynamics of not only a variety of mechanical systems (e.g., spring-mass model) but also several electric structures (LC circuits), has not been explored.

Here, inspired by previous studies, we propose a dimer spring-mass system mimicking the 1D Su-Schrieffer-Heeger (SSH) model [119] to realize the topological phase transition. Despite some similarities with previous models, this mechanical system has some important differences that can lead to distinctive behaviors in the presence of disorder. First, the band gap region is around a finite frequency as opposed to zero frequency in the SSH model. Second, in the SSH model, hopping disorder only changes the energy spectrum while preserving system's chiral symmetry. On the contrary, disorder in the spring stiffness of a spring-mass chain usually breaks the chiral symmetry, since the perturbation is reflected in the diagonal entries of the dynamical matrix as well. Third, as noted earlier, the equations of motions are governed by the second-order differential equations in time, such that the topological characterization of real space obtained from the transient response of the system should be handled carefully. Therefore, to understand the effect of disorder on the topological properties of this classical system comprehensively, we introduce two types of disorders in our spring-mass chain: i) a chiral (chiral-symmetry preserving) and ii) a random disorder. To probe the topological properties for various disorder scenarios, we use three kinds of topological invariants defined in the real space (displacements of the masses). Moreover, we keep track of the localization length in the system to capture the boundaries between topologically distinct phases. While the random type of disorder is more common in mechanical settings, we demonstrate that in the carefully designed setting of chiral disorder, we can achieve both kinds of topological phase transitions, from topologically nontrivial to trivial and vice versa. The later type leads to the mechanical analogue of TAI.

4.2 Model

4.2.1 Equations of Motion

In this part, we consider a 1D dimer spring-mass chain, as shown in Fig. 4.1, which is composed of particles of uniform mass ($m = 0.01$ throughout this study) connected by alternating springs. All the particles are attached to the ground with an onsite spring (K_0), which acts in the horizontal direction. Each unit cell contains two particles. The springs located within the unit cell are defined as intracell springs (K_a) while those connecting neighboring unit cells are called intercell springs (K_e). We assume the 1D dimer chain contains n unit cells, i.e., $N = 2n$ particles and $N+1$ inter and intracell springs in total.

By imposing fixed boundary conditions on both ends, the equations of motion of the system can be written as:

$$\begin{aligned} m\ddot{u}_1 &= -k_1 u_1 - k_2(u_1 - u_2) - k_1^0 u_1, \\ m\ddot{u}_j &= k_j(u_{j-1} - u_j) - k_{j+1}(u_j - u_{j+1}) - k_j^0 u_j, \quad j \in [2, N-1] \\ m\ddot{u}_N &= k_N(u_{N-1} - u_N) - k_{N+1} u_N - k_N^0 u_N, \end{aligned} \tag{4.1}$$

where u_j is the displacement of the jth particle, k_j is the spring constant between the $(j-1)$th and jth particles, and k_j^0 is the jth onsite spring constant, such that $k_j = K_e$ for odd j, $k_j = K_a$ for even j, and $k_j^0 = K_0 \; \forall j$.

We can rearrange the equations of motion into a matrix form as follows:

$$\ddot{\mathbf{U}}(t) + \mathbb{D}\mathbf{U}(t) = 0, \tag{4.2}$$

where $\mathbf{U}(t)$ and $\mathbb{D}$ are the displacement vector of length N and the dynamical matrix of dimension $N \times N$, respectively. The dynamical matrix is real and symmetric and takes the following form:

$$\mathbb{D} = \frac{1}{m}\begin{bmatrix} K_a+K_e+K_0 & -K_a & ... & 0 & 0 \\ -K_a & K_a+K_e+K_0 & -K_e & ... & 0 \\ ... & ... & ... & ... & ... \\ 0 & ... & -K_e & K_a+K_e+K_0 & -K_a \\ 0 & 0 & ... & -K_a & K_a+K_e+K_0 \end{bmatrix}. \tag{4.3}$$

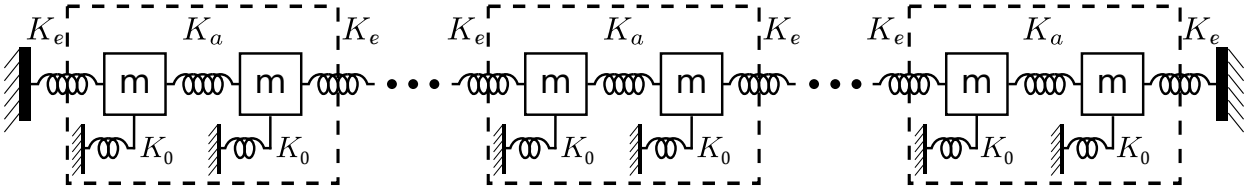

Figure 4.1: Schematic of the 1D dimer spring-mass chain with ground springs. Unit cell is highlighted with the box.

To get the system's time-history response, we can rewrite Eq. (4.2) as a first-order state equation

$$\dot{\mathbf{X}} = \mathbb{A}\mathbf{X}, \tag{4.4}$$

where $\mathbf{X} = \begin{bmatrix} \mathbf{U}(t) \\ \mathbf{V}(t) \end{bmatrix}$ is the state vector consisting of displacement and velocity components of all the particles, and $\mathbb{A} = \begin{bmatrix} 0 & \mathbb{I} \\ -\mathbb{D} & 0 \end{bmatrix}_{2N\times 2N}$ with $\mathbb{I}$ being the identity matrix.

4.2.2 Spectrum

To perform the eigen analysis, we assume a harmonic system response and substitute the ansatz $\mathbf{U}(t) = \mathbf{U}e^{i\omega t}$ into Eq. (4.2) and get:

$$\mathbb{D}\mathbf{U}_j = \omega_j^2 \mathbf{U}_j \tag{4.5}$$

where $\mathbf{U}_j$ is an eigenvector corresponding to the eigenfrequency ω_j. We note that after the removal of the diagonal term $(K_a+K_e+K_0)/m$ from the dynamical matrix of Eq. (4.3), which shifts the

spectrum to the frequency $\omega_0 = \sqrt{\frac{K_a+K_e+K_0}{m}}$, the remaining matrix obeys the anti-commutative relation:

$$\Gamma[\mathbb{D} - \omega_0^2\mathbb{I}] + [\mathbb{D} - \omega_0^2\mathbb{I}]\Gamma = 0, \tag{4.6}$$

where $\mathbb{I}_{N\times N}$ denotes the identity matrix and Γ is the chiral operator (see subsection 4.5.1 for details). The system in this case is said to possess the chiral symmetry and in combination with the time reversal symmetry, it results in a symmetric square of the spectrum (ω^2) around the mid-gap square frequency (ω_0^2). In addition, all the eigenvectors have their chiral partner, namely for every eigenvector $\mathbf{U}_k$ with eigenfrequency ω_k, there is an eigenvector $\mathbf{U}_l$ with eigenfrequency ω_l such that $\Gamma\mathbf{U}_k = \mathbf{U}_l$ and $\omega_k^2 - \omega_0^2 = -(\omega_l^2 - \omega_0^2)$.

4.2.3 Disorder arrangement

Although in the clean limit (without disorder), the dynamic matrix of the dimer spring-mass chain shares the same topological property with the Hamiltonian matrix of a 1D SSH chain, these two systems become quite different in the presence of disorder. Mathematically speaking, the diagonal terms of the SSH Hamiltonian matrix depend only on the onsite energies. By introducing disorder on the hoppings in the SSH tight-binding model, we will only vary the off-diagonal terms of the SSH Hamiltonian matrix. In contrast, the diagonal terms of the dynamic matrix of a spring-mass chain are the summation of two neighboring springs and the onsite ground spring. In consideration of such difference, we introduce two types of disorder to study their effects on topological phase transitions in the 1D mechanical system. The disorder strengths of intercell and intracell springs are noted as W_e and W_a, respectively. Then, the jth disordered spring stiffness can be written as:

$$k_j = \begin{cases} K_e + \delta_j = K_e + W_e\varepsilon_j & \text{if } j \text{ is odd} \\ K_a + \delta_j = K_a + W_a\varepsilon_j & \text{if } j \text{ is even} \end{cases} \tag{4.7}$$

where ε_j are random, independent numbers chosen uniformly from the range $[-1, 1]$.

First, we discuss the case of chiral disorder, which we call Type I disorder in this study. For this particular type, in order to keep the chiral symmetry of the system, we choose the ground springs

to take values $k_j^0 = K_0 + \delta_j^0$ with $\delta_j^0 = -\delta_j - \delta_{j+1}$. By doing so, we balance out the disorders of the coupling springs, and thus the diagonal terms of the spring matrix are constant. Then, the dynamical matrix of the system with chiral disorder can be expressed as:

$$\mathbb{D}^I = \frac{1}{m}\begin{bmatrix} K_a+K_e+K_0 & -K_a-\delta_2 & ... & 0 & 0 \\ -K_a-\delta_2 & K_a+K_e+K_0 & -K_e-\delta_3 & ... & 0 \\ ... & ... & ... & ... & ... \\ 0 & ... & -K_e-\delta_{N-1} & K_a+K_e+K_0 & -K_a-\delta_N \\ 0 & 0 & ... & -K_a-\delta_N & K_a+K_e+K_0 \end{bmatrix}. \quad (4.8)$$

Note that we have again $\Gamma[\mathbb{D}^I - \omega_0^2\mathbb{I}] + [\mathbb{D}^I - \omega_0^2\mathbb{I}]\Gamma = 0$. Therefore, the disorder matrix $\mathbb{D}^I - \omega_0^2\mathbb{I}$ is chiral symmetric, as in the clean case, and a symmetric spectrum is expected to be formed around ω_0^2.

We call the random disorder type II disorder. Here, we only introduce disorders independently on intercell (K_e) and intracell (K_a) springs, while keeping the on-site springs unperturbed. In this case, the dynamical matrix takes the following form

$$\mathbb{D}^{II} = \frac{1}{m}\begin{bmatrix} K_a+K_e+K_0+\Delta_1 & -K_a-\delta_2 & ... & 0 & 0 \\ -K_a-\delta_2 & K_a+K_e+K_0+\Delta_2 & -K_e-\delta_3 & ... & 0 \\ ... & ... & ... & ... & ... \\ 0 & ... & -K_e-\delta_{N-1} & K_a+K_e+K_0-\Delta_{N-1} & -K_a-\delta_N \\ 0 & 0 & ... & -K_a-\delta_N & K_a+K_e+K_0-\Delta_N \end{bmatrix}, \quad (4.9)$$

where $\Delta_j = \delta_j + \delta_{j+1}$. As one can easily check, due to the non-constant diagonal terms, the disorder matrix $\mathbb{D}^{II}$ is not chiral, and the spectrum is not symmetric around the ω_0^2 anymore. Note that we mainly focus on the stiffness disorder in this study. The reason is that with disorder in masses the diagonal terms of the dynamical matrix are not identical and the system does not possess chiral symmetry. Therefore, we expect the effect of mass disorder to be similar to that of random stiffness disorder, which also breaks the chiral symmetry.

4.3 Topological characterization

For an infinitely-long clean dimer chain, its topological property could be characterized by the winding number defined in the wave vector space [20]. It is quantized and can take only integer values in a system possessing chiral symmetry. However, such formula cannot be applied to the disorder system directly, since the translational symmetry is broken. Therefore, we need to handle the topological invariant in the real space. Following Ref. [116], we introduce three types of topological invariants calculated by the real space wave functions, specifically *local topological marker* ν, *mean chiral displacement* $C(t)$ and *infinite-time limit of mean chiral displacement* C_∞.

*Local Topological Marker (LTM).*The local topological marker is based on the eigenfuctions of the system and gives a local value for the topological invariant when this is evaluated away from the boundaries [116], see the appendix of [116] for more information. First, we construct a modal matrix $\mathbb{U}$ by arranging all the normalized eigenvectors $\mathbf{U}_j$ with corresponding eigenfrequencies in ascending order. Specifically, $\mathbb{U} = [\mathbf{U}_1, \mathbf{U}_2, ..., \mathbf{U}_n, \mathbf{U}_{n+1}, ..., \mathbf{U}_N]$. Let $\mathbb{U}_- = [\mathbf{U}_1, \mathbf{U}_2, ..., \mathbf{U}_n]$, and $\mathbb{U}_+ = [\mathbf{U}_{n+1}, \mathbf{U}_{n+2}, ..., \mathbf{U}_N]$. Then the projectors of the negative (below the band gap) and positive (above the band gap) energy spectrum are given as $\mathbb{P}_- = \mathbb{U}_-\mathbb{U}_-^T$ and $\mathbb{P}_+ = \mathbb{U}_+\mathbb{U}_+^T$, respectively. We can then define "flat band Hamiltonian" as $\mathbb{Q} = \mathbb{P}_+ - \mathbb{P}_-$. The $\mathbb{Q}$ matrix is decomposed as $\mathbb{Q} = \mathbb{Q}_{AB} + \mathbb{Q}_{BA} = \Gamma_A\mathbb{Q}\Gamma_B + \Gamma_B\mathbb{Q}\Gamma_A$, where Γ_A and Γ_B refer to the projectors onto the A or B particles respectively, and $\Gamma = \Gamma_A - \Gamma_B$ is the chiral operator (see subsection 4.5.1). Then, the LTM can be defined as:

$$\nu(l) = \frac{1}{2}\sum_{a=A,B}\{(\mathbb{Q}_{BA}[\mathbb{X}, \mathbb{Q}_{AB}])_{la,la} + (\mathbb{Q}_{AB}[\mathbb{Q}_{BA}, \mathbb{X}])_{la,la}\}, \tag{4.10}$$

where $\mathbb{X}$ is the position operator (see subsection 4.5.1), l is the unit cell number, lA and lB indicate the entries of the matrix corresponding to the A or B particle for the lth unit cell. This marker works as a local topological invariant when evaluated in a region away from the boundary of the system. To extract a value for the winding number in a disordered system, we need to average $\nu(l)$ over a small region in the center of the chain for single disorder realization ($\bar{\nu}$) then over multiple disorder realizations ($\langle\bar{\nu}\rangle$).

Mean chiral displacement (MCD).—Another type of variable that can detect the winding in a 1D chiral system is the *mean chiral displacement* [120, 121], given as

$$C(t) = 2\langle \Psi(t)|\widehat{\Gamma}\widehat{\mathbb{X}}|\Psi(t)\rangle, \tag{4.11}$$

where $\Psi(t) = e^{-iHt}|0_a\rangle$ represents the time evolution of an initially localized state in a quantum mechanical system. Unlike the quantum mechanical system, which is governed by the Schrödinger equation, a first-order differential equation, our 1D spring-mass chain is governed by second-order differential equations. Therefore, we cannot use the above definitions of MCD directly. Instead, we first map our mechanical system to a quantum-mechanical problem. Following the framework proposed by Süsstrunk and Huber [122], we introduce

$$\Psi(t) = \begin{bmatrix} \sqrt{\mathbb{D}} & 0 \\ 0 & i \end{bmatrix} \begin{bmatrix} \mathbf{U}(t) \\ \mathbf{V}(t) \end{bmatrix}, \tag{4.12}$$

which transform the time evolution equation given in Eq. (4.3) into $i\dot{\Psi}(t) = \mathbb{H}\Psi(t)$ with $\mathbb{H} = \begin{bmatrix} 0 & \sqrt{\mathbb{D}} \\ \sqrt{\mathbb{D}} & 0 \end{bmatrix}$ being a Hermitian matrix. This resembles the Schrödinger equation. Moreover, we define the extended chiral operator and displacement operator as $\widehat{\Gamma} = \left[\begin{smallmatrix} \Gamma & 0 \\ 0 & \Gamma \end{smallmatrix}\right]$ and $\widehat{\mathbb{X}} = \left[\begin{smallmatrix} \mathbb{X} & 0 \\ 0 & \mathbb{X} \end{smallmatrix}\right]$, respectively. With these extended operators we can then calculate the MCD from Eq. (4.11).

Infinite-time-limit of mean chiral displacement (IMCD).—As $t \to \infty$, the MCD converges to a time-independent variable given as:

$$C_\infty = 2\sum_{j=1}^{2N} |\alpha_{aj}|^2 \langle \widehat{\Psi}_j|\widehat{\Gamma}\widehat{\mathbb{X}}|\widehat{\Psi}_j\rangle \tag{4.13}$$

where $\widehat{\Psi}_j$ is the jth normalized eigenvector of the transformed Hamiltonian $\mathbb{H}$, and α_{aj} indicates the projection of the initial state $\Psi(0)$ on the jth eigenvector.

4.3.1 Capturing topological transition through localization length

Apart from the aforementioned topological invariants, we may also study the system's localization properties, since it is found that a topological transition is accompanied with a divergence of the localization length Λ [113, 115] at the Fermi level, corresponding to the mid-gap frequency ω_0 in our case. Indeed, for the chiral disorder case, at ω_0 the following solutions can be obtained:

$$\begin{aligned} u_{2n-1} &= (-1)^{n-1} \prod_{j=1}^{n-1} \frac{k_{2j}}{k_{2j+1}} u_1 \\ u_{2n} &= (-1)^{n-1} \prod_{j=1}^{n-1} \frac{k_{2j+1}}{k_{2j+2}} u_2, \end{aligned} \tag{4.14}$$

where the k_j's are given by equation (4.7). Then, assuming an exponential form for these solutions and applying the Birkhoff's theorem, see [115], one obtains the following expression for Λ:

$$\Lambda^{-1} = \left| \frac{1}{2} \frac{\int_{-1}^{1} d\varepsilon \int_{-1}^{1} d\varepsilon' \left(\ln |K_e + W_e \varepsilon| - \ln |K_a + W_a \varepsilon'| \right)}{4} \right|, \tag{4.15}$$

where an ensemble average has been used. Note that the normalization factor $1/4$ appears since the random variables ε and ε' are uniformly distributed in the interval $[-1, 1]$ as mentioned before. After performing the integration, we deduce

$$\Lambda^{-1} = \frac{1}{4} \left| \ln \left[\frac{|K_e + W_e|^{(K_e/W_e+1)}}{|K_e - W_e|^{(K_e/W_e-1)}} \frac{|K_a - W_a|^{(K_a/W_a-1)}}{|K_a + W_a|^{(K_a/W_a+1)}} \right] \right|. \tag{4.16}$$

The latter expression, which is valid for the case of chiral disorder, will be used later to indicate the critical line in the (K_a, W) parametric plane, where Λ diverges.

Complementarily, we also calculate the localization length at ω_0 employing the transfer matrix approach [123, 124]. Specifically, we can rewrite Eq. (4.1) as

$$\begin{pmatrix} u_{j+2} \\ u_{j+1} \end{pmatrix} = \mathbb{T}_j \begin{pmatrix} u_{j+1} \\ u_j \end{pmatrix}, \tag{4.17}$$

and get the transfer matrix $\mathbb{T}_j$ given by

$$\mathbb{T}_j = \begin{pmatrix} \dfrac{k_{j+2}+k_{j+1}+k_{j+1}^0-m\omega_0^2}{k_{j+2}} & -\dfrac{k_{j+1}}{k_{j+2}} \\ 1 & 0 \end{pmatrix}. \tag{4.18}$$

Then, the Lyapunov exponents γ_1 and γ_2 are calculated numerically using the typical numerical schemes described in [125, 126, 124]. We found that $\gamma_1 \approx -\gamma_2 = \gamma$. The localization length is then determined through the relation $\Lambda = \dfrac{1}{\gamma}$.

4.4 Numerical Results

4.4.1 No disorder

Before moving to the disorder study, we need to verify the aforementioned three types of real space topological invariants in a finite clean system. We consider a chain composed of $n = 250$ unit cells, i.e., 500 particles and 501 inter/intracell springs. In the following numerical simulations, we fix $K_0 = 5$. First, let us look at a case with $K_e = 1$ and $K_a = 0.5$. For $K_e > K_a$, the periodic system is topological, which is characterized by a winding number $\nu = 1$. In a finite chain, we expect to see two localized edge modes exist in the topological band gap as shown in Fig. 4.2(a) [see also Fig. 4.7(a) in subsection 4.5.2 for the whole spectrum]. The red and blue dots represent the two states localized on the left, $|L\rangle$, and right boundary, $|R\rangle$, respectively at the mid gap frequency ω_0. In fact, a hybrization of the edge states is expected, which leads to a frequency splitting, meaning that the two eigenfrequencies are not exactly located at ω_0 but at ω_0^+ and ω_0^- (the two corresponding eigenstates are approximated as: $|\omega_0^+\rangle = \frac{e^{-i\phi/2}|L\rangle+e^{i\phi/2}|R\rangle}{\sqrt{2}}$ and $|\omega_0^-\rangle = \frac{e^{-i\phi/2}|L\rangle-e^{i\phi/2}|R\rangle}{\sqrt{2}}$ for some ϕ) [127]. However, for large system sizes, as in our case, one can consider that the energy splitting is sufficiently small, and thus we have a "degeneracy" of the eigenstates $|L\rangle$ and $|R\rangle$ at ω_0. The shapes of the localized edge modes are shown in the insets of Fig. 4.2(a). Note that the two localized edge modes have a characteristic profile with only sites from one sub-lattice excited (either j even or odd). This is a well-known consequence of the chiral symmetry. As we increase K_a to 1.5, the system becomes trivial with a winding number being zero, where the localized edge modes do not exist anymore [see Fig. 4.2(b) and Fig. 4.7(b) in subsection 4.5.2].

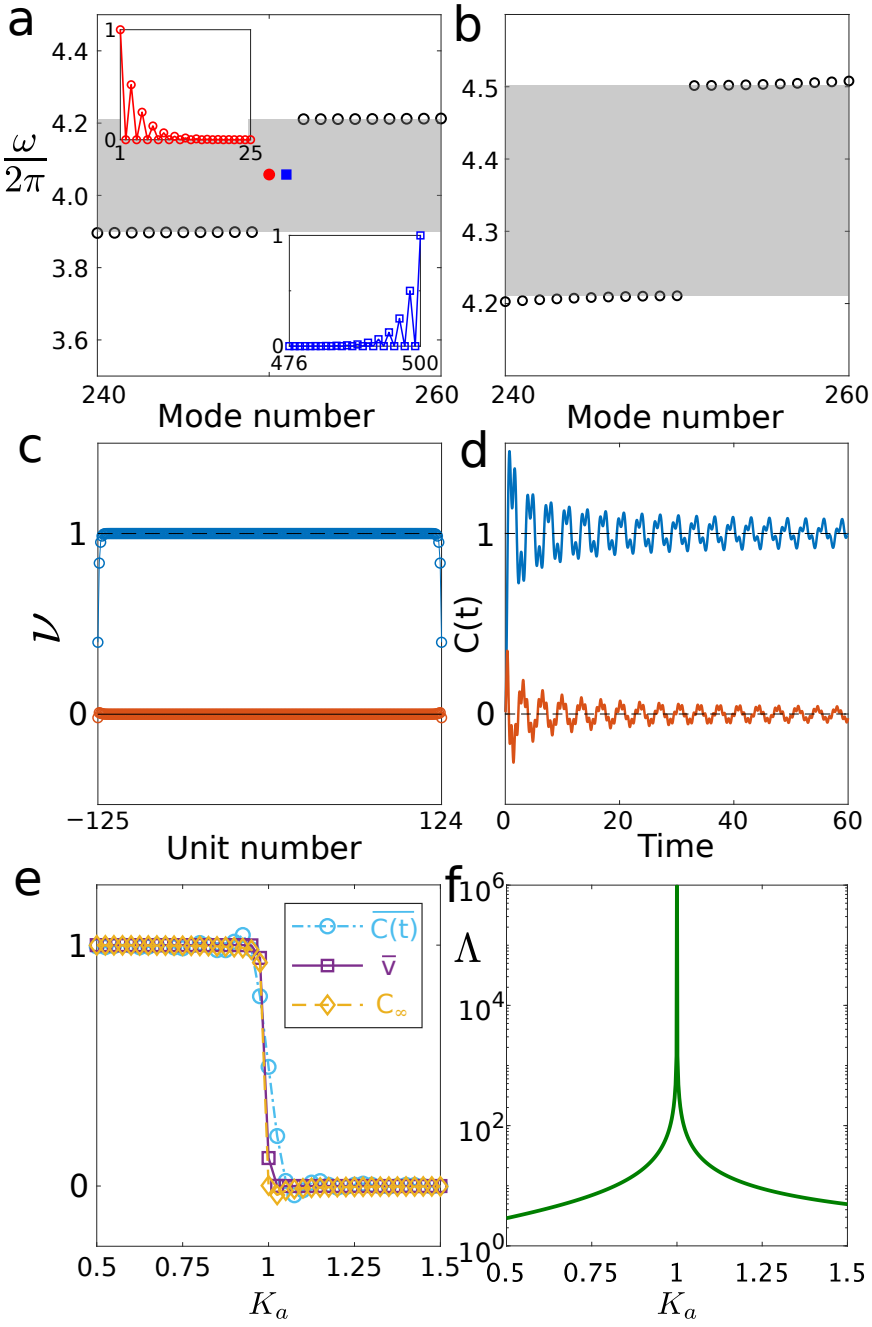

Figure 4.2: Eigenfrequencies for a finite (a) topologically nontrivial and (b) trivial 1D spring-mass chain. Shapes of the topological edge modes are shown in the inset of (a). The grey areas represent the band gaps. (c) LTM calculated from the eigenmodes of the nontrivial (blue) and trivial (red) system. (d) Time-dependent MCD for the nontrivial (blue) and trivial (red) under initial displacement excitation. (e) Evolution of three kind of real space topological invariants during a topological transition. (f) Localization length of the eigenmode at the frequency ω_0.

Based on the eigenmodes obtained from Eq. 4.5, we can calculate the LTM of the system as defined in Eq. (4.10). Figure 4.2(c) shows the calculated LTM as a function of the unit cell number in the topologically nontrivial (red line) and trivial cases (blue line), respectively. As we see, the LTM is well quantized to either zero or one in the bulk of the chain, while approaching the boundary, it deviates from the theoretical value. To overcome such boundary effect, we take the average value over 100 unit cells in the middle of the chain, noted as $\bar{\nu}$. We then get $\bar{\nu} = 1$ for the nontrivial and $\bar{\nu} = 0$ for the trivial configurations. Similarly, by plugging the eigenmodes into Eq. (4.13), we obtain the IMCD, which are $C_{\text{inf}} = 1$ and $C_{\text{inf}} = 0$ for nontrivial and trivial configurations, respectively. To derive the time-dependent MCD, we take the initial displacement $u_{251}(0) = 0.1$ and perform transient simulations. After normalizing the time-history response at each time t and plugging this in Eq. (4.11), we get the MCD as a function of time. Figure 4.2(d) demonstrates its evolution in a nontrivial (blue curve) or trivial (red curve) system. It is clear that the MCD oscillates and tends to converge to 1 (0) in a topologically nontrivial (trivial) system despite the oscillations. We conduct the time average from $t = 0$ to $t = 60$ to eliminate the influence of fluctuations, which gives $\bar{C}(t) = 1$ [$\bar{C}(t) = 0$]. The time window is selected to avoid possible wave reflections at the system boundaries.

In these two cases, all three topological invariants are closely quantized to 0 or 1, which shows a great agreement with the theoretical winding number of an infinite system defined in the momentum space. Figure 4.2(e) summarizes the evolution of the different topological invariants during an *in situ* topological phase transition. During the process, we vary K_a from 0.5 to 1.5 with a 0.025 step while keeping $K_e = 1$. Clearly, all three kinds of real space topological invariants agree well with each other and can accurately probe the topological phase transition in a clean 1D mechanical system, which happens when the gap closes, namely at $K_a = K_e = 1$. Finally, in Fig. 4.2(f), we also plot the the localization length of the edge modes as we vary the coupling K_a from 0.5 to 1.5, which is given by the analytical expression $\Lambda = \frac{2}{|\ln(K_a/K_e)|}$.

Notice that at the point where the topological transition occurs, i.e., $K_a = K_e = 1$, the localization length diverges. This is expected since, as we mentioned, the topological transition occurs when the gap closes and thus the edge mode transforms to an extended mode.

4.4.2 Chiral disorder

In this subsection, we explore the topological phase transition of a spring-mass system induced by the chiral disorder with the dynamical matrix $\mathbb{D}^I$. Figure 4.3(a) shows the numerically calculated LTM as a function of the intracell spring stiffness K_a and the disorder strength $W = W_a = 2W_e$ under chiral disorder. We again choose $K_e = 1$. Each data point is a disorder-averaged result over 250 realizations. Evidently, the surface map can be approximately divided into two regions separated by a blurry white boundary. The region with a red (blue) tone has topological marker close to 1 (0) corresponding to a topologically nontrivial (trivial) system. In most real mechanical systems, the spring stiffness tends to be positive. The black dashed lines follow the relation given by $\min(|K_e - W_e|, |K_a - W_a|) = 0$ for sufficiently large K_0. Therefore, only the area on the left of the dashed black line in the surface plot could be realized without the necessity of negative-stiffness springs. However, note that by tuning the disorder ratio (W_e/W_a), we can further shift the topological phase diagram and change the critical boundary (see subsection 4.5.3 for more detail). Note also that effective negative-stiffness springs can be designed utilizing the symmetry of modes and a sophisticated geometry of the coupling of the neighbor particles, look for example refs. [128] and [129] for an implementation of negative hoppings in elastic and acoustic systems, respectively.

Figure 4.3(b) shows the localization length at ω_0, obtained numerically using the transfer matrix method, as a function of the same parameters (K_a and W). We note here that the transfer matrix was iterated 10^6 times at each point of Fig. 4.3(b). The solid black curve shown in Figs. 4.3(a) and 4.3(b) indicates the critical boundary obtained by the analytical diverging line from Eq. (4.16). It is clear that the numerical solutions [blurry white regions in Fig. 4.3(a) and highlighted area in Fig. 4.3(b)] match with the analytical results (solid black curve). This denotes that the topological phase transition is related with a critical point at which the localization length diverges.

Figure 4.3(c) shows the evolution of the topological marker with the increase of the disorder strength for $K_a = 0.6$, which corresponds to the yellow line in Fig. 4.3(a). In the clean limit ($W = 0$), this finite system is nontrivial with a topological marker of $\bar{\nu} = 1$. As expected, the topological marker remains constant in the presence of weak and medium level disorder, as the

topological properties of this system are protected by the chiral symmetry and the topological edge modes are immune to weak disorder. However, when the disorder strength rises and reaches a sufficiently large amount, the topological marker falls sharply and eventually stabilizes near zero under strong disorder, which indicates a transition process from a topologically nontrivial system to a trivial one. We also notice that the disorder-averaged results show larger standard deviation in this region, which is reasonable in strong disorder. Disorder-averaged mean values of MCD and IMCD are marked by the crosses and circles in Fig. 4.3(c), respectively. See subsection 4.5.4 for typical time-history responses of the 1D spring mass chain under different levels of disorder. All three kinds of topological invariants, therefore, show good agreement in capturing the general trends of disorder-induced topological transition. For the time-history response, note that negative stiffness of intersite or onsite springs caused by the strong disorder does not necessarily lead to dynamical instability of our system. Within the disorder ranges that we are interested in, our system remains stable (See subsection 4.5.5 for more details).

For $K_a = 1.05$ [green line in Fig. 4.3(a)], however, we observe a more sophisticated topological phase transition process, as shown in Fig. 4.3(d). The system is trivial with $\bar{\nu} = 0$ when there is no disorder. For very weak disorder $W < 0.3$, the topological marker remains near zero. However, as we introduce stronger disorder, the topological marker surprisingly surges up to reach a plateau ($\bar{\nu} \approx 0.98$) which is very close to 1 (not exactly 1 due to finite size). If we keep increasing the disorder strength, it drops again close to zero. This procedure is particularity interesting since we demonstrate a two-way transition by purely increasing disorder in the system. The spring-mass chain starts as a trivial system, then changes into a nontrivial one and finally becomes a trivial Anderson insulator. The MCD and IMCD results as marked with crosses and circles in Fig. 4.3(d) also corroborate the LTM trend. Therefore, the intermediary nontrivial state is the realization of a mechanical analogue to the TAI.

So far, we have quantitatively demonstrated the topological phase transitions by tracking the real-space topological invariants. Now we investigate their characteristics in more details. We choose the configuration of the system that supports the TAI phase, i.e., with $K_a = 1.05$ and $K_e = 1$ in Fig. 4.3(d) and analyze its eigenfrequencies and modes as a function of disorder strength.

Figures 4.4(a)-4.4(c) show the eigenfrequencies of a finite chain under one realization with disorder strengths $W = 0.25$, $W = 1.25$, and $W = 2.5$. The grey regions represent the topological band gaps in the clean ($W = 0$) case. After we introduce disorder in the system, the topological band gap shrinks in the regime of weak disorder [Fig. 4.4(a) for $W = 0.25$] and is eventually closed under strong disorder [see Figs. 4.4(b) and 4.4(c) for $W = 1.25$ and $W = 2.5$, respectively]. We then plot the shapes of the center modes (250th and 251st) in Figs. 4.4(d)-4.4(f). We find that for weak disorder ($W = 0.25$), the modes are quite extended. Of course, as the disorder strength increases, the modes become spatially strongly localized.

The TAI phase ($W = 1.25$) is distinct in a way that the localized modes appear on the boundaries of the system as in a nontrivial system, whereas the localized modes need not be at the boundaries for an Anderson insulator ($W = 2.5$) and reside at the same location with only phase differences at some particles.

We further demonstrate the validity of this statement for all disorder realizations by defining the Center of Mode (COM) as

$$\mathrm{COM} = \frac{\sum_{i=1}^{N} x_i u_i^2}{\sum_{i=1}^{N} u_i^2} \tag{4.19}$$

where x_i and u_i denote the position and displacement of the ith mass. We study the statistical distribution of the COM for 1000 disorder realizations. Figures 4.4 (g)-4.4(i) show the histograms of the COM of the 250th and 251st modes under chiral disorder for varying disorder strengths. This agrees with the topological phase diagram [see Fig. 4.3(d)] and the eigen analysis [Figs. 4.4 (d)-4.4(f)]. When the system is with weak ($W = 0.25$) and strong ($W = 2.5$) disorder, the 250th and 251st modes are likely to be all along the chain; however, for the TAI phase ($W = 1.25$), the modes are most likely localized at the boundaries [Fig. 4.4 (h)]. A similar inference can be made for the configuration with $K_a = 0.6$ and $K_e = 1$ and that has been included in subsection 4.5.6.

4.4.3 Random disorder

We now discuss the effect of random disorder on topology by removing the disorder on the onsite ground springs. As given in Eq. 4.9, the diagonal entries of the random disordered stiffness matrix are not identical anymore, which leads to the breaking of the system's chiral symmetry. Since the topology in the 1D SSH model is mainly protected by the chiral symmetry, we expect to see a stronger influence of the random disorder over topology.

Figure 4.5(a) shows the topological phase diagram under random disorder with $W = W_a = 2W_e$. It is clear that the topological states can only survive much weaker random disorder compared to the chiral one. Moreover, Fig. 4.5(b) shows the localization length at ω_0, and in contrast to the case of chiral disorder there is no signature of the localization length divergence at this frequency, which also contributes to the uncertainty of the clear phase transition due to non-chiral disorder.

Furthermore, even with very small amount of disorder, we see that the topological marker deviates from the quantized value as shown in Fig. 4.5(c). As we expected, breaking the chiral symmetry leads to the variation of the real space topological marker, which is not well quantized to an integer value but tends to saturate near a decimal between 0 and 1. This leave us an open question whether it is appropriate to discuss the concept of topology in a 1D mechanical system in absent of the chiral symmetry. If so, what kind of quantities or phenomena should we use to characterize the topological properties in these cases?

Despite the lack of a theoretical framework, we try to extend the eigen analysis and COM statistical study to examine the relation between random disorder and the topological indicators in a 1D system. Figures 4.6(a)-4.6(c) show the eigenfrequencies around the center of the frequency spectrum of a finite chain ($K_a = 0.6$) under random disorder with strength $W = 0.25$, $W = 1.25$, and $W = 2.5$, respectively. The grey regions represent the topologically nontrivial band gaps in the clean ($W = 0$) case. It is clear that the random disorder causes more drastic change of the frequency spectrum. Especially, the two center modes no longer share a common frequency and may shift out of the original bandgap region. Despite the frequency variations, the two center modes of the system under weak ($W = 0.25$) random disorder are still localized modes existing at the boundary

[Figs. 4.6(d)-4.6(i)], which is the key character of the topological edge states. This is consistent with the topological invariant calculation, which is very close to 1 in this configuration [see the yellow line in Fig. 4.5(c)]. As we increase the disorder level, these center modes start to move into the bulk. More interestingly, the two center modes tend to localize at different positions in the chain, which is different from the trivial chiral disordered system where the two modes exist at the same location [Fig. 4.4(f)]. A similar trend can also be observed for the disordered study in the case of $K_a = 1.05$ (subsection 4.5.6). Finally, in Figs. 4.4(g)-4.6(i) we show the histograms of the COM of the central modes under random disorder for varying disorder strengths. For weak ($W = 0.25$) disorder, the 250th and 251st modes are likely to be localized at the boundaries, while for strong ($W = 1.25$ and $W = 2.5$) disorder (both in the trivial Anderson phase) they can be localized all along the chain.

4.5 Additional discussion

4.5.1 Definition of the chiral operator and position operator

For a 1D system with $n = 250$ unit cells, that is $N = 2n = 500$ particles, we first define the unit cell numbers as $l = [-125, -124, \cdots, 0, \cdots, 123, 124]$. Then the chiral operator and position operator are given as

$$\Gamma = \begin{bmatrix} 1 & 0 & 0 & 0 & \cdots \\ 0 & -1 & 0 & 0 & \cdots \\ 0 & 0 & 1 & 0 & \cdots \\ 0 & 0 & 0 & -1 & \cdots \\ \vdots & \vdots & \vdots & \vdots & \ddots \end{bmatrix}_{N\times N}, \tag{4.20}$$

$$\Gamma_A = \begin{bmatrix} 1 & 0 & 0 & 0 & \cdots \\ 0 & 0 & 0 & 0 & \cdots \\ 0 & 0 & 1 & 0 & \cdots \\ 0 & 0 & 0 & 0 & \cdots \\ \vdots & \vdots & \vdots & \vdots & \ddots \end{bmatrix}_{N\times N} ,\Gamma_B = \begin{bmatrix} 0 & 0 & 0 & 0 & \cdots \\ 0 & 1 & 0 & 0 & \cdots \\ 0 & 0 & 0 & 0 & \cdots \\ 0 & 0 & 0 & 1 & \cdots \\ \vdots & \vdots & \vdots & \vdots & \ddots \end{bmatrix}_{N\times N} , \tag{4.21}$$

$$\mathbb{X} = \begin{bmatrix} -125 & 0 & 0 & 0 & \cdots & 0 & 0 \\ 0 & -125 & 0 & 0 & \cdots & 0 & 0 \\ 0 & 0 & -124 & 0 & \cdots & 0 & 0 \\ 0 & 0 & 0 & -124 & \cdots & 0 & 0 \\ \vdots & \vdots & \vdots & \vdots & \ddots & \vdots & \vdots \\ 0 & 0 & 0 & 0 & \cdots & 124 & 0 \\ 0 & 0 & 0 & 0 & \cdots & 0 & 124 \end{bmatrix}_{N\times N} . \tag{4.22}$$

4.5.2 Spectrum

In Fig. 4.7, we show *all* the eigenfrequencies of a clean chain of 500 particles for both topologically trivial and nontrivial phases. These are the same cases as shown in Fig. 4.2(a) and 4.2(b) of the main text.

4.5.3 Topological phase diagram with different combinations of disorder strength

In Section 4.4, we discuss the disorder configuration with specific ratio $W = W_a = 2W_e$. Here, we briefly explore the effect of disorder ratio (W_e/W_a) by studying the topological transitions in the presence of chiral disorder with different combination of W_a and W_e. Figures 4.8(a)-4.8(c) show the topological phase diagrams under chiral disorder with (a) $W = W_a$ and $W_e = 0$, (b) $W = W_a = 4W_e$, and (c) $W = W_a = 0.5W_e$. It is clear that by changing the disorder ratio (W_e/W_a), we can shift the critical boundaries for the disorder-induced topological transitions.

4.5.4 Spatiotemporal diagrams in disordered systems

Figures 4.9(a)-4.8(d) show the typical time-history responses of the 1D spring mass chain with chiral disorder under strength $W = 0$, $W = 0.25$, $W = 1.25$, and $W = 2.5$, respectively. In a periodic system ($W = 0$), the energy is evenly spreading to both sides of the system after the initial disturbance in the middle of the chain, as shown in Fig. 4.9(a). With the increase of disorder strength, we start to see more and more localization of the energy in the system due to Anderson localization.

4.5.5 Stability of disordered systems

The dynamics of our system is governed by Eq. (4.2). For the stability of this system, the dynamical matrix must be positive definite, implying that all the eigenvalues (ω^2) are positive. In Fig. 10, we show the stability diagram under chiral disorder that corresponds to the case shown in Fig. 3(a) of the main text. This highlights the probability of the dynamical matrix being positive definite with varying system parameters. We can therefore conclude that our system remains stable within the disorder range we are interested in ($W < 3$).

4.5.6 Some other cases of chiral and random disorder

To have a comprehensive understanding of the topological transition process, we study two extra cases with chiral and random disorders, respectively. In Fig. 4.11, we study a spring-mass chain with configuration $K_a = 0.6$ and $K_e = 1$ under *chiral* disorder, which corresponds to Fig. 4.3(c). Similarly, Fig. 4.12 shows the results of a system with configuration $K_a = 1.05$ and $K_e = 1$ under *random* disorder corresponding to the green curve in Fig. 4.5(c).

4.6 Conclusion

In this work, we explore the disorder-induced topological phase transitions in a spring-mass chain. To probe the topological property in a disordered 1D mechanical system, we use three kinds of topological invariants obtained from the real space wave functions to work as an effective winding number. We introduce two types of disorder, chiral and random, to study their influences on the

topology in a mechanical system. Under the chiral disorder, we not only demonstrate the transition from topological to trivial, but also the abnormal reverse transformation leading to the realization of so-called Topological Anderson Insulator (TAI) in a mechanical setup. However, for the case of random disorder, we do not observe similar TAI phenomena. Instead, we find that the random disorder suppresses the topological property, as it breaks the internal system symmetry that protects the topology. Our findings can be extended to higher dimensional mechanical systems to further study the interactions between disorder and topology. In addition, despite the difficulties in controlling stiffness in a disordered mechanical system, it would be very interesting to implement and experimentally verify the proposed framework in other highly tunable systems, such as electric circuits [130].

4.7 Author contributions

This chapter is adopted from the author's following publication: X. Shi, I. Kiorpelidis, R. Chaunsali, V. Achilleos, G. Theocharis, and J. Yang, Disorder-Induced Topological Phase Transition in a One-Dimensional Mechanical System, Phys. Rev. Research 3, 033012 (2021). [131] X. Shi and J. Yang conceived the idea of the project. X. Shi performed the numerical simulations. I. Kiorpelidis performed the localization length analysis. X. Shi and I. Kiorpelidis wrote the manuscript. G. Theocharis and J. Yang supervised the project. All authors interpreted the results and reviewed the manuscript.

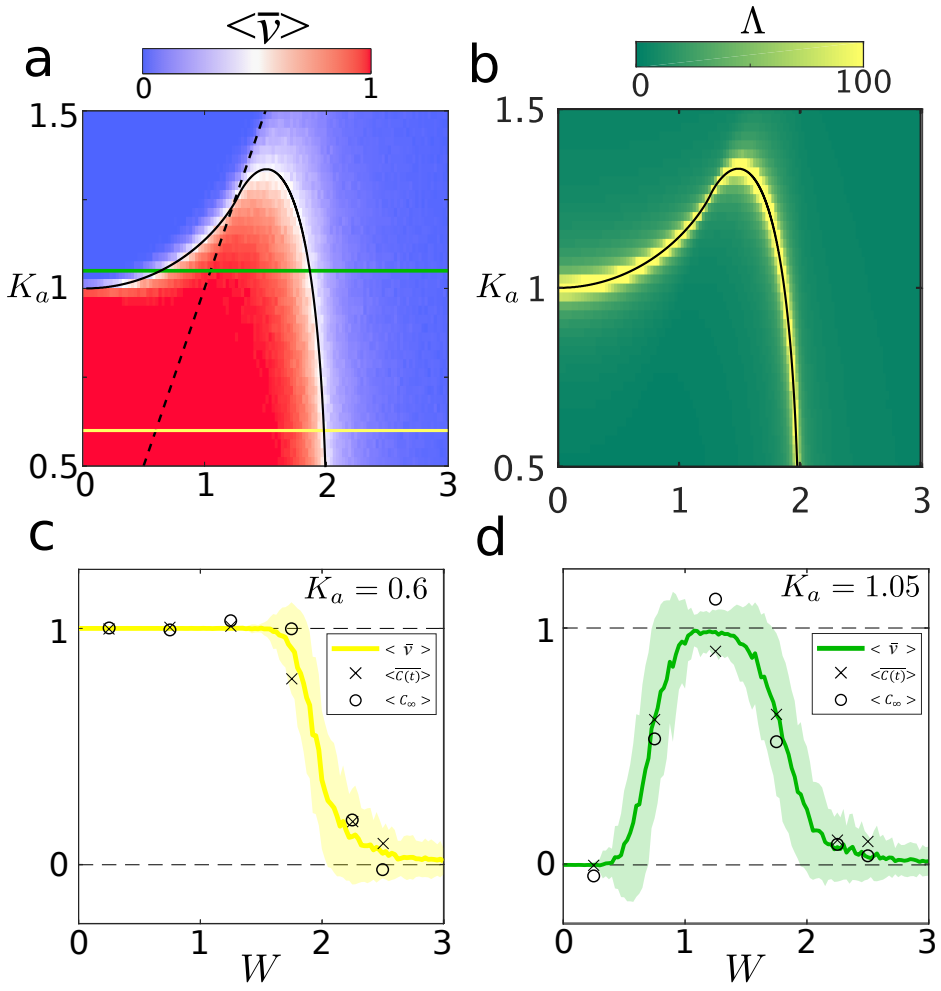

Figure 4.3: (a) Topological phase diagram under chiral disorder with disorder ratio $W = W_a = 2W_e$. Colorbar ranging from 0 to 1 stands for the LTM averaged over 250 disorder realizations. (b) The localization length at the mid gap frequency, $\Lambda(\omega_0)$ from the transfer matrix method (colormap) and the analytical expression. (c) and (d) The evolution of topological markers with the increase in disorder strength for $K_a = 0.6$ [yellow line in (a)] and 1.05 [green line in (a)], respectively. The lines and shaded area represent the mean and standard deviation of the LTM. The cross and sphere markers indicate the mean of MCD and IMCD.

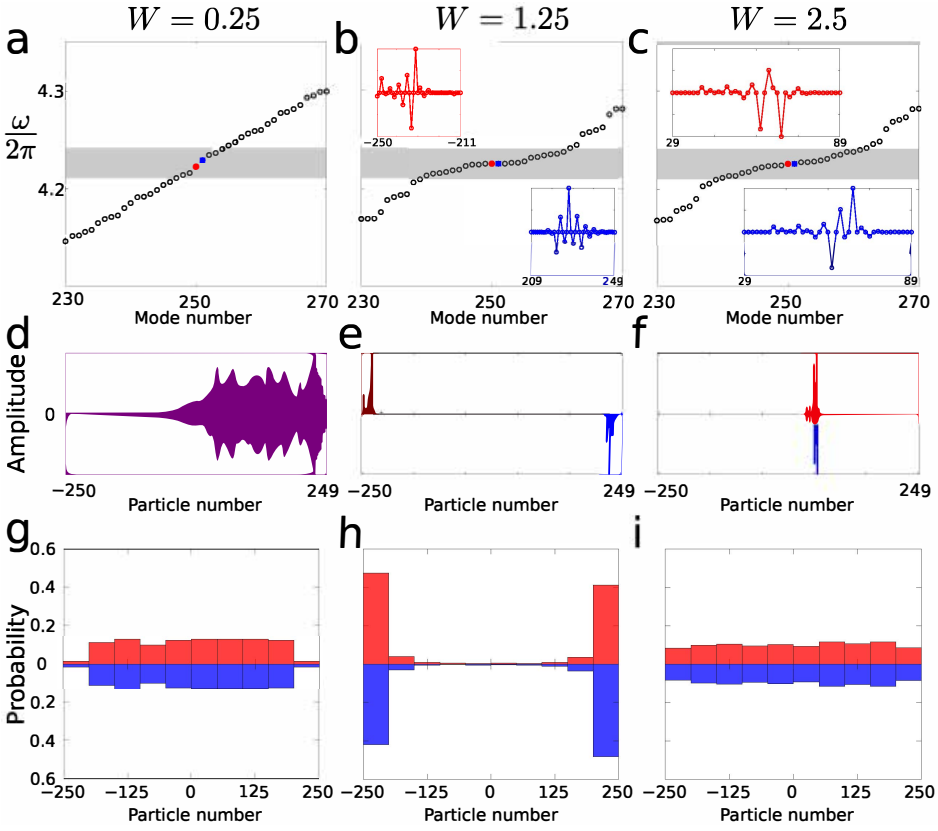

Figure 4.4: Eigen-frequencies and two modes in the center of frequency spectrum of a finite spring-mass chain ($K_a = 1.05$ and $K_e = 1$) under *chiral* disorder with disorder ratio $W = W_a = 2W_e$ for (a) $W = 0.25$, (b) $W = 1.25$ (TAI phase), and (c) $W = 2.5$. These correspond to three typical realizations with different disorder strengths in Fig. 4.3(d). Chiral nature of the two edge modes lying at the center of band gap is shown in the insets. (d)–(f) Spatial profile of these two modes for one disorder realization. (g)-(h) Histogram of the Center of Mode (COM) obtained by 1000 disorder realizations, describing the probability of COM lying in 50 particle interval throughout the chain.

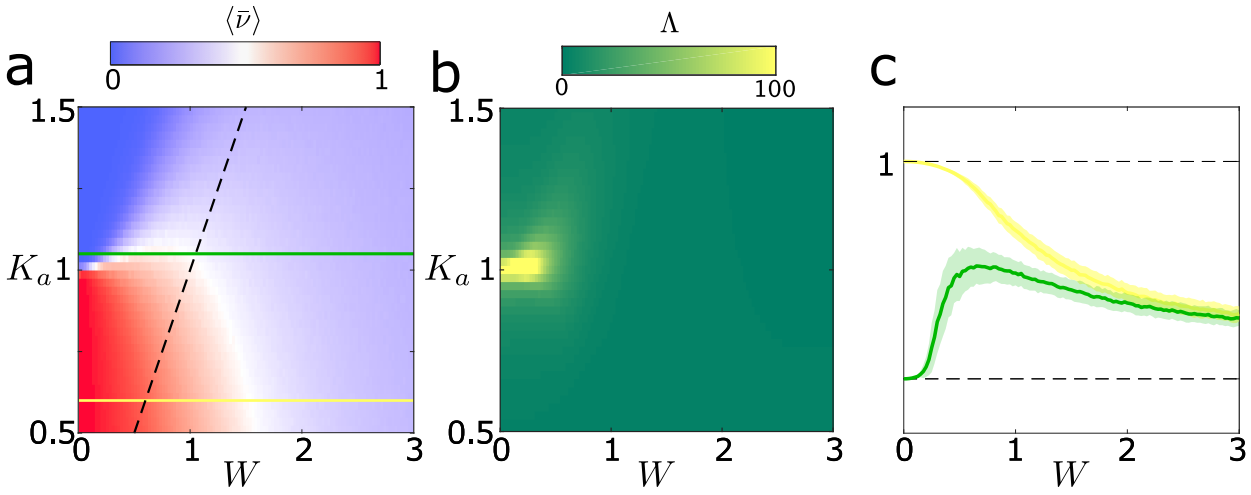

Figure 4.5: (a) Topological phase diagram under random disorder with disorder ratio $W = W_a = 2W_e$. Colorbar ranging from 0 to 1 stands for the LTM averaged over 250 disorder realizations. (b) Localization length $\Lambda(\omega_0)$ under random disorder. The transfer matrix was again iterated 10^6 times at each point. (c) The evolution of topological marker with increase of disorder for $K_a = 1.05$ (green) and $K_a = 0.6$ (yellow). The shaded area shows the standard deviation.

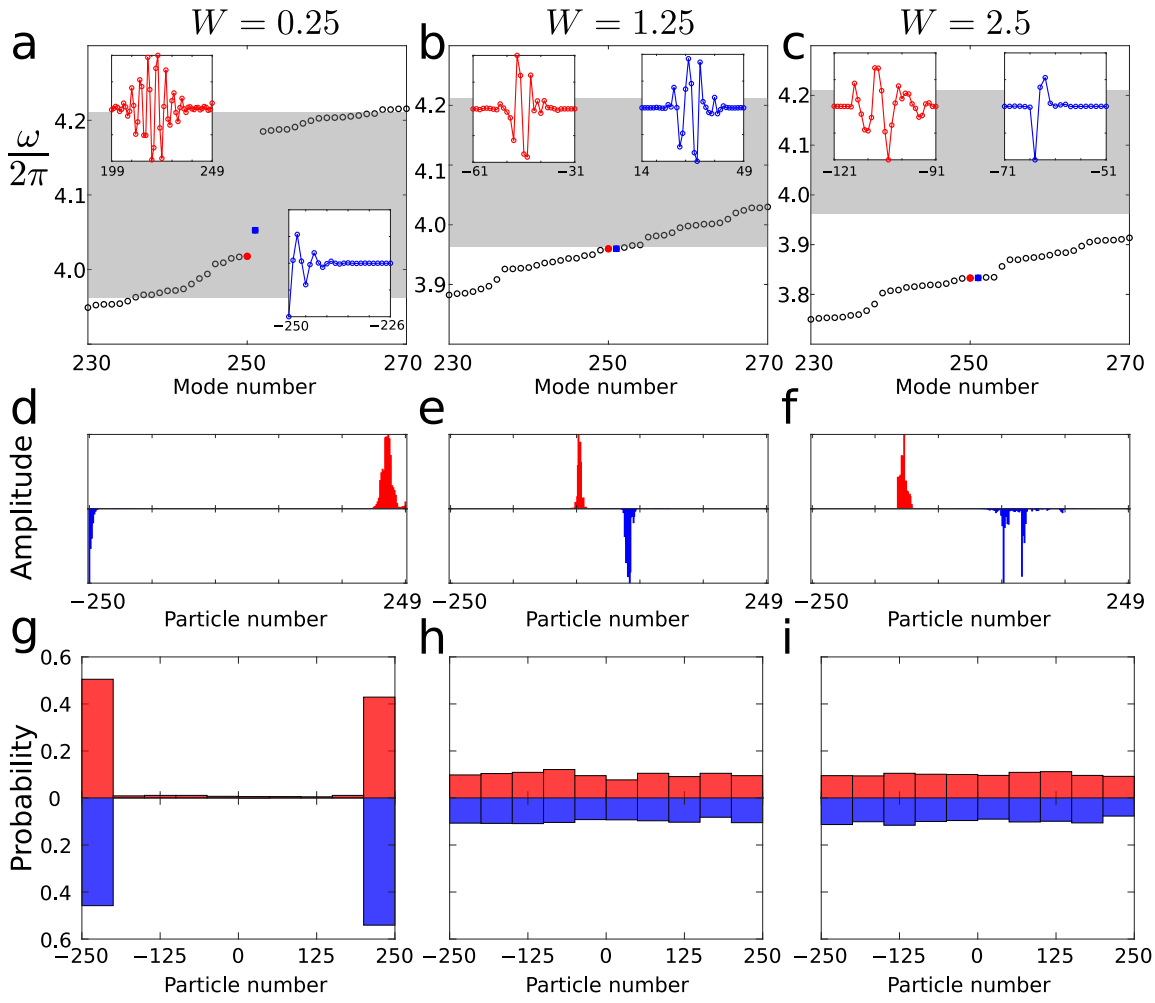

Figure 4.6: Eigen-frequencies and two modes in the center of frequency spectrum of a finite spring-mass chain ($K_a = 0.6$ and $K_e = 1$) under *random* disorder with disorder ratio $W = W_a = 2W_e$ for (a) $W = 0.25$, (b) $W = 1.25$, and (c) $W = 2.5$. These correspond to three typical realizations with different disorder strengths on the yellow curve in Fig. 4.5(c). Non-chiral nature of the two modes (marked) is shown in the insets. (d)–(f) Spatial profile of these two modes for one disorder realization. (g)-(h) Histogram of the Center of Mode (COM) obtained by 1000 disorder realizations, describing the probability of COM lying in 50 particle interval throughout the chain.

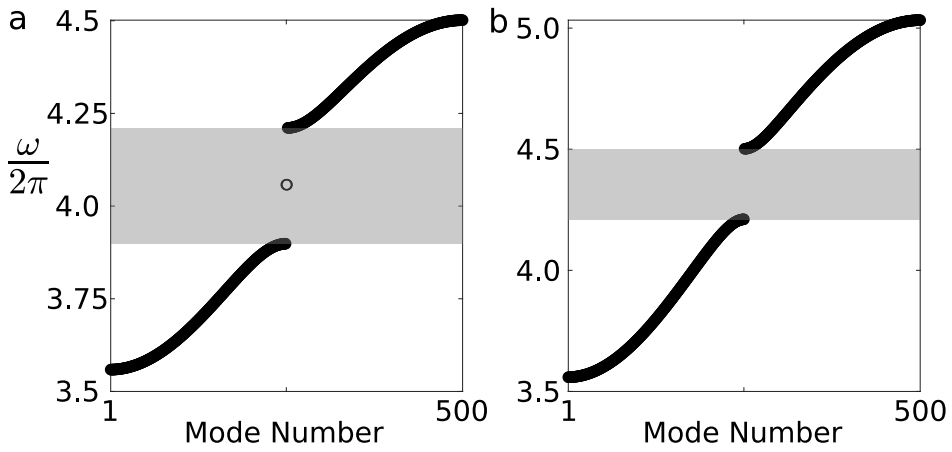

Figure 4.7: The eigenfrequencies of a chain of 500 particles for the topological nontrivial phase (left panel, $K_e = 1$, $K_a = 0.5$) and trivial case (right panel, $K_e = 1$, $K_a = 1.5$). For both cases, $K_0 = 5$. Band gap is highlighted with the shaded area.

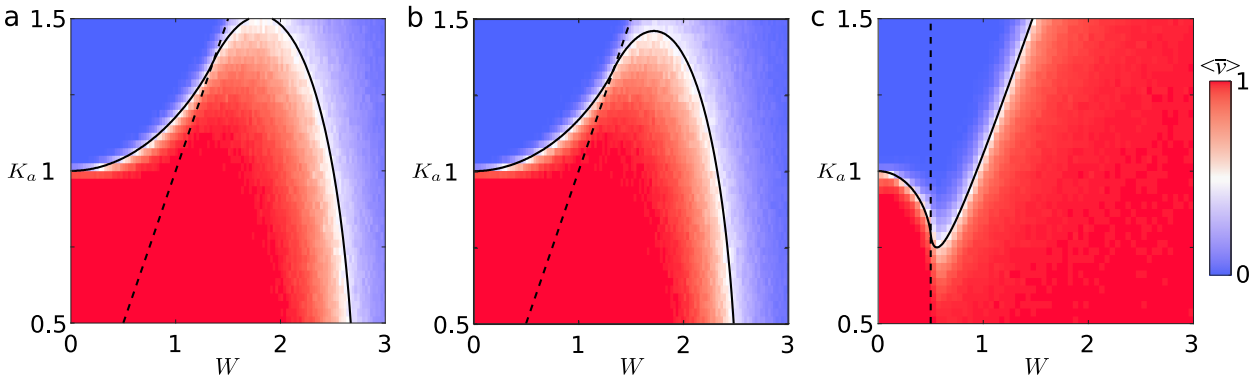

Figure 4.8: Topological phase diagram under chiral disorder with different combination of W_a and W_e. (a) $W = W_a$ and $W_e = 0$, (b) $W = W_a = 4W_e$, and (c) $W = W_a = 0.5W_e$. The solid black line indicates the divergence of the localization length obtained analytically. The dashed line separates the region of negative stiffness.

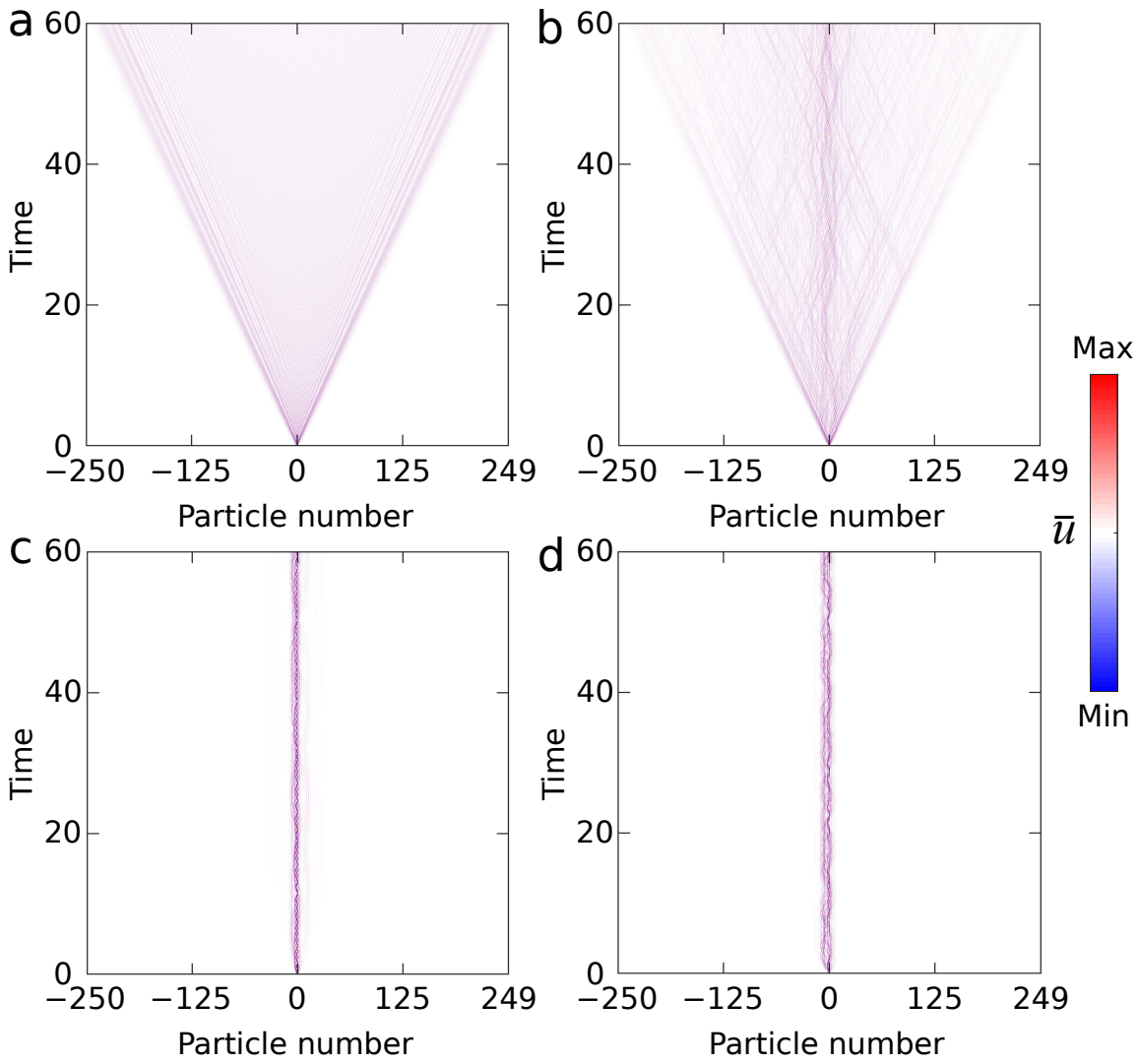

Figure 4.9: Spatio-temporal evolution of particle displacement ($K_a = 0.6$ and $K_e = 1$). We use chiral-disorder strengths (a) $W = 0$, (b) $W = 0.25$, (c) $W = 1.25$, and (d) $W = 2.5$.

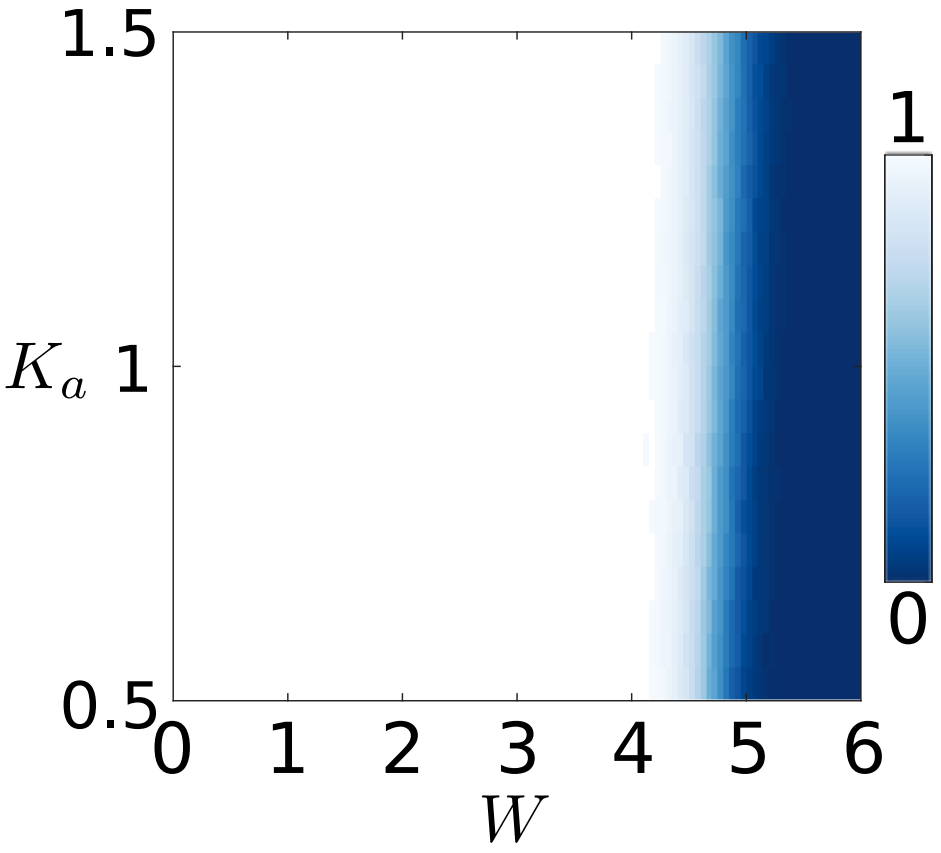

Figure 4.10: Stability diagram of the 1D system as a function of K_a and W under the chiral disorder. Colorbar ranging from 0 to 1 stands for the probability (over 1000 disorder realizations) of the dynamical matrix being positive-definite.

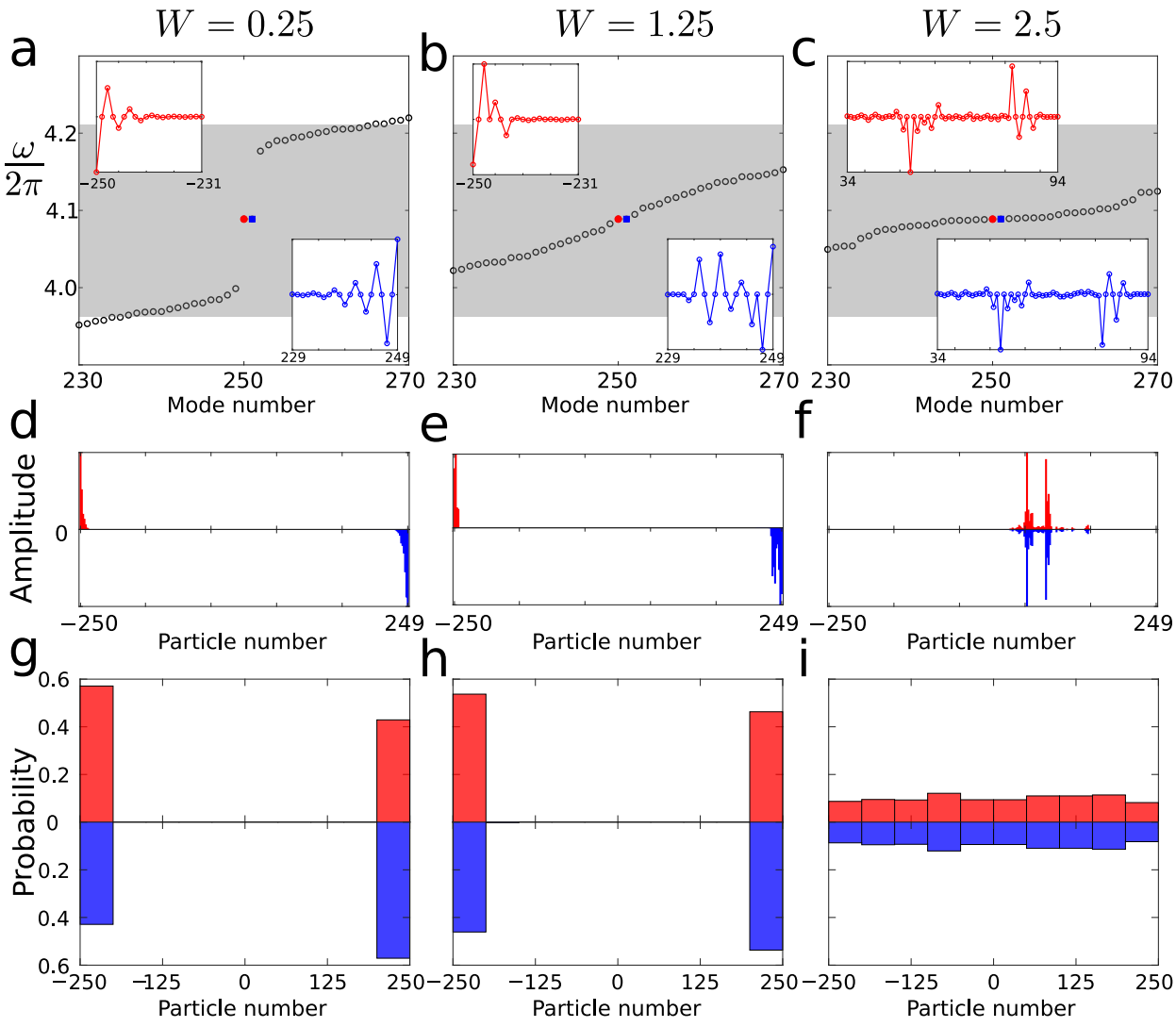

Figure 4.11: Eigen-frequencies and two modes in the center of frequency spectrum of a finite spring-mass chain ($K_a = 0.6$ and $K_e = 1$) under *chiral* disorder with disorder ratio $W = W_a = 2W_e$ for (a) $W = 0.25$, (b) $W = 1.25$, and (c) $W = 2.5$. These correspond to three typical realizations with different disorder strengths in Fig. 4.3(c). Chiral nature of the two edge modes lying at the center of band gap is shown in the insets. (d)–(f) Spatial profile of these two modes for one disorder realization. (g)-(h) Histogram of the Center of Mode (COM) obtained by 1000 disorder realizations, describing the probability of COM lying in 50 particle interval throughout the chain.

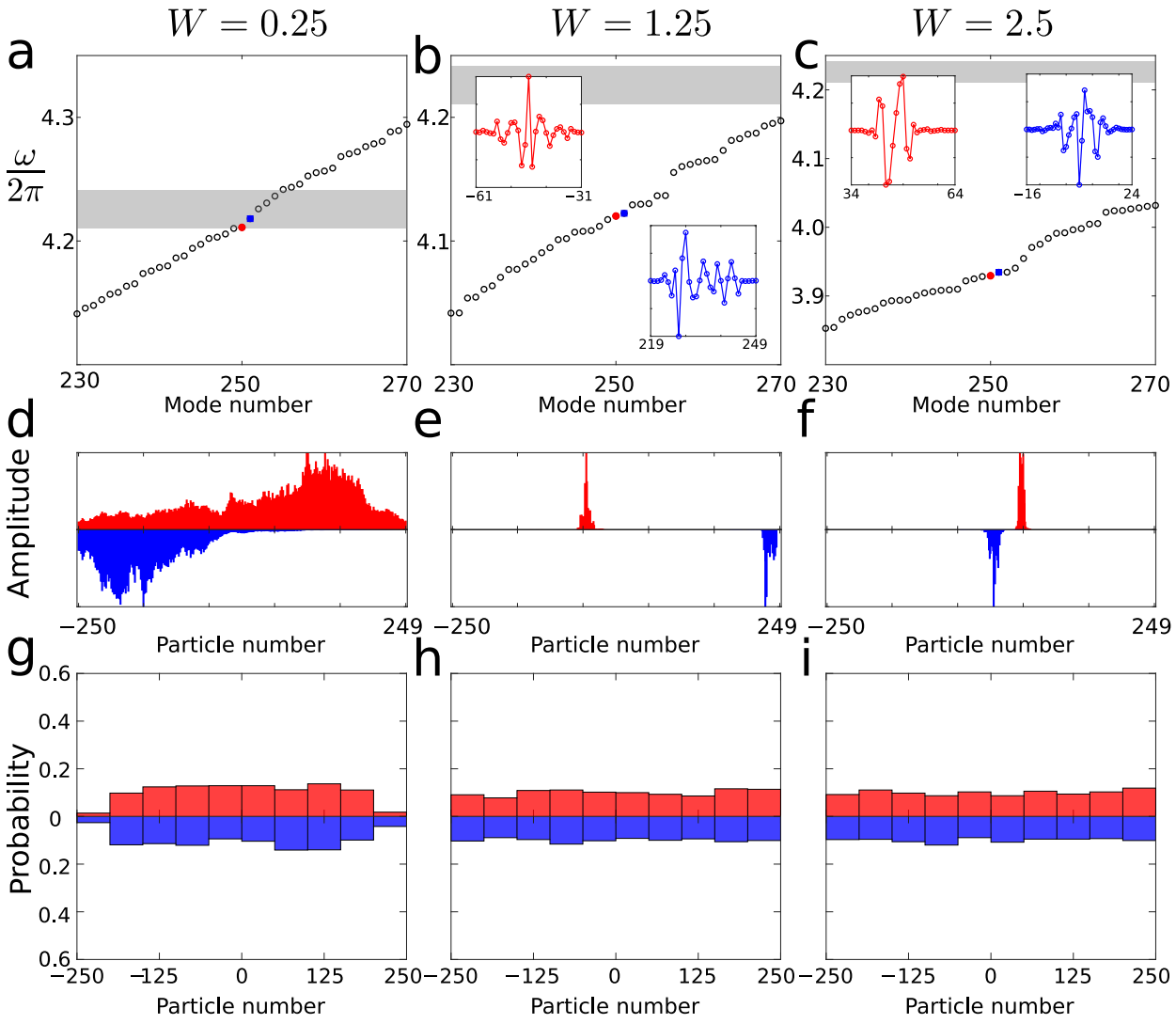

Figure 4.12: Eigen-frequencies and two modes in the center of frequency spectrum of a finite spring-mass chain ($K_a = 1.05$ and $K_e = 1$) under *random* disorder with disorder ratio $W = W_a = 2W_e$ for (a) $W = 0.25$, (b) $W = 1.25$, and (c) $W = 2.5$. These correspond to three typical realizations with different disorder strengths on the green curve in Fig. 4.5(c). Non-chiral nature of the two modes (marked) is shown in the insets. (d)–(f) Spatial profile of these two modes for one disorder realization. (g)-(h) Histogram of the Center of Mode (COM) obtained by 1000 disorder realizations, describing the probability of COM lying in 50 particle interval throughout the chain.

Chapter 5

TOPOLOGICAL PHASE TRANSITION IN 2D DISORDERED ELASTIC QUANTUM SPIN HALL SYSTEM

We investigate the effect of disorder on topologically nontrivial states in a two dimension (2D) mechanical system. We first propose a quantum spin Hall (QSH) insulator based on an out-of-plane spring-mass model and analytically study the interplay between the disorder and topology in both topologically trivial and nontrivial systems. We adopt the spin Bott index to characterize the topological property in disordered mechanical systems. By tracking the evolution of the spin Bott index with the increase of disorders, we quantitatively demonstrate the disorder induced transition from a topologically nontrivial QSH insulator to a trivial insulator. We then validate the topological phase transition through transient analysis in discrete lattices. Finally, we design a phononic crystal based on the discrete spring-mass model and numerically verify the topologically protected states along the boundary between the trivial insulator and disordered topological QSH insulator in a continuous system. This work puts a step forward in understanding the role of disorder in a 2D topological classical system.

5.1 Introduction

The discovery of topological insulators (TI) [51, 50] opened a new era for studies in condensed matter physics. The key feature of a TI is the robust and directional flow of energy at the boundary of the system, which promises a powerful tool for the design of low-dissipative devices. In general, the topological insulators can be classified into two kinds, those that break the time-reversal (TR) symmetry (e.g., the quantum Hall (QH) insulator [19, 132]) and those that preserve the time-reversal symmetry (e.g., the quantum spin Hall (QSH) insulator [23, 24] and the quantum valley Hall (QVH) insulator [133, 134]). As the former type usually requires additional efforts such as the

strong external magnetic fields to support topological states, the TR-symmetry preserved system is more practical to realize, thus drawing significant attention recently.

The QSH effect can be regarded as the effect of two coupled quantum Hall states with opposite Chern numbers for each spin. Taking advantage of the spin-orbit coupling [24], the QSH system can support robust helical edge modes even in the absence of magnetic fields. However, due to the lack of intrinsic spin, it is not straightforward to realize the quantum spin hall phase in classic wave systems which are composed of spin-less particles. In order to generate such a pseudospin degree of freedom, Wu *et al*. introduced the zone-folding technique and reported a topological photonic crystal with C_6 lattice symmetry [35]. Afterward, similar ideas have been applied to acoustic [104] and mechanical [135] wave systems, which helped to take a great step in the development of topological metamaterials.

One of the important research directions in the study of topological insulators is to understand the effect of disorder on topology [50, 51]. Generally, the topological state is immune to weak disorder. With the increase of the disorder level in the system, the topologically nontrivial phase will eventually vanish. Such topological phase transition is intuitive to understand since the Bloch theory fails in the presence of disorder that suppresses the periodicity of the structure. Moreover, further investigations found an abnormal transition from a trivial system to a topological one solely induced by disorder, accompanied by the realization of topological Anderson insulator (TAI) [136]. Followed by the early works on phase transitions in disordered topological electronic systems [137, 41, 138, 112, 139, 140, 141, 142, 115, 113], the study on the interplay between disorder and topology also extends to other fields, such as photonic systems [45, 117, 143, 144, 145] and electric circuits [130, 146]. Research on disorder induced topological phase transition in the elastic topological system has also been reported in one dimension (1D) system. Zangeneh-Nejad. *et al*. realized the topological Anderson insulator phases in a topological sonic crystal [118]. Shi. *et al*. numerically investigated the topological phase transition in a disordered spring-mass chain [131].

Unlike the 1D systems, qualitative analysis and verification of the topological transition in two dimension (2D) elastic systems is still challenging due to the following reasons: (1) Lack of proper topological invariant in a 2D disordered system. Without explicit band structure, traditional clas-

sic topological invariants, such as the Chern number and spin Chern number, are ill-defined. (2) Difficulty in precisely manipulating the disorder in 2D topological metamaterials. Particularly, accurate mapping from disorder parameters in analytical models to a structure is not easy to achieve. Recently, Liu *et al*. reported observation of TAI in a 2D acoustic spin Chern insulator [147]. They proposed a bilayer phononic crystal with synthetic spin-orbit coupling and experimentally demonstrated disorder-driven topological spin-dependent edge states. However, disorder induced topological phase transition in other types of 2D elastic TI is still elusive. Particular, analysis of the disorder effect in zone folding induced TI, which is the most common type of classical analogy of TI, is yet to be explored.

In this work, we focus on the investigation of disorder induced topological phase transition in 2D elastic systems. First, we start with a discrete mechanical QSH insulator based on an out-of-plane spring-mass lattice. We compare different approaches to calculate the topological invariant in periodic cases and then generalize the spin Bott index to work as an effective spin Chern number to characteristic the topology of disordered elastic QSH systems. Based on that, we systematically analyze the effect of random stiffness disorder on the topology and quantitatively demonstrate the disorder induced topological phase transition. Then, we validate the analysis by comparing the transient wave fields of finite size disordered structures under pseudospin excitation. Finally, we propose a phononic crystal and verify computationally the disorder induced topological phase transition process in continuous systems.

5.2 Mechanical quantum spin Hall insulator

We start with a simple mechanical QSH model, which is composed of particles connected by springs. As shown in Fig. 5.1(a), the system is a honeycomb lattice with uniform masses ($m = 1$). Following the zone-folding mechanism [35], we choose an expanded unit cell containing 6 particles as indicated by the shaded hexagon. The distance between the nearest neighboring masses is equal to L. $\vec{a_1} = a(1,0)$ and $\vec{a_2} = a(\frac{1}{2}, \frac{\sqrt{3}}{2})$ are lattice vectors with $a = 3L$ being the lattice constant, as indicated by the red arrows in Fig. 5.1(a).

We then define springs connecting masses within a unit cell as intracell springs with stiffness

K_{in}, shown as the dashed black lines in Fig. 5.1(a). The springs linking masses of different cells are noted as intercell springs with stiffness K_{out}, shown as solid black lines in Fig. 5.1(a). Note that we will focus on the out-of-plane motion of the mass particles only. That is, each particle has just one degree of freedom. By applying Floquet Bloch boundary conditions, we can get the dynamic matrix of the unit cell given as:

$$\boldsymbol{D} = \frac{1}{m}\begin{bmatrix} K_d & -K_{in} & 0 & -K_{out}e^{i\vec{k}\vec{a}_1} & 0 & -K_{in} \\ -K_{in} & K_d & -K_{in} & 0 & -K_{out}e^{i\vec{k}(\vec{a}_1-\vec{a}_2)} & 0 \\ 0 & -K_{in} & K_d & -K_{in} & 0 & -K_{out}e^{-i\vec{k}\vec{a}_2} \\ -K_{out}e^{-i\vec{k}\vec{a}_1} & 0 & -K_{in} & K_d & -K_{in} & 0 \\ 0 & -K_{out}e^{-i\vec{k}(\vec{a}_1-\vec{a}_2)} & 0 & -K_{in} & K_d & -K_{in} \\ -K_{in} & 0 & -K_{out}e^{-i\vec{k}\vec{a}_2} & 0 & -K_{in} & K_d \end{bmatrix} \tag{5.1}$$

where $K_d = 2K_{in} + K_{out}$, $\vec{k} = (k_x, k_y)$, and $k_x(k_y)$ is the wave number in $x(y)$ direction.

The dispersion relation can be obtained by solving the eigenvalue problem given as:

$$\omega^2 \boldsymbol{D}\boldsymbol{U} = \boldsymbol{U} \tag{5.2}$$

where ω is the angular frequency and $\boldsymbol{U} = [u_1, u_2, u_3, u_4, u_5, u_6]^T$ is the displacement vector constituted from the nodal displacement for each particle within the unit cell. Figure 5.1(b) shows the dispersion curves of the unit cell with different arrangements of K_{in} and K_{out}. The black lines represent the case for $K_{in} = K_{out} = K_0 = 1$, where a four-band degeneracy can be observed at Γ point ($\vec{k} = (k_x, k_y) = (0,0)$). When K_{in} and K_{out} are different, the degeneracy will be lifted and a band gap appears. To ensure that the band gap is formed near the original double Dirac point, we set the intracell and intercell spring stiffness as $K_{in} = K_0(1-0.5\Delta)$ and $K_{out} = K_0(1+\Delta)$. Here, Δ represents the perturbation of the spring stiffness, and it should be noted that the levels of perturbation are different between K_{in} and K_{out} to ensure the band gap is formed near the original Dirac frequency. By varying the relative stiffness of intercell and intracell springs, the system can be switched between a trivial insulator and a QSH insulator. The red dotted lines in Fig. 5.1(b) stand

for a case for $K_{in} = 0.9 < K_{out} = 1.2$ with a band gap being formed near the original double Dirac point.

To characterize its topological property, we can calculate a topological invariant associated with the system, such as, the spin Chen number C_s. One way to determine the spin Chern number is through the analytical approach, where we need to derive the effective Hamiltonian of the system and map it to the Bernevig-Hughes-Zhang (BHZ) model [24, 148] of QSH effect in an electron system. By transforming the dynamical matrix $\boldsymbol{D}$ to a pseudospin vector basis $\begin{bmatrix} p_+, & d_+, & p_-, & d_- \end{bmatrix}$, we can obtain the effective Hamiltonian of the system, given as:

$$\begin{aligned} \boldsymbol{H} &= Q^{\dagger}[p_x, d_{xy}, p_y, d_{x^2-y^2}]^{\dagger}\boldsymbol{D}[p_x, d_{xy}, p_y, d_{x^2-y^2}]Q \\ &= [p_+, d_+, p_-, d_-]^{\dagger}\boldsymbol{D}[p_+, d_+, p_-, d_-] \\ &= {T_{s2n}}^{\dagger}\boldsymbol{D}T_{s2n} \end{aligned} \tag{5.3}$$

where $\begin{bmatrix} p_x, & d_{xy}, & p_y, & d_{x^2-y^2} \end{bmatrix} = \begin{pmatrix} \frac{\sqrt{3}}{3} & \frac{\sqrt{3}}{6} & -\frac{\sqrt{3}}{6} & -\frac{\sqrt{3}}{3} & -\frac{\sqrt{3}}{6} & \frac{\sqrt{3}}{6} \\ 0 & -\frac{1}{2} & \frac{1}{2} & 0 & -\frac{1}{2} & \frac{1}{2} \\ 0 & -\frac{1}{2} & -\frac{1}{2} & 0 & \frac{1}{2} & \frac{1}{2} \\ -\frac{\sqrt{3}}{3} & \frac{\sqrt{3}}{6} & \frac{\sqrt{3}}{6} & -\frac{\sqrt{3}}{3} & \frac{\sqrt{3}}{6} & \frac{\sqrt{3}}{6} \end{pmatrix}^T$ represent the electronic orbital-like p/d type degenerate modes at the Γ point, $Q = \begin{pmatrix} \frac{1}{\sqrt{2}} & 0 & \frac{1}{\sqrt{2}} & 0 \\ 0 & \frac{1}{\sqrt{2}} & 0 & \frac{1}{\sqrt{2}} \\ \frac{i}{\sqrt{2}} & 0 & \frac{-i}{\sqrt{2}} & 0 \\ 0 & \frac{i}{\sqrt{2}} & 0 & \frac{-i}{\sqrt{2}} \end{pmatrix}$ is the unitary transformation operator, and $T_{s2n} = \begin{bmatrix} p_+, & d_+, & p_-, & d_- \end{bmatrix}$ is the transformation matrix from natural basis to spin vector basis, which is constituted by the pseudospin up $(+)$ and down$(-)$ states. Specifically, $p_{\pm} = \frac{1}{\sqrt{2}}(p_x \pm ip_y)$ and $d_{\pm} = \frac{1}{\sqrt{2}}(d_{xy} \pm id_{x^2-y^2})$.

Then we need to expand the effective Hamiltonian $\boldsymbol{H}$ near Γ point to the first order and get:

$$\boldsymbol{H}(\delta\vec{k}) = \begin{bmatrix} \boldsymbol{H}_+(\delta\vec{k}) & 0 \\ 0 & \boldsymbol{H}_-(\delta\vec{k}) \end{bmatrix} \tag{5.4}$$

with

$$\boldsymbol{H}_{\pm}(\delta\vec{k}) = \begin{bmatrix} K_d - (K_{in} - K_{out}) + \frac{1}{2}a^2\delta k^2 & \frac{1}{2}aK_{out}(\mp\delta k_x - i\delta k_y) \\ \frac{1}{2}K_{out}(\mp\delta k_x + i\delta k_y & K_d + (K_{in} - K_{out}) - \frac{1}{2}a^2K_{out}\delta k^2 \end{bmatrix} \tag{5.5}$$

where $\vec{k} = (\delta k_x, \delta k_y)$ is a small wave vector deviating from the Γ point, $\delta k^2 = {\delta k_x}^2 + {\delta k_y}^2$, and $\boldsymbol{H}_{\pm}(\delta\vec{k})$ represents the Hamiltonian for the pseudospin-up/down state. Note that, $\boldsymbol{H}(\delta\vec{k})$ resembles the BHZ Hamiltonian of HgTe quantum wells [24].

The other way to obtain the spin Chern number is to numerically integrate the Berry curvature of band dispersion of the projected effective Hamiltonian $\boldsymbol{H}_{\pm}(\delta\vec{k})$ over the first Brillouin zone. Figure 5.1(c) depicts the Berry curvature (Ω) of the lower spin-down channel for $K_{in} < K_{out}$. By integrating the Berry curvature over the first Brillouin zone, we can obtain the corresponding spin Chern number given as $C_s^{-\downarrow} = \frac{1}{2\pi}\int_{BZ}\Omega \mathrm{d}^2k$. See subsection 5.7.1 for the Berry curvatures and spin Chern numbers of all spin channels. Following these methods, we can find that the system is a trivial insulator ($C_s = 0$) for $K_{in} > K_{out}$ or a nontrivial QSH insulator ($C_s = 1$) for $K_{in} < K_{out}$. By combining these two kinds of topologically distinct phases, we can realize spin-dependent edge states along the domain wall. Here, the spin Chern number provides an elegant way to characterize the topological property in the proposed periodic system.

5.3 Spin Bott index in Mechanical systems

In the presence of disorder, the translational symmetry of the structure is broken. The two aforementioned classic methods to calculate the spin Chern number in the periodic system are not applicable anymore. Therefore, we need to use a new topological invariant to classify the topological phases in disordered QSH systems. Here, we adopt the spin Bott index proposed by Huang *et al.* [149, 150] in electronic systems and generalize it to a mechanical setup. In this work, we focus mainly on spring stiffness disorder. Note that our spring-mass model can be treated as a special phononic 2D Su-Schrieffer-Heeger (SSH) model in the study of the disorder [151]. Specifically, the disorder in the spring stiffness simultaneously perturbs the hopping strength and on-site potential in the SSH model. We impose a global random stiffness disorder in the system, given as:

$$k_j = K_j + K_0 W_j \varepsilon_j \quad \text{for } j = 1, 2, ..., N \tag{5.6}$$

where N is the total number of springs, ε_j is a random number ranging from -1 to 1, K_j is the unperturbed spring stiffness and may take the values K_{in} or K_{out} depending on its location, $W_j = W\xi_j$ is the corresponding disorder magnitude with W being the disorder strength, and ξ_j is a coefficient that controls the ratio between the disorder strength on intracell and intercell springs.

To calculate the spin Bott index, we consider a finite size structure containing $N = N_1 \times N_2$ unit cells and impose fixed boundary conditions on all four boundaries as shown in Fig. 5.1(d). The dynamical matrix of the finite size structure is noted as $\mathbb{D}$. Throughout our study on discrete models, we set $N_1 = N_2 = 20$. First, we need to derive the effective Hamiltonian $\mathbb{H}$ of this finite size structure. See subsection 5.7.2 for more details about the construction of $\mathbb{D}$ and $\mathbb{H}$.

Then, we can construct a projector operator of the occupied states of the effective Hamiltonian $\mathbb{H}$ below the band gap,

$$P = \sum_{i}^{N_{occ}} |\varphi_i\rangle\langle\varphi_i|, \tag{5.7}$$

where $N_{occ} = 2N$, φ_i is the ith normalized eigenvector of the effective Hamiltonian $\mathbb{H}$ corresponding to eigenvalue ω_i^2. Figure 5.1(e) shows the eigenfrequencies of the finite size clean structure (without disorder $W = 0$) made of the unit cell defined in Fig. 5.1(a) with $K_{in} = 0.9 < K_{out} = 1.2$. The shaded region represents the band gap predicted by the unit cell band structure. Please find the eigenfrequencies and eigenmodes of the finite size structure with different types of unit cells in subsection 5.7.3.

Next, we need to decompose P into two spin sectors by using a spin operator $\widehat{S_z}$

$$P_z = P\widehat{S_z}P, \tag{5.8}$$

where $\widehat{S_z} = S_z \bigotimes I_N$, and $S_z = \begin{bmatrix} 1 & 0 & 0 & 0 \\ 0 & 1 & 0 & 0 \\ 0 & 0 & -1 & 0 \\ 0 & 0 & 0 & -1 \end{bmatrix}$. Figure 5.1(f) shows the eigenvalues of P_z. One can see nonzero eigenvalues of P_z are generally divided into two groups ($|\pm\phi_i\rangle = \pm\frac{1}{2}$) corresponding to the spin up and spin down sectors, respectively. We can write the associated eigenvalue problem as:

$$P_z|\pm\phi_i\rangle = S_\pm|\pm\phi_i\rangle. \tag{5.9}$$

Accordingly, the new spin up/down $(+/-)$ projector operator can be expressed as:

$$P_{\pm}| = \sum_{i}^{N_{occ}/2} |\pm\phi_i\rangle\langle\pm\phi_i|. \tag{5.10}$$

After rescaling the coordinate of the centroid of each unit cell into the interval $[0,1)$, one can derive the projected position operators as:

$$U_{\pm}| = P_{\pm}e^{i2\pi X}P_{\pm} + (I - P_{\pm}), \tag{5.11}$$

$$V_{\pm}| = P_{\pm}e^{i2\pi Y}P_{\pm} + (I - P_{\pm}), \tag{5.12}$$

Finally, we can calculate the Bott index of the two spin sectors. The spin Bott index is given as [149, 150]:

$$B_{\pm} = \frac{1}{2\pi} Im\{tr[log(V_{\pm}U_{\pm}V_{\pm}^{\dagger}U_{\pm}^{\dagger})]\}, \tag{5.13}$$

$$B_s = \frac{1}{2}(B_+ - B_-). \tag{5.14}$$

Note that the spin Bott index is equivalent to the spin Chern number and can be applied to disordered systems to determine the topological QSH phases. With such a powerful tool, we can start to explore topological transitions in the disordered 2D mechanical lattice.

5.4 Disorder induced topological transition in discrete mechanical lattice

To demonstrate the disorder induced topological transition, we take the structure shown in Fig. 5.1(d) with 20 unit cells in both lattice vector directions. The finite structure contains 2400 particles thus 2400 degrees of freedom in total. In this study, we propose a special type of disorder, a ***discrete disorder***, and explore its effects on topology in both topologically trivial and nontrivial 2D mechanical lattice systems. Specifically, the discrete disorder is determined by the choice of random parameter ε_j in Eq. 5.6. Here ε_j is drawn from the discrete uniform distribution on the interval $[-1,1]$ and can only take values -1, 0, or 1. Following the ratio of perturbation in defining K_{in} and K_{out}, we set $\xi_{in} = 0.5$ and $\xi_{out} = 1$. We choose $K_0 = 1$ and $\Delta = \mp 0.2$ to define our clean systems (no disorder) as the base reference. Based on our previous analysis of the periodic discrete model in section 5.2,

we know that when $\Delta = -0.2$, the system is topologically trivial with $K_{in} = 1.1 > K_{out} = 0.8$. For $\Delta = 0.2$, the system becomes topologically nontrivial with $K_{in} = 0.9 < K_{out} = 1.2$.

Figure 5.2(a) shows the evolution of the spin Bott index with the increase of disorder strength W. Each data point represents the numerical average of 200 disorder realizations and the error bars indicate the standard deviations. We begin by taking a look at the role of disorder in a trivial system. As shown by the red line in Fig. 5.2(a), the spin Bott index of a trivial system remains zero regardless of the disorder strength. That is, introducing random discrete disorder cannot alter topological phases in the trivial mechanical lattice for our choice of ξ_{in} and ξ_{out}. Then, we discuss the phase transition in a topologically nontrivial system under disorder, indicated by the blue line in Fig 5.2(a). For $W = 0$, such a clean system is a QSH insulator with the spin Bott index being 1, which agrees well with our analytical results obtained from the unit cell analysis. After introducing disorders in the system, we can see that the spin Bott index remains constant and barely shows any deviation at the low disorder level. This is clear evidence of the robustness of the topological property which is proven to be immune to weak disorder ($W < 0.4$). By further increasing the disorder strength, we observe a sharp drop of the spin Bott index from 1 which eventually becomes quantized near 0. This indicates that the system is changing from a topologically nontrivial phase to a trivial one.

This topological phase transition is usually accompanied by the closure of a band gap. We take the structure shown in Fig. 5.1(d) to investigate the band gap closing process. To get rid of the influence of boundary modes, we modify the structure by imposing periodic boundary conditions at all four edges. Figure 5.2(b) shows the eigenfrequencies of the 20 by 20 structure with the increase of disorder strength. At each disorder level, we take 200 realizations and plot all the eigenfrequencies overlapping with each other. Blue and red circles are the lower and upper edges of the band gaps for all realizations, which refers to the center two eigenfrequencies (1200^{th} and 1201^{st}) in the spectrum. One can see that the band gap always exists for all the disorder realizations when the disorder is in a weak range $W < 0.4$, which very well explains the initial plateau of spin Bott index under disorder in Fig. 5.2(a).

Upon further increase of disorder, the upper and lower edges of the disordered topological

band gap start to merge with each other. Particularly, during the transition region, we see very large deviations in the disorder-averaged spin Bott index. This is because the system's topological nature becomes very sensitive to small perturbations near the critical point and is highly dependent on specific realization when the band gap is about to close. In summary, we quantitatively demonstrate that the disorder in the QSH system tends to destroy its topological nature. Note that the disorder in our model is determined by two parameters, ξ_j, and ε_j. By varying these two parameters, we can manipulate the topological phase transition process by shifting the critical transition boundary. Please find more details about the effect of disorder parameters in subsection 5.7.4.

5.5 Pseudospin-dependent interface states in disordered QSH system

One of the most important features of the QSH system is the unidirectional propagation of topological edge modes. To validate previous analysis on topological phase transition by tracking the spin Bott index, we proceed to investigate the transient pseudospin-dependent wave transport along a designed interface between a trivial insulator and a disordered QSH TI.

Figure 5.3(a) displays a schematic of a numerical simulation setup, which contains 40×40 unit cells in total and is made of two kinds of unit cells. Specifically, the inner core (indicated by the shaded region) consists of 20×20 topologically nontrivial unit cells (marked as type A in Fig. 5.3(a) for the sake of visualization) with $K_{in} = 0.9$ and $K_{out} = 1.2$. All the surrounding area contains trivial unit cells (type B) with $K_{in} = 1.1$ and $K_{out} = 0.8$. Therefore, a rhombic domain wall is formed between these two topologically distinct substructures. To selectively excite a pseudospin mode, we impose displacement input near the interface according to the pseudospin up state p_+. Specifically, Gaussian-modulated sinusoidal pulses (GMSP) with proper phases are placed at 6 sites within a unit cell as indicated by the red star. Figure 5.3(b) shows snapshots of simulated elastic wave propagation under a pseudospin up excitation with center angular frequency at 1.71 in a clean system. It is clear that the elastic waves travel only along the interface in the clockwise direction and can pass the sharp corners with negligible backscattering.

Then we move on to the disordered QSH systems to investigate their characteristics during the topological phase transitions. As we mentioned in the last section, introducing disorder in the

trivial configuration will not flip the topological phase. We only impose disorder in the inner core region during the following analysis, which is made of topologically nontrivial unit cells [see the shaded area in Fig. 5.3(a)]. Figures 5.3(c)-(f) are the schematics of the inner core under discrete disorder with strength $W = 0.2$, $W = 0.4$, $W = 0.6$, and $W = 0.8$, respectively. Color intensity represents the disorder magnitude of spring stiffness ($W_j \varepsilon_j$).

Figures 5.3(g)-(j) show the snapshots of transient results of the elastic wave fields under a pseudospin up excitation with center frequency at 0.272 Hz for corresponding disorder configuration. Similar to a clean system, the pseudospin waves mainly travel along the interface in the clockwise direction in a system under weak disorder $W = 0.2$ and 0.4. However, as the C_6 symmetry at the interface is further broken by the disorder besides the initial mismatch between the topologically distinct unit cells, we start to observe more backscattering by the spin mixing defects [152, 108, 39] [See bottom panels of Figs. 5.3(g) and (h)]. When the stronger disorder is present, we can barely observe any propagation along the interface. Instead, we find the energy tends to penetrate into the bulk for $W = 0.6$ (Fig. 5.3(i)) and show stronger localization for $W = 0.8$ (Fig. 5.3(j)). This could be explained by the Anderson localization [153]. Based on the characteristic and significance of the propagation of pseudospin waves, we can learn that the inner core can retain its topological nature under weak disorder ($W < 0.4$) and start to lose its topological properties with the increase of disorder strength, which is inconsistent with our previous prediction by spin Bott index.

It is worth mentioning that the spin Bott index of a disordered QSH system in Fig. 5.2(a) is an averaged result of numerous realizations, which actually shows a very large deviation during the transition region. The transient simulation results shown in Fig. 5.3 are based on one particular realization, which does not reflect the statistical property of the topologically disordered QSH systems, particularly during the transition region. Please find the transient results of two more realizations under discrete disorder in subsection 5.7.5 to see the disorder-realization-dependent propagation of pseudospin waves in disordered structures.

5.6 Disordered topological phononic crystal

So far, the interplay between disorder and topology has been explored in the discrete model. To extend our discrete spring-mass model into a continuous structure, we propose a phononic crystal constructed by connecting hexagonal prism cavities with square tubes, as shown in Fig. 5.4(a). Here the gray parts are filled with air with density $\rho = 1.3$ kgm^{-3} and speed of sound $v = 343$ m/s, and the white parts are rigid walls. The prism resonance cavities work effectively as the mass particles in the discrete model and the air channels in square windows are equivalent to the springs. The parameters used are $m = 15$ mm, $n = 1.3$ mm, $H = 25$ mm, and $b = 2$ mm. A top view of the extended unit cell of the phononic crystal and a rough mapping to the discrete spring-mass lattice can be seen in Fig. 5.4(b). By varying the cross-section of the air tubes, we can effectively tune the spring stiffness corresponding to the discrete lattice model. Figure 5.4(c) gives the relationship between the width of the *square* channels (d) and the effective spring stiffness. Red circles represent the results obtained by fitting unit cell dispersion curves of a discrete lattice model with that of the phononic crystal calculated by finite element analysis (FEA) software COMSOL Multiphysics [See subsection 5.7.6 for more details on the fitting process]. The black line stands for the second degree polynomial fitted to the data red dots.

To verify the topological states along the interface between topologically nontrivial disordered QSH insulator and a trivial insulator, we construct a U-shape interface by joining the substructure with two kinds of unit cells. Specifically, type A unit cell is topologically nontrivial with $d_{in} = 4.9$ mm and $d_{out} = 5.4$ mm, which corresponds to $K_{in} = 0.9 \times 10^5$ and $K_{out} = 1.1 \times 10^5$ in the discrete model. Here, d_{in} and d_{out} refer to the width of intracell and intercell air channels, respectively. Type B unit cell is topologically trivial with $d_{in} = 5.2$ mm and $d_{out} = 4.7$ mm, which is equivalent to a unit cell with $K_{in} = 1.1 \times 10^5$ and $K_{out} = 0.8 \times 10^5$ in the discrete model. Figure 5.4(d) is a schematic of the FEA setup. Specifically, the inner core consists of the type A unit cells with intracell air channels narrower than the intercell ones, while the outer part contains trivial unit cells (type B) with intracell air channels wider than the intercell ones. The green lines represent the radiative boundary conditions imposed on four sides of the system, which allows acoustic

waves to leak into the environment to reduce reflection at these boundaries. Six point sources with appropriate phase differences are put in the six air cavities within one unit cell as marked by the red star in Fig. 5.4(d) to excite the system with pseudospin up modes. We then use COMSOL Multiphysics to perform the harmonic finite element analysis. Similar to our arrangement in the transient analysis in section 5.4, the discrete disorder is only introduced on the inner core region. Note that, the disorder configuration is determined by changing the air tube width d based on the spring stiffness information from a disorder realization in the discrete model. See subsection 5.7.7 for a flowchart explaining the process of constructing the disordered phononic structure.

Figure 5.4(e) shows the steady state response of a clean system under pseudospin-up excitation. It is clear that the acoustic waves are very well confined to the topological interface and can only propagate in the clockwise direction. Particularly, the pseudospin waves can robustly pass the sharp bends without obvious reflections and scatterings.

The one-way propagation of pseudospin dependent waves at 2.72 kHz with the weak disorder ($W = 0.2, 0.4$) are shown in Figs. 5.4(f) and (g). Specifically, a disordered QSH system with A type unit cells under disorder level $W = 0.2$ or 0.4 has spin Bott index 1 with very small variations, thus indicating a stable topologically nontrivial state [see Figure 5.2(a)]. In this case, we can observe that the acoustic waves are still mostly localized near the topological boundary, and a significant amount of the energy is still flowing in the clockwise direction. However, instead of an uniform energy distribution along the propagation path as seen in the clean system, we start to see more unevenly distributed modes at the interface with energy penetrating to the bulk of the substructure.

As we further increase the disorder strength to $W = 0.6$, the pseudospin excitation does not generate unidirectional propagating waves [see Fig. 5.4(h)]. Finally, when the disorder strength reaches $W = 0.8$, the inner substructure becomes topological trivial with a spin Bott index very close to zero [see Fig. 5.2(a)]. That is, the interface between the substructures A and B can no longer be treated as a topological domain wall. As presented in Fig. 5.4(i), acoustic energy spreads into the bulk of the structure. Again the results in Figs. 5.4(e)-(i) are based on a single disorder realization, which cannot represent the statistical characteristics of the disordered topological QSH insulator. Steady-state wave fields under pseudospin up excitation for one more realization are

plotted in subsection 5.7.8 for comparison.

5.7 Additional discussion

5.7.1 Berry curvature and Spin Chern number

Figure 5.5 shows the calculated Berry curvature in the first Brillouin zone for all spin channels. By integrating the Berry curvature, we can obtain the corresponding spin Chern numbers of four spin bands, given as $C_S^{\downarrow -} = 1$, $C_S^{\uparrow -} = -1$, $C_S^{\downarrow +} = -1$, and $C_S^{\uparrow +} = 1$. Then the spin Chern numbers of spin up and spin down states are defined as $C_S^{\downarrow} = \frac{C_S^{\downarrow +} - C_S^{\downarrow -}}{2} = -1$ and $C_S^{\uparrow} = \frac{C_S^{\uparrow +} - C_S^{\uparrow -}}{2} = 1$, respectively. Therefore, the total spin Chern number can be calculated as $C_S = \frac{C_S^{\uparrow} - C_S^{\downarrow}}{2}$, indicating a topologically nontrivial system.

5.7.2 Dynamical matrix and effective Hamiltonian of finite size structure

While assembling dynamical matrix $\mathbb{D}$, we need to arrange the nodal displacements such that particle displacements within a unit cell are packed in a subgroup with the increase of particle number as noted by the number in Fig. 5.1(a). Therefore, the modal displacement vector can be written as:

$$\mathbb{U}_{6N\times 1} = \begin{bmatrix} U_1 \\ U_2 \\ \vdots \\ U_{N-1} \\ U_N \end{bmatrix} = \begin{bmatrix} T_{s2n}\psi_1 \\ T_{s2n}\psi_2 \\ \vdots \\ T_{s2n}\psi_{N-1} \\ T_{s2n}\psi_N \end{bmatrix} = \begin{bmatrix} T_{s2n} & 0 & 0 & 0 & 0 \\ 0 & T_{s2n} & 0 & 0 & 0 \\ 0 & 0 & \ddots & 0 & 0 \\ 0 & 0 & 0 & T_{s2n} & 0 \\ 0 & 0 & 0 & 0 & T_{s2n} \end{bmatrix} \begin{bmatrix} \psi_1 \\ \psi_2 \\ \vdots \\ \psi_{N-1} \\ \psi_N \end{bmatrix} = \mathbb{T}_{6N\times 4N}\Psi_{4N\times 1} \tag{5.15}$$

where N is the total number of unit cells, U_j is the modal displacement vector of the jth unit cell, ψ_j is the transformed modal displacement vector corresponding to the jth unit cell in the spin vector basis, $\mathbb{U}$ is the sorted modal displacements of the finite size structure, and $\mathbb{T}$ is the global transformation matrix. Then the effective Hamiltonian of the finite size structure is defined as:

$$\mathbb{H}_{4N\times 4N} = \mathbb{T}^{\dagger}_{4N\times 6N}\mathbb{D}_{6N\times 6N}\mathbb{T}_{6N\times 4N}. \tag{5.16}$$

5.7.3 *Eigenfrequencies and typical eigenmodes of the finite size structures with different types of unit cells*

Figure 5.6(a) compares eigenfrequencies of the finite size structures with different choices of unit cells. The blue circles represent the case for topologically nontrivial unit cells with $K_{in} = 0.9 < K_{out} = 1.2$, which is the same as Fig. 5.1(e). The red circles stand for results of topologically trivial unit cells with $K_{in} = 1.1 > K_{out} = 0.8$. Figures 5.6(b) and (c) give examples of bulk modes with frequencies outside the band gap in a trivial and nontrivial configuration, respectively. While the properties of the bulk modes are similar, the clear differences can be observed in the frequency band gap It is easy to catch that the main difference between these two cases is the emergence of boundary modes within the band gap range in the topologically nontrivial structure. Figures 5.6(d) and (e) show typical examples of an edge state and a corner state, respectively.

5.7.4 *Effect of disorder parameters on the topological phase transitions*

In previous sections of this chapter, we focus on the interplay of discrete disorder with topology. It is controlled by two parameters ξ_j and ε_j. Specifically, ξ_j refers to the disorder ratio between intercell and intracell disorder coefficients (ξ_{in}/ξ_{out}). It explains the fact that intercell and intracell springs may have different tendencies to develop disorders. Figure 5.7(a) compares the disorder averaged spin Bott index for different combinations of ξ_{in} and ξ_{out}. Blue line stands for the results of the case with $\xi_{in} = 0.5$, $\xi_{out} = 1$, which is the same as Figure 5.2(a). Red line plots the results obtained with $\xi_{in} = 1$, $\xi_{out} = 1$. The choice of ε_j determines the disorder type. By randomly selecting *integers* from the discrete uniform distribution on the interval $[-1,1]$, we define the so-called discrete disorder, which is a very simplified case of disorder. A more general type of disorder, namely the continuous disorder, can be realized by setting ε_j a uniformly distributed number in the interval $[-1,1]$. Figure 5.7(b) compares the effects of discrete (blue line) and continuous (yellow line) disorder on topology. By varying disorder parameters, we will be able to manipulate the topological phase transition process and shift the critical transition boundary.

5.7.5 Transient wave analysis for other realizations under discrete disorder

In Fig. 5.2, we can observe that the spin Bott index of a system with a certain disorder level shows a very large deviation, which indicates that topology is highly dependent on a particular disorder configuration for a certain range of disorders. Here, we conduct 2 extra transient simulations for different discrete disorder realizations and demonstrate the snapshots of wave fields at $t = 300$ in Fig. 5.8. We see very similar wave propagation phenomena for weak disorder cases ($W = 0.2$ and $W = 0.4$), corresponding a the stable spin Bott index that is very well quantized at 1. Figures 5.8(c)-(d) show two more numerical simulation results with disorder strength $W = 0.6$ and 0.8, respectively. By comparing the structure responses of different realizations, we find that a larger standard deviation of the spin Bott index suggests that systems with different disorder realizations tend to respond more distinctively under the same pseudospin excitation. Despite the fact such an approximate relationship involves intuitive interpretations of the transient wave fields, it still helps to give a better understanding of the disordered QSH system based on the calculation of the spin Bott index.

5.7.6 Parameter fitting between the square tube width and the effective spring stiffness

In order to find the relationship between the square tube width and the effective spring stiffness, we fit the dispersion diagram of the spring-mass model with that of a phononic crystal obtained from COMSOL Multiphysics. Figures 5.9(a)-(b) show the unit cell of the spring-mass model and the phononic crystal, respectively. A comparison between the dispersion relations obtained from the discrete model and the continuous model is plotted in Fig. 5.9(c). Black lines represent the result of a discrete spring-mass model with $K_{in} = K_{out} = 1.0 \times 10^8$. Red dots stand for the FEA result with $d_{in} = 4.73$ mm, and $d_{out} = 5.75$ mm. Figure 5.9(d) shows a similar results for $K_{in} = 0.9 \times 10^8$, $K_{out} = 1.2 \times 10^8$ and $d_{in} = d_{out} = 5.08$ mm. By varying d_{in} and d_{out} values and repeating the dispersion curves fitting process, we finally come up with the relationship between the square tube width d and the effective spring stiffness K within the range of our interest, as shown in Fig. 5.4(c).

5.7.7 Construction of disordered phononic crystal structure

The disordered phononic structures are constructed by mapping from discrete spring-mass systems. First, we need to generate the random parameter ε_j that determines the disorder configuration, where j is the spring element number. Then we substitute ε_j into Eq. 5.6 to calculate the stiffness of the jth disordered spring. Next, based on the fitted polynomial in Fig. 5.4(c), we find the width d of an air tube corresponding to each spring in the discrete model. Finally, we draw the geometry of disordered phononic crystal for FEA simulation in COMSOL Multiphysics. Figure 5.10 summarizes the procedure to generate the disordered phononic crystal model.

5.7.8 Steady state in phononic crystal for extra discrete disorder realization

In Figure 5.11, we show the steady state of disordered phononic crystal under pseudospin excitation with the same disorder strength but a different configuration compared to realization in Figure 5.4. As we can see, with the increase of disorder strength, less energy could stay confined near the interface and propagate in the clockwise direction. We observe a growing leakage into the bulk and more significant energy localization. In general, by comparing the results in Fig. 5.4 and Fig. 5.11, we can know that wave propagates in a very similar trend for disordered systems with spin Bott index of low deviation ($W = 0.2$, 0.4, and 0.8). When the averaged spin Bott index has a large variation ($W = 0.6$), a more drastic difference may appear in the disordered system.

5.8 Conclusion

This chapter investigates the interplay between topology and disorder in both discrete and continuous 2D phononic systems. Quantitative analysis of the disorder effect is conducted by tracking the spin Bott index. We find that a topologically nontrivial QSH system can endure a certain level of disorder and will eventually alter its topological nature under strong disorder. Transient simulation results of the pseudospin dependent waves also confirm the topological phase transition induced solely by disorder and agreed well with the spin Bott index prediction. With the proposed framework, we provide a powerful tool to quantitatively analyze the topological phases in a disordered

2D system. The results reveal the robustness of the zone-folding induced topological phases and may inspire future explorations on the sensitivity of the topologically nontrivial system to different types of disorders.

While this study focused on the linear response of the 2D system, we envision that the findings of this study can be useful for the exploration of the nonlinear response of the 2D disordered topological system. Likewise, the extension of the spin Bott index to different types of systems (e.g., quasi-periodic 2D system or general 3D architecture) can be one of directions for the future studies. Lastly, the findings of this study may lay a foundation for the possible realization of TAI in the 2D/3D mechanical system.

5.9 Author contributions

X. Shi and J. Yang conceived the idea of the project. X. Shi performed the numerical simulations. X. Shi wrote the manuscript. H. Huang, R. Zhu, and J. Yang supervised the project. All authors interpreted the results and reviewed the manuscript.

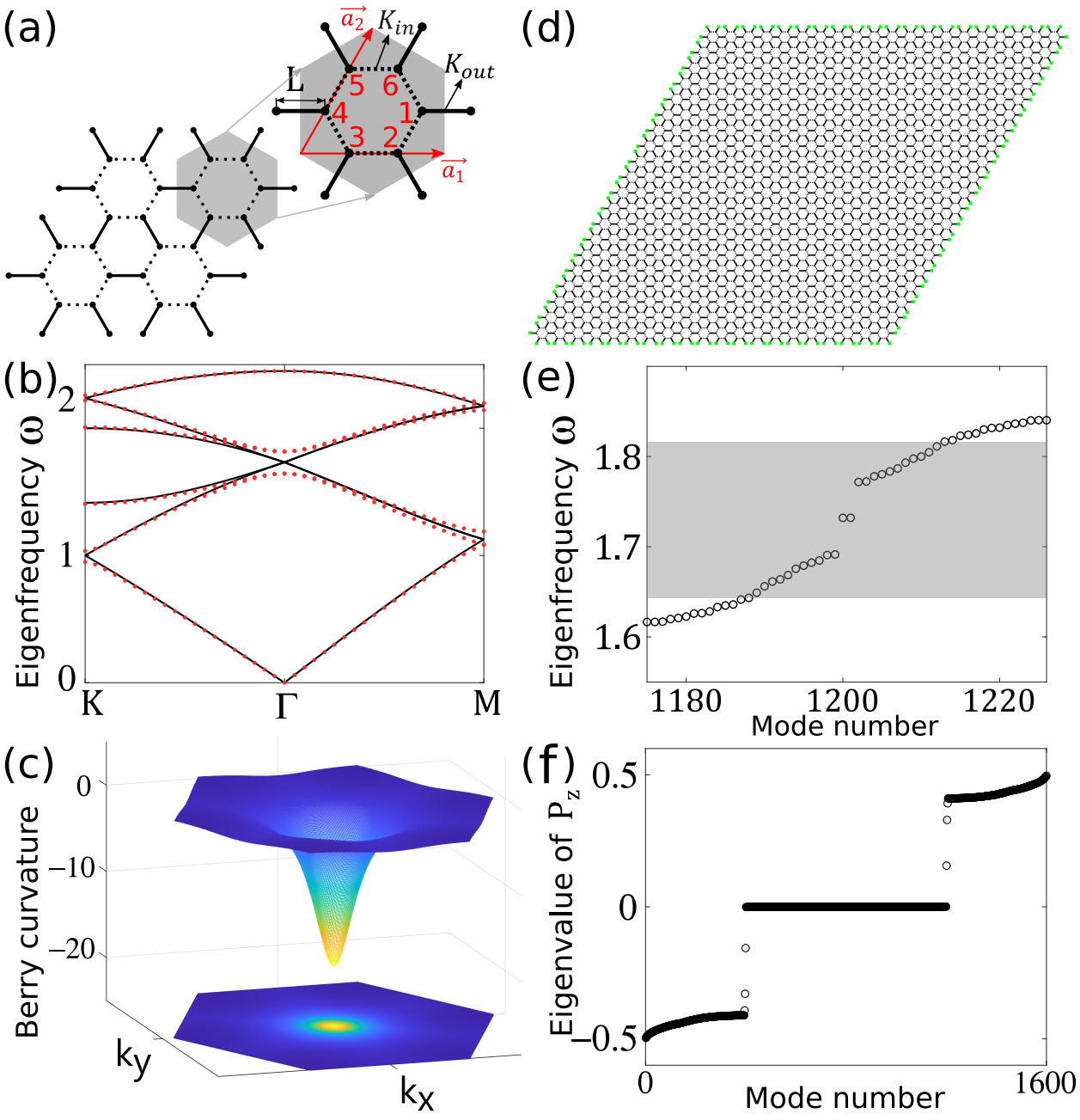

Figure 5.1: (a) A schematic of the unit cell of a spring-mass-based discrete structure. (b) Band structure of the expanded unit cell. (c) Berry curvature of the lower band of the spin-up channel. (d) Configuration of a finite size lattice structure with fixed boundary conditions. Green dots stand for the mass particles whose displacements are set to zero. (e) Eigenfrequencies of the finite size structure. (f) Eigenvalues of the spin projector operator P_z.

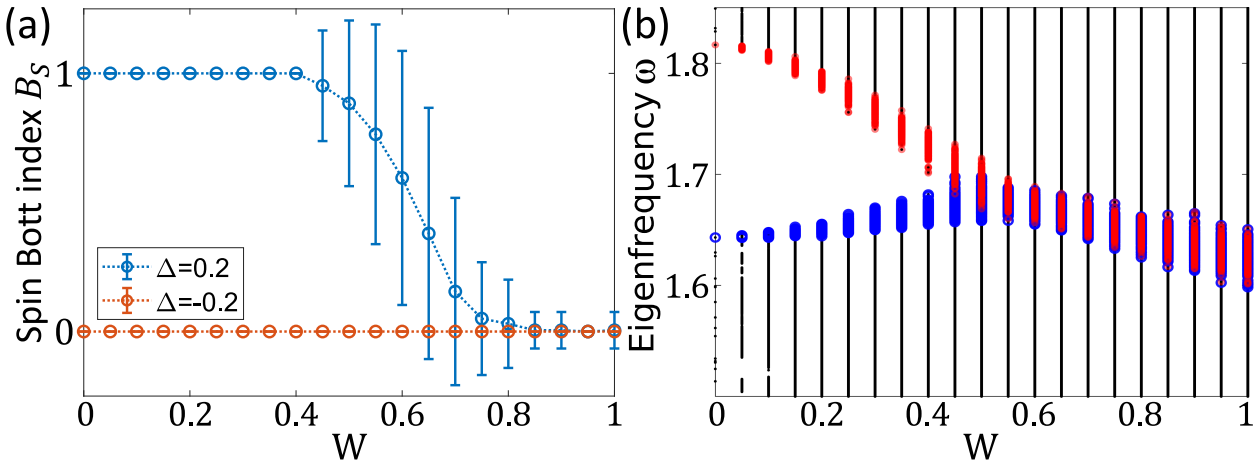

Figure 5.2: (a) Dependence of spin Bott index B_S on the disorder strength under random discrete disorder. (b) Eigenfrequencies of a topologically nontrivial structure with periodic boundary conditions under different levels of disorder.

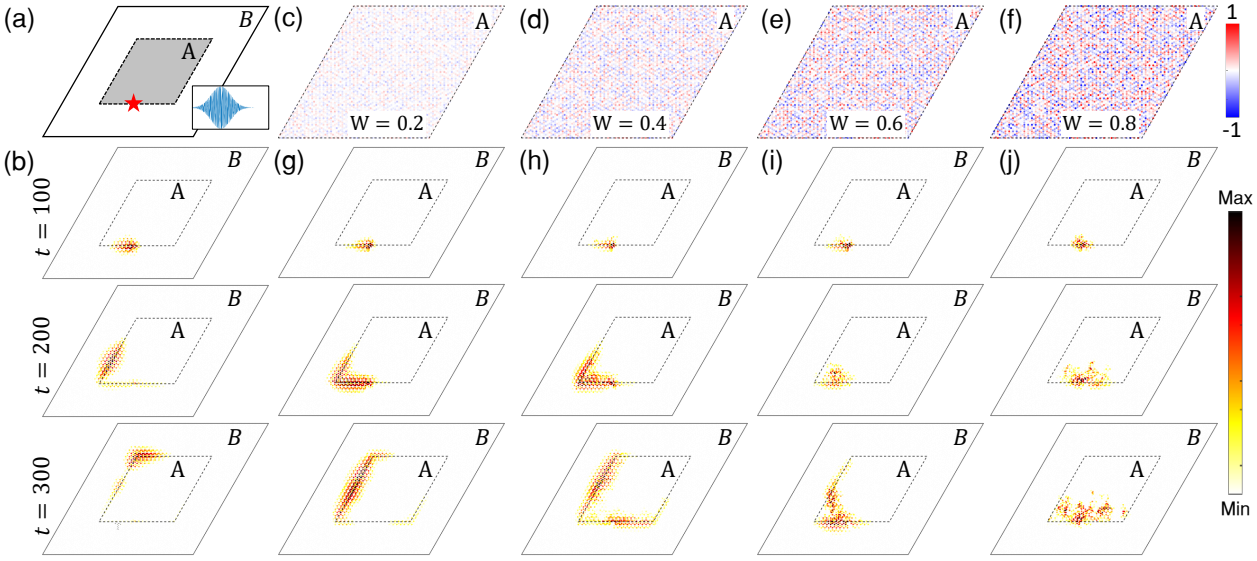

Figure 5.3: (a) Numerical setup of the rhombic structure. The interface between two kinds of topologically distinct lattices is indicated by the black dashed line. (b) Transportation of the pseudospin-dependent wave package along the interface at a different time in a clean system. Color intensity represents the power spectral density of the particle displacements. (c)-(f) Schematics of the disordered inner core under random discrete disorder with strength $W = 0.2$, $W = 0.4$, $W = 0.6$, and $W = 0.8$ respectively. (g)-(j) Snapshots of transient simulated results under pseudospin excitation in the corresponding disordered structures. Colorbar represents the magnitude of the nondimensionalized displacement given as $20\log\frac{u_j}{A_0}$, where u_j is the particle displacement and A_0 is the amplitude of the displacement input.

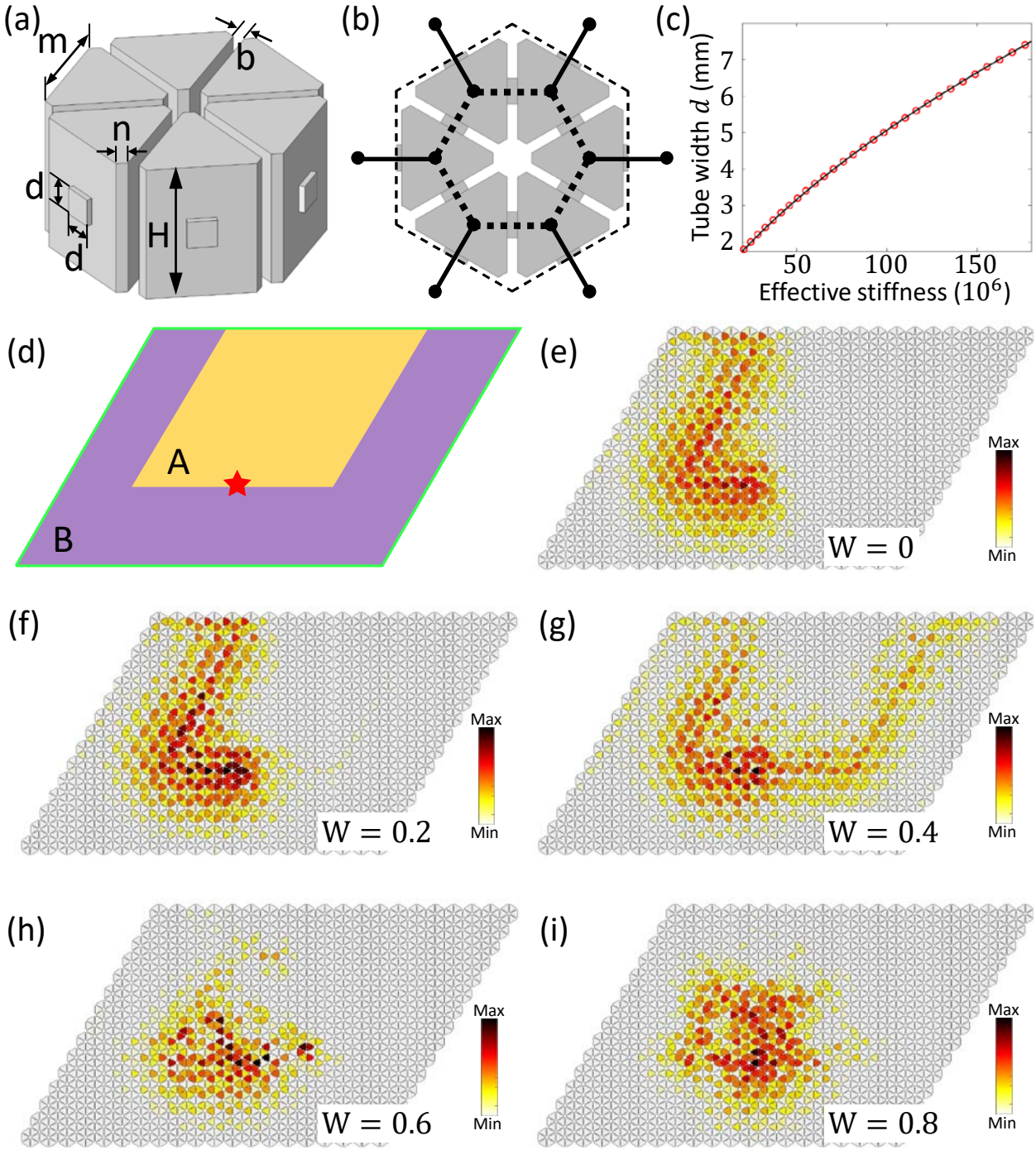

Figure 5.4: (a) A detailed view of the design of the phononic crystal. (b) A top view of the unit cell and a mapping relation to the discrete model. (c) Relationship between the width d of air tubes and the effective spring stiffness. (d) Schematic of the Finite element simulation setup. A U-shape interface is created by putting substructures with two types of unit cells adjacently. The red star indicates the excitation point. (e)-(i) Simulated wave field with a harmonic excitation along the interface under discrete disorder with disorder strength $W = 0$, 0.2, 0.4,0.6, and 0.8, respectively.

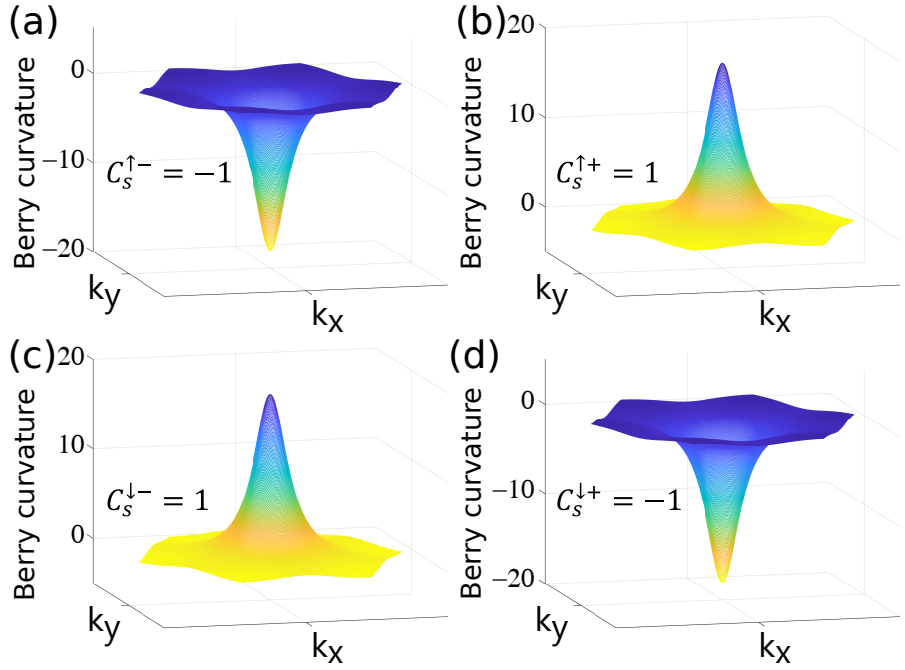

Figure 5.5: Berry curvature and spin Chern number of four pseudo spin channels for $K_{in} < K_{out}$. (a) The lower band of pseudo spin up. (b) The upper band of pseudo spin up. (c) The lower band of pseudo spin down. (d) The upper band of pseudo spin down.

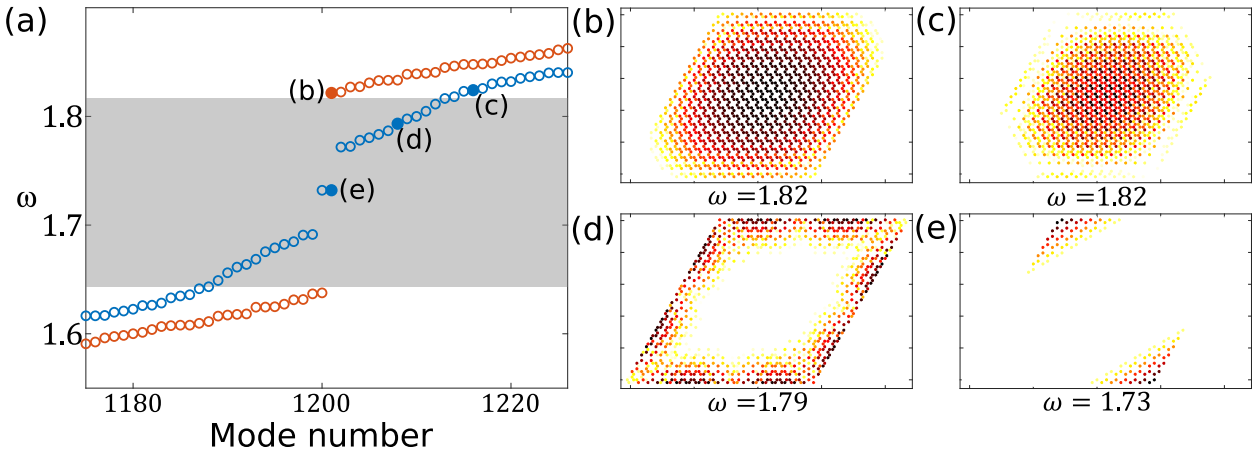

Figure 5.6: (a) Eigenfrequency spectrum of the topologically trivial (red circles) or nontrivial (blue circles) structure. (b)-(e) Eigenmodes of the finite structure corresponding to the markers in (a).

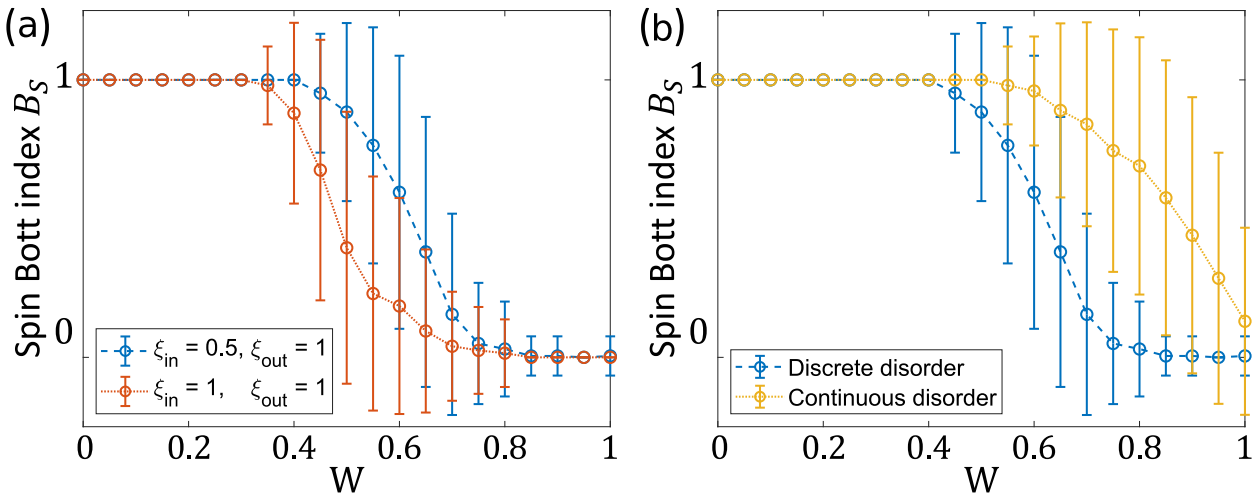

Figure 5.7: Effect of (a) disorder ratio and (b) disorder type on the topological phase transition.

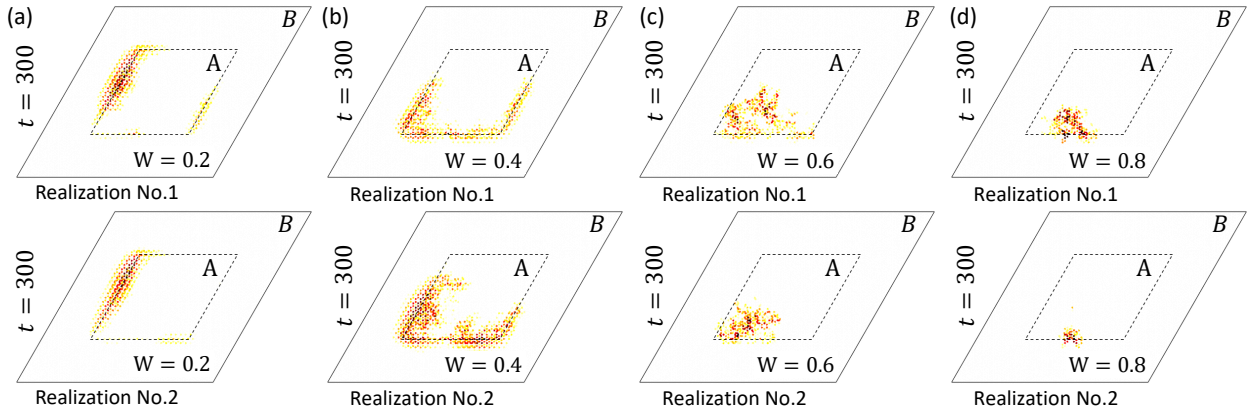

Figure 5.8: (a)-(d) Transient simulated wave fields at $t = 300$ under pseudospin excitation for two more realizations under random discrete disorder with disorder strength $W = 0.2$, $W = 0.4$, $W = 0.6$, and $W = 0.8$, respectively.

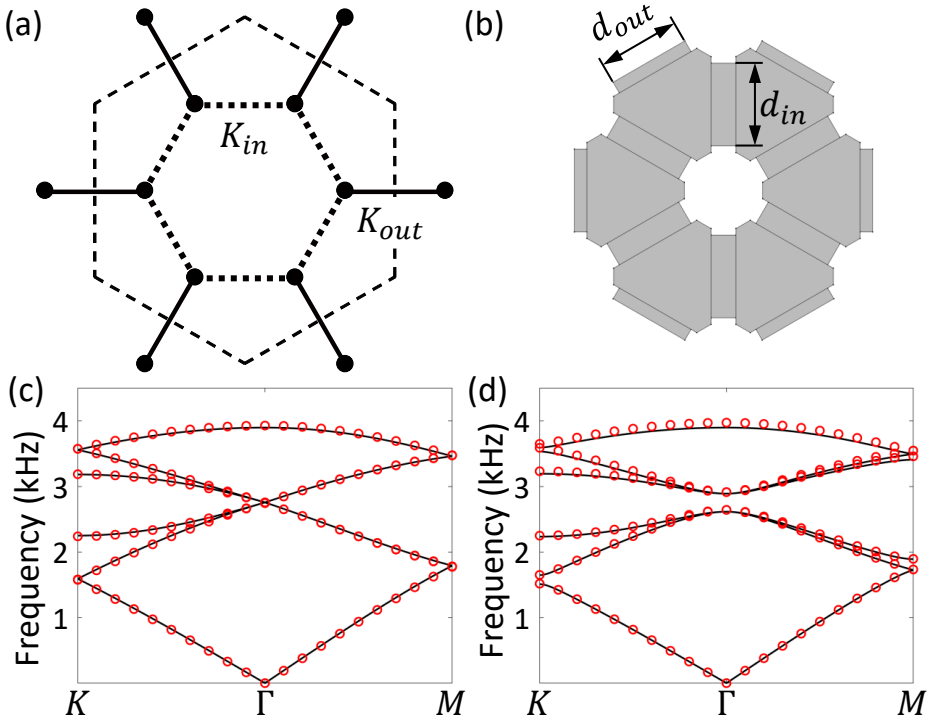

Figure 5.9: (a) Unit cell of the discrete model (b) Top view of the unit cell of a phononic crystal. (c)-(d) Comparison of unit-cell dispersion curves with a double Dirac point or a band gap obtained from the spring-mass model (solid lines) and the phononic crystal (red dots)

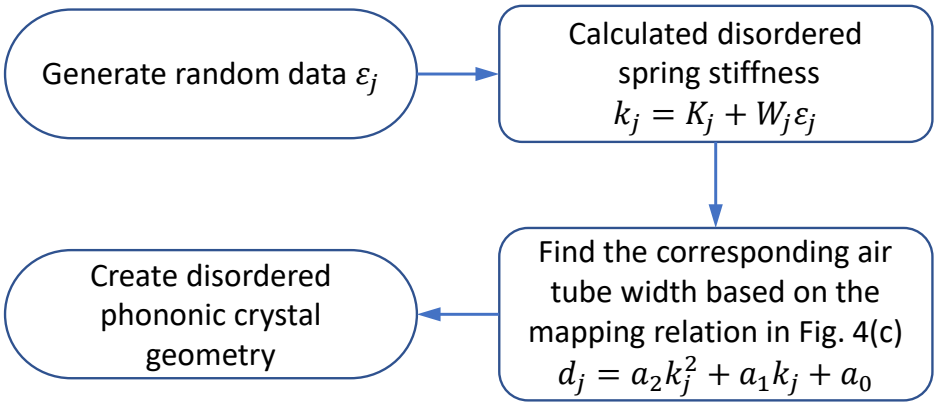

Figure 5.10: Procedure to generate the disordered phononic crystal.

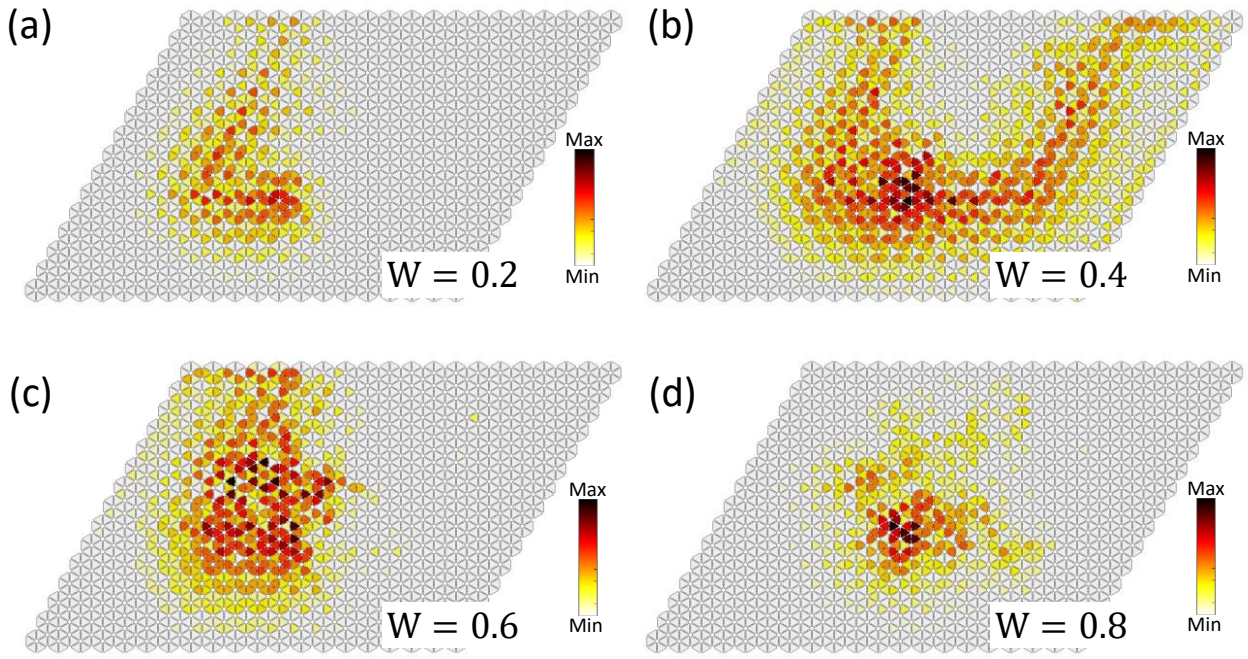

Figure 5.11: (a)-(d) Steady state wave field under a harmonic excitation in the presence of discrete disorder with disorder strength $W = 0.2$, 0.4, 0.6, and 0.8, respectively.

Chapter 6

CONCLUSIONS AND OUTLOOK

This dissertation has focused on explorations of topological mechanical metamaterials. We mainly investigate topological phases in two classes of mechanical metamaterials: (i) ordered 3D mechanical metamaterials and (ii) disordered mechanical metamaterials. The results presented clearly demonstrate that mechanical metamaterials can be simple, versatile, and fruitful platforms to realize topological effects, which is of great both conceptual and practical importance. Here, we summarize the key findings of our research:

- We show topological protected waves on the surfaces in 3D mechanical structures (Chapter 2 and 3). We design a 3D mechanical structure in analogy to Weyl semimetals in condensed matter physics and numerically show the robust one-way transport of elastic energy which is immune to the sharp corners and defects in full-scale simulations. We also proposed a 3D chiral phononic crystal that carries spin-1 Weyl points with topological charge ± 2 and presents the collimated robust propagation of topological surface arc states in the system.

- We propose a 3D Chiral Lieb lattice by stacking up the 2D subsystems (Chapter 3). By introducing chiral interlayer interactions, we induce synthetic gauge flux at certain $k_x - k_y$ planes in the reciprocal space and observe spin-1 Weyl points that carry topological charge ± 2. Such a tight-binding model is implemented in 3D acoustic systems and may inspire research in other fields.

- We introduce new topological invariants based on only real-space wave functions to probe the topological property of **disordered** mechanical systems (Chapters 4 and 5). We generalize the local topological marker ν, mean chiral displacement $C(t)$, and infinite-time limit

of mean chiral displacement C_∞ into a 1D mechanical chain and spin Bott index B_s into 2D mechanical structures to characterize the topological nature in the absence of translational symmetry. Such powerful tools lay a foundation to investigate the effect of disorder on topological mechanical metamaterials.

- We demonstrate the disorder-induced topological phase transitions in both 1D and 2D mechanical metamaterials by tracking the evolution of a topological invariant with the increase of disorder strength (Chapters 4 and 5). By gradually introducing global random disorder, we can destroy the topological phases in mechanical systems, such as the localized boundary states in the 1D dimmer spring-mass chain and the unidirectional interface states at the domain wall between the trivial insulator and disordered QSH mechanical insulator. Moreover, we realize a mechanical analogy to the topological Anderson insulator in a 1D spring-mass model, which is accomplished by introducing chiral symmetry preserved disorder in a trivial system.

Overall, this research expands the study of topological mechanical metamaterials into three dimensions and disordered regions. Our new findings can help to deepen our understanding of topological phases in mechanical systems and may inspire research in other classical wave fields. At the end of this dissertation, we would like to address several potential directions for future research:

- A natural extension of this research would be an investigation of disorder-induced topological phase transitions in 3D mechanical systems. In particular, the realization of a 3D mechanical topological Anderson insulator is still missing. The main challenge is how to calculate a topological invariant or define an empirical parameter to characterize topological properties in 3D disordered mechanical systems.

- Nonlinear topological mechanical insulators are less explored. Besides disorder, nonlinearity is another key factor that may suppress the traditional band theory. Therefore, it is very

important to understand the impact of nonlinearity on topological phases. The early explorations on nonlinear topological mechanical systems have revealed that nonlinearity can not only harm but induce topological states in different cases [154, 155, 156, 157, 158, 159]. However, the fundamental theory of nonlinear topological invariants has not been established.

- Most of the previous topological mechanical metamaterials are consisted of periodic building blocks. It is worth exploring aperiodic topological mechanical systems. Topological phases in 1D and 2D quasiperiodic mechanical structures have been theoretically and experimentally verified in numerous researches [160, 161, 162, 163, 164, 165, 166, 167, 168, 169, 170]. However, topological wave phenomenons in 2D quasiperiodic mechanical systems with Penrose tiling pattern, Ammann-Beenker tiling pattern, and other classical patterns of rotation symmetries, [171] are yet to be explored.

BIBLIOGRAPHY

[1] Viktor G Veselago. The Electrodynamics of Substances with Simultaneously Negative Values of ϵ and μ. *Sov. Phys. Usp.*, 10(4):509–514, April 1968.

[2] D. R. Smith, Willie J. Padilla, D. C. Vier, S. C. Nemat-Nasser, and S. Schultz. Composite Medium with Simultaneously Negative Permeability and Permittivity. *Phys. Rev. Lett.*, 84(18):4184–4187, May 2000.

[3] Vladimir M. Shalaev, Wenshan Cai, Uday K. Chettiar, Hsiao-Kuan Yuan, Andrey K. Sarychev, Vladimir P. Drachev, and Alexander V. Kildishev. Negative index of refraction in optical metamaterials. *Opt. Lett., OL*, 30(24):3356–3358, December 2005.

[4] Zhengyou Liu, Xixiang Zhang, Yiwei Mao, Y. Y. Zhu, Zhiyu Yang, C. T. Chan, and Ping Sheng. Locally Resonant Sonic Materials. *Science*, 289(5485):1734–1736, September 2000.

[5] Xiaoming Zhou and Gengkai Hu. Analytic model of elastic metamaterials with local resonances. *Phys. Rev. B*, 79(19):195109, May 2009.

[6] Joseph N. Grima, Ruben Gatt, Naveen Ravirala, Andrew Alderson, and K. E. Evans. Negative Poisson's ratios in cellular foam materials. *Materials Science and Engineering: A*, 423(1):214–218, May 2006.

[7] Nicholas Fang, Dongjuan Xi, Jianyi Xu, Muralidhar Ambati, Werayut Srituravanich, Cheng Sun, and Xiang Zhang. Ultrasonic metamaterials with negative modulus. *Nature Mater*, 5(6):452–456, June 2006.

[8] Z. Yang, Jun Mei, Min Yang, N. H. Chan, and Ping Sheng. Membrane-Type Acoustic Metamaterial with Negative Dynamic Mass. *Phys. Rev. Lett.*, 101(20):204301, November 2008.

[9] Zachary G. Nicolaou and Adilson E. Motter. Mechanical metamaterials with negative compressibility transitions. *Nature Mater*, 11(7):608–613, July 2012.

[10] Víctor Espinosa, Víctor J. Sánchez-Morcillo, Kestutis Staliunas, Isabel Pérez-Arjona, and Javier Redondo. Subdiffractive propagation of ultrasound in sonic crystals. *Phys. Rev. B*, 76(14):140302, October 2007.

[11] M. Kafesaki, M. M. Sigalas, and N. García. Frequency Modulation in the Transmittivity of Wave Guides in Elastic-Wave Band-Gap Materials. *Phys. Rev. Lett.*, 85(19):4044–4047, November 2000.

[12] D. Richards and D. J. Pines. Passive reduction of gear mesh vibration using a periodic drive shaft. *Journal of Sound and Vibration*, 264(2):317–342, July 2003.

[13] R. Zhu, X. N. Liu, G. K. Hu, C. T. Sun, and G. L. Huang. A chiral elastic metamaterial beam for broadband vibration suppression. *Journal of Sound and Vibration*, 333(10):2759–2773, May 2014.

[14] Steven A. Cummer and David Schurig. One path to acoustic cloaking. *New J. Phys.*, 9(3):45, March 2007.

[15] Mohamed Farhat, Sebastien Guenneau, and Stefan Enoch. Ultrabroadband Elastic Cloaking in Thin Plates. *Phys. Rev. Lett.*, 103(2):024301, July 2009.

[16] Junfei Li, Xiaoming Zhou, Guoliang Huang, and Gengkai Hu. Acoustic metamaterials capable of both sound insulation and energy harvesting. *Smart Mater. Struct.*, 25(4):045013, March 2016.

[17] Stefano Gonella, Albert C. To, and Wing Kam Liu. Interplay between phononic bandgaps and piezoelectric microstructures for energy harvesting. *Journal of the Mechanics and Physics of Solids*, 57(3):621–633, March 2009.

[18] Guancong Ma, Meng Xiao, and C. T. Chan. Topological phases in acoustic and mechanical systems. *Nat Rev Phys*, 1(4):281–294, April 2019.

[19] K. v. Klitzing, G. Dorda, and M. Pepper. New Method for High-Accuracy Determination of the Fine-Structure Constant Based on Quantized Hall Resistance. *Phys. Rev. Lett.*, 45(6):494–497, August 1980.

[20] Emil Prodan and Hermann Schulz-Baldes. *Bulk and Boundary Invariants for Complex Topological Insulators: From K-Theory to Physics*. Mathematical Physics Studies. Springer, Cham, 2016.

[21] Yuanbo Zhang, Yan-Wen Tan, Horst L. Stormer, and Philip Kim. Experimental observation of the quantum Hall effect and Berry's phase in graphene. *Nature*, 438(7065):201–204, November 2005.

[22] K. S. Novoselov, Z. Jiang, Y. Zhang, S. V. Morozov, H. L. Stormer, U. Zeitler, J. C. Maan, G. S. Boebinger, P. Kim, and A. K. Geim. Room-Temperature Quantum Hall Effect in Graphene. *Science*, 315(5817):1379–1379, March 2007.

[23] C. L. Kane and E. J. Mele. Quantum Spin Hall Effect in Graphene. *Phys. Rev. Lett.*, 95(22):226801, November 2005.

[24] B. Andrei Bernevig, Taylor L. Hughes, and Shou-Cheng Zhang. Quantum Spin Hall Effect and Topological Phase Transition in HgTe Quantum Wells. *Science*, 314(5806):1757–1761, December 2006.

[25] D. N. Sheng, Z. Y. Weng, L. Sheng, and F. D. M. Haldane. Quantum Spin-Hall Effect and Topologically Invariant Chern Numbers. *Phys. Rev. Lett.*, 97(3):036808, July 2006.

[26] F. D. M. Haldane. Model for a Quantum Hall Effect without Landau Levels: Condensed-Matter Realization of the "Parity Anomaly". *Phys. Rev. Lett.*, 61(18):2015–2018, October 1988.

[27] Xiao-Liang Qi, Yong-Shi Wu, and Shou-Cheng Zhang. Topological quantization of the spin Hall effect in two-dimensional paramagnetic semiconductors. *Phys. Rev. B*, 74(8):085308, August 2006.

[28] Cui-Zu Chang, Jinsong Zhang, Xiao Feng, Jie Shen, Zuocheng Zhang, Minghua Guo, Kang Li, Yunbo Ou, Pang Wei, Li-Li Wang, Zhong-Qing Ji, Yang Feng, Shuaihua Ji, Xi Chen, Jinfeng Jia, Xi Dai, Zhong Fang, Shou-Cheng Zhang, Ke He, Yayu Wang, Li Lu, Xu-Cun Ma, and Qi-Kun Xue. Experimental Observation of the Quantum Anomalous Hall Effect in a Magnetic Topological Insulator. *Science*, 340(6129):167–170, April 2013.

[29] Long Ju, Zhiwen Shi, Nityan Nair, Yinchuan Lv, Chenhao Jin, Jairo Velasco, Claudia Ojeda-Aristizabal, Hans A. Bechtel, Michael C. Martin, Alex Zettl, James Analytis, and Feng Wang. Topological valley transport at bilayer graphene domain walls. *Nature*, 520(7549):650–655, April 2015.

[30] Liang Fu, C. L. Kane, and E. J. Mele. Topological Insulators in Three Dimensions. *Phys. Rev. Lett.*, 98(10):106803, March 2007.

[31] Xiangang Wan, Ari M. Turner, Ashvin Vishwanath, and Sergey Y. Savrasov. Topological semimetal and Fermi-arc surface states in the electronic structure of pyrochlore iridates. *Phys. Rev. B*, 83(20):205101, May 2011.

[32] Tiantian Zhang, Zhida Song, A. Alexandradinata, Hongming Weng, Chen Fang, Ling Lu, and Zhong Fang. Double-Weyl Phonons in Transition-Metal Monosilicides. *Phys. Rev. Lett.*, 120(1):016401, January 2018.

[33] Tomoki Ozawa, Hannah M. Price, Alberto Amo, Nathan Goldman, Mohammad Hafezi, Ling Lu, Mikael C. Rechtsman, David Schuster, Jonathan Simon, Oded Zilberberg, and Iacopo Carusotto. Topological photonics. *Rev. Mod. Phys.*, 91(1):015006, March 2019.

[34] Guancong Ma, Meng Xiao, and C. T. Chan. Topological phases in acoustic and mechanical systems. *Nat Rev Phys*, 1(4):281–294, April 2019.

[35] Long-Hua Wu and Xiao Hu. Scheme for Achieving a Topological Photonic Crystal by Using Dielectric Material. *Phys. Rev. Lett.*, 114(22):223901, June 2015.

[36] Rajesh Chaunsali, Feng Li, and Jinkyu Yang. Stress Wave Isolation by Purely Mechanical Topological Phononic Crystals. *Scientific Reports*, 6:30662, August 2016.

[37] Rajesh Chaunsali, Aman Thakkar, Eunho Kim, Panayotis G. Kevrekidis, and Jinkyu Yang. Demonstrating an in-situ topological band transition in cylindrical granular chains. *Physical Review Letters*, 119(2), July 2017.

[38] Ying Wu, Rajesh Chaunsali, Hiromi Yasuda, Kaiping Yu, and Jinkyu Yang. Dial-in Topological Metamaterials Based on Bistable Stewart Platform. *Scientific Reports*, 8(1):112, January 2018.

[39] Rajesh Chaunsali, Chun-Wei Chen, and Jinkyu Yang. Subwavelength and directional control of flexural waves in zone-folding induced topological plates. *Phys. Rev. B*, 97(5):054307, February 2018.

[40] Rajesh Chaunsali, Chun-Wei Chen, and Jinkyu Yang. Experimental demonstration of topological waveguiding in elastic plates with local resonators. *New J. Phys.*, 20(11):113036, November 2018.

[41] C. W. Groth, M. Wimmer, A. R. Akhmerov, J. Tworzydło, and C. W. J. Beenakker. Theory of the Topological Anderson Insulator. *Phys. Rev. Lett.*, 103(19):196805, November 2009.

[42] Jian Li, Rui-Lin Chu, J. K. Jain, and Shun-Qing Shen. Topological Anderson Insulator. *Phys. Rev. Lett.*, 102(13):136806, April 2009.

[43] Emil Prodan, Taylor L. Hughes, and B. Andrei Bernevig. Entanglement Spectrum of a Disordered Topological Chern Insulator. *Phys. Rev. Lett.*, 105(11):115501, September 2010.

[44] Paraj Titum, Netanel H. Lindner, Mikael C. Rechtsman, and Gil Refael. Disorder-Induced Floquet Topological Insulators. *Phys. Rev. Lett.*, 114(5):056801, February 2015.

[45] Changxu Liu, Wenlong Gao, Biao Yang, and Shuang Zhang. Disorder-Induced Topological State Transition in Photonic Metamaterials. *Phys. Rev. Lett.*, 119(18):183901, November 2017.

[46] Zhengyou Liu, Xixiang Zhang, Yiwei Mao, Y. Y. Zhu, Zhiyu Yang, C. T. Chan, and Ping Sheng. Locally Resonant Sonic Materials. *Science*, 289(5485):1734–1736, September 2000.

[47] Mahmoud I. Hussein, Michael J. Leamy, and Massimo Ruzzene. Dynamics of Phononic Materials and Structures: Historical Origins, Recent Progress, and Future Outlook. *Appl. Mech. Rev*, 66(4):040802–040802–38, May 2014.

[48] Muamer Kadic, Tiemo Bückmann, Robert Schittny, and Martin Wegener. Metamaterials beyond electromagnetism. *Rep. Prog. Phys.*, 76(12):126501, November 2013.

[49] Katia Bertoldi, Vincenzo Vitelli, Johan Christensen, and Martin van Hecke. Flexible mechanical metamaterials. *Nature Reviews Materials*, 2(11):17066, November 2017.

[50] M. Z. Hasan and C. L. Kane. Colloquium: Topological insulators. *Rev. Mod. Phys.*, 82(4):3045–3067, November 2010.

[51] Xiao-Liang Qi and Shou-Cheng Zhang. Topological insulators and superconductors. *Rev. Mod. Phys.*, 83(4):1057–1110, October 2011.

[52] Sebastian D. Huber. Topological mechanics. *Nature Physics*, 12:621–623, June 2016.

[53] Chen Fang, Matthew J. Gilbert, Xi Dai, and B. Andrei Bernevig. Multi-Weyl Topological Semimetals Stabilized by Point Group Symmetry. *Phys. Rev. Lett.*, 108(26):266802, June 2012.

[54] Su-Yang Xu, Ilya Belopolski, Nasser Alidoust, Madhab Neupane, Guang Bian, Chenglong Zhang, Raman Sankar, Guoqing Chang, Zhujun Yuan, Chi-Cheng Lee, Shin-Ming Huang, Hao Zheng, Jie Ma, Daniel S. Sanchez, BaoKai Wang, Arun Bansil, Fangcheng Chou, Pavel P. Shibayev, Hsin Lin, Shuang Jia, and M. Zahid Hasan. Discovery of a Weyl fermion semimetal and topological Fermi arcs. *Science*, 349(6248):613–617, August 2015.

[55] Alexey A. Soluyanov, Dominik Gresch, Zhijun Wang, QuanSheng Wu, Matthias Troyer, Xi Dai, and B. Andrei Bernevig. Type-II Weyl semimetals. *Nature*, 527(7579):495–498, November 2015.

[56] N. P. Armitage, E. J. Mele, and Ashvin Vishwanath. Weyl and Dirac semimetals in three-dimensional solids. *Rev. Mod. Phys.*, 90(1):015001, January 2018.

[57] Zhong Fang, Naoto Nagaosa, Kei S. Takahashi, Atsushi Asamitsu, Roland Mathieu, Takeshi Ogasawara, Hiroyuki Yamada, Masashi Kawasaki, Yoshinori Tokura, and Kiyoyuki Terakura. The Anomalous Hall Effect and Magnetic Monopoles in Momentum Space. *Science*, 302(5642):92–95, October 2003.

[58] Wen-Jie Chen, Meng Xiao, and C. T. Chan. Photonic crystals possessing multiple Weyl points and the experimental observation of robust surface states. *Nature Communications*, 7:13038, October 2016.

[59] H. B. Nielsen and Masao Ninomiya. The Adler-Bell-Jackiw anomaly and Weyl fermions in a crystal. *Physics Letters B*, 130(6):389–396, November 1983.

[60] Ling Lu, Liang Fu, John D. Joannopoulos, and Marin Soljačić. Weyl points and line nodes in gyroid photonic crystals. *Nature Photonics*, 7(4):294–299, April 2013.

[61] Ling Lu, Zhiyu Wang, Dexin Ye, Lixin Ran, Liang Fu, John D. Joannopoulos, and Marin Soljačić. Experimental observation of Weyl points. *Science*, 349(6248):622–624, August 2015.

[62] Guoqing Chang, Su-Yang Xu, Benjamin J. Wieder, Daniel S. Sanchez, Shin-Ming Huang, Ilya Belopolski, Tay-Rong Chang, Songtian Zhang, Arun Bansil, Hsin Lin, and M. Zahid Hasan. Unconventional Chiral Fermions and Large Topological Fermi Arcs in RhSi. *Phys. Rev. Lett.*, 119(20):206401, November 2017.

[63] Meng Xiao, Wen-Jie Chen, Wen-Yu He, and C. T. Chan. Synthetic gauge flux and Weyl points in acoustic systems. *Nature Physics*, 11(11):920–924, November 2015.

[64] Zhaoju Yang and Baile Zhang. Acoustic Type-II Weyl Nodes from Stacking Dimerized Chains. *Phys. Rev. Lett.*, 117(22):224301, November 2016.

[65] Feng Li, Xueqin Huang, Jiuyang Lu, Jiahong Ma, and Zhengyou Liu. Weyl points and Fermi arcs in a chiral phononic crystal. *Nature Physics*, 14(1):30–34, January 2018.

[66] Tingting Liu, Shengjie Zheng, Hongqing Dai, Dejie Yu, and Baizhan Xia. Acoustic semimetal with Weyl points and surface states. *arXiv preprint arXiv:1803.04284*, March 2018.

[67] Hao Ge, Xu Ni, Yuan Tian, Samit Kumar Gupta, Ming-Hui Lu, Xin Lin, Wei-Dong Huang, C. T. Chan, and Yan-Feng Chen. Experimental Observation of Acoustic Weyl Points and Topological Surface States. *Phys. Rev. Applied*, 10(1):014017, July 2018.

[68] Hailong He, Chunyin Qiu, Liping Ye, Xiangxi Cai, Xiying Fan, Manzhu Ke, Fan Zhang, and Zhengyou Liu. Topological negative refraction of surface acoustic waves in a Weyl phononic crystal. *Nature*, 560(7716):61–64, August 2018.

[69] Xiujuan Zhang, Meng Xiao, Ying Cheng, Ming-Hui Lu, and Johan Christensen. Topological sound. *Communications Physics*, 1(1):97, December 2018.

[70] Michel Fruchart, Seung-Yeol Jeon, Kahyun Hur, Vadim Cheianov, Ulrich Wiesner, and Vincenzo Vitelli. Soft self-assembly of Weyl materials for light and sound. *PNAS*, 115(16):E3655–E3664, April 2018.

[71] Yao-Ting Wang and Ya-Wen Tsai. Multiple Weyl and double-Weyl points in an elastic chiral lattice. *New J. Phys.*, 20(8):083031, August 2018.

[72] Pai Wang, Filippo Casadei, Sung Hoon Kang, and Katia Bertoldi. Locally resonant band gaps in periodic beam lattices by tuning connectivity. *Phys. Rev. B*, 91(2):020103, January 2015.

[73] Christopher S. Lefky, Brian Zucker, David Wright, Abdalla R. Nassar, Timothy W. Simpson, and Owen J. Hildreth. Dissolvable Supports in Powder Bed Fusion-Printed Stainless Steel. *3D Printing and Additive Manufacturing*, 4(1):3–11, March 2017.

[74] Xiaotian Shi, Rajesh Chaunsali, Feng Li, and Jinkyu Yang. Elastic Weyl Points and Surface Arc States in Three-Dimensional Structures. *Phys. Rev. Applied*, 12(2):024058, August 2019.

[75] Alexey A. Soluyanov, Dominik Gresch, Zhijun Wang, QuanSheng Wu, Matthias Troyer, Xi Dai, and B. Andrei Bernevig. Type-II Weyl semimetals. *Nature*, 527(7579):495–498, November 2015.

[76] Zhong Fang, Naoto Nagaosa, Kei S. Takahashi, Atsushi Asamitsu, Roland Mathieu, Takeshi Ogasawara, Hiroyuki Yamada, Masashi Kawasaki, Yoshinori Tokura, and Kiyoyuki Terakura. The Anomalous Hall Effect and Magnetic Monopoles in Momentum Space. *Science*, 302(5642):92–95, October 2003.

[77] Qiang Wang, Meng Xiao, Hui Liu, Shining Zhu, and C. T. Chan. Optical Interface States Protected by Synthetic Weyl Points. *Phys. Rev. X*, 7(3):031032, August 2017.

[78] Boyang Xie, Hui Liu, Hua Cheng, Zhengyou Liu, Shuqi Chen, and Jianguo Tian. Experimental Realization of Type-II Weyl Points and Fermi Arcs in Phononic Crystal. *Phys. Rev. Lett.*, 122(10):104302, March 2019.

[79] Barry Bradlyn, Jennifer Cano, Zhijun Wang, M. G. Vergniory, C. Felser, R. J. Cava, and B. Andrei Bernevig. Beyond Dirac and Weyl fermions: Unconventional quasiparticles in conventional crystals. *Science*, 353(6299):aaf5037, August 2016.

[80] Peizhe Tang, Quan Zhou, and Shou-Cheng Zhang. Multiple Types of Topological Fermions in Transition Metal Silicides. *Phys. Rev. Lett.*, 119(20):206402, November 2017.

[81] Ming-Li Chang, Meng Xiao, Wen-Jie Chen, and C. T. Chan. Multiple Weyl points and the sign change of their topological charges in woodpile photonic crystals. *Phys. Rev. B*, 95(12):125136, March 2017.

[82] Yan-Qing Zhu, Dan-Wei Zhang, Hui Yan, Ding-Yu Xing, and Shi-Liang Zhu. Emergent pseudospin-1 Maxwell fermions with a threefold degeneracy in optical lattices. *Phys. Rev. A*, 96(3):033634, September 2017.

[83] I. C. Fulga, L. Fallani, and M. Burrello. Geometrically protected triple-point crossings in an optical lattice. *Phys. Rev. B*, 97(12):121402, March 2018.

[84] Haiping Hu, Junpeng Hou, Fan Zhang, and Chuanwei Zhang. Topological Triply Degenerate Points Induced by Spin-Tensor-Momentum Couplings. *Phys. Rev. Lett.*, 120(24):240401, June 2018.

[85] H. Miao, T. T. Zhang, L. Wang, D. Meyers, A. H. Said, Y. L. Wang, Y. G. Shi, H. M. Weng, Z. Fang, and M. P. M. Dean. Observation of Double Weyl Phonons in Parity-Breaking FeSi. *Phys. Rev. Lett.*, 121(3):035302, July 2018.

[86] Daichi Takane, Zhiwei Wang, Seigo Souma, Kosuke Nakayama, Takechika Nakamura, Hikaru Oinuma, Yuki Nakata, Hideaki Iwasawa, Cephise Cacho, Timur Kim, Koji Horiba, Hiroshi Kumigashira, Takashi Takahashi, Yoichi Ando, and Takafumi Sato. Observation of Chiral Fermions with a Large Topological Charge and Associated Fermi-Arc Surface States in CoSi. *Phys. Rev. Lett.*, 122(7):076402, February 2019.

[87] Zhicheng Rao, Hang Li, Tiantian Zhang, Shangjie Tian, Chenghe Li, Binbin Fu, Cenyao Tang, Le Wang, Zhilin Li, Wenhui Fan, Jiajun Li, Yaobo Huang, Zhehong Liu, Youwen Long, Chen Fang, Hongming Weng, Youguo Shi, Hechang Lei, Yujie Sun, Tian Qian, and Hong Ding. Observation of unconventional chiral fermions with long Fermi arcs in CoSi. *Nature*, 567(7749):496–499, March 2019.

[88] Daniel S. Sanchez, Ilya Belopolski, Tyler A. Cochran, Xitong Xu, Jia-Xin Yin, Guoqing Chang, Weiwei Xie, Kaustuv Manna, Vicky Süß, Cheng-Yi Huang, Nasser Alidoust, Daniel Multer, Songtian S. Zhang, Nana Shumiya, Xirui Wang, Guang-Qiang Wang, Tay-Rong Chang, Claudia Felser, Su-Yang Xu, Shuang Jia, Hsin Lin, and M. Zahid Hasan. Topological chiral crystals with helicoid-arc quantum states. *Nature*, 567(7749):500–505, March 2019.

[89] Niels B. M. Schröter, Ding Pei, Maia G. Vergniory, Yan Sun, Kaustuv Manna, Fernando de Juan, Jonas A. Krieger, Vicky Süss, Marcus Schmidt, Pavel Dudin, Barry Bradlyn, Timur K. Kim, Thorsten Schmitt, Cephise Cacho, Claudia Felser, Vladimir N. Strocov, and Yulin Chen. Chiral topological semimetal with multifold band crossings and long Fermi arcs. *Nat. Phys.*, 15(8):759–765, August 2019.

[90] Yihao Yang, Hong-xiang Sun, Jian-ping Xia, Haoran Xue, Zhen Gao, Yong Ge, Ding Jia, Shou-qi Yuan, Yidong Chong, and Baile Zhang. Topological triply degenerate point with double Fermi arcs. *Nat. Phys.*, 15(7):645–649, July 2019.

[91] R. Shen, L. B. Shao, Baigeng Wang, and D. Y. Xing. Single Dirac cone with a flat band touching on line-centered-square optical lattices. *Phys. Rev. B*, 81(4):041410, January 2010.

[92] D. Bercioux, D. F. Urban, H. Grabert, and W. Häusler. Massless Dirac-Weyl fermions in a ${\mathcal{T}}_{3}$ optical lattice. *Phys. Rev. A*, 80(6):063603, December 2009.

[93] Dmitry Green, Luiz Santos, and Claudio Chamon. Isolated flat bands and spin-1 conical bands in two-dimensional lattices. *Phys. Rev. B*, 82(7):075104, August 2010.

[94] W. Beugeling, J. C. Everts, and C. Morais Smith. Topological phase transitions driven by next-nearest-neighbor hopping in two-dimensional lattices. *Phys. Rev. B*, 86(19):195129, November 2012.

[95] Rui Yu, Xiao Liang Qi, Andrei Bernevig, Zhong Fang, and Xi Dai. Equivalent expression of ${\mathbb{Z}}_{2}$ topological invariant for band insulators using the non-Abelian Berry connection. *Phys. Rev. B*, 84(7):075119, August 2011.

[96] Chen Fang, Matthew J. Gilbert, and B. Andrei Bernevig. Bulk topological invariants in noninteracting point group symmetric insulators. *Phys. Rev. B*, 86(11):115112, September 2012.

[97] Jun Mei, Ying Wu, C. T. Chan, and Zhao-Qing Zhang. First-principles study of Dirac and Dirac-like cones in phononic and photonic crystals. *Phys. Rev. B*, 86(3):035141, July 2012.

[98] Hongfei Zhu and Fabio Semperlotti. Double-Zero-Index Structural Phononic Waveguides. *Phys. Rev. Applied*, 8(6):064031, December 2017.

[99] Xiaotian Shi and Jinkyu Yang. Spin-1 Weyl point and surface arc state in a chiral phononic crystal. *Phys. Rev. B*, 101(21):214309, June 2020.

[100] Zheng Wang, Yidong Chong, J. D. Joannopoulos, and Marin Soljačić. Observation of unidirectional backscattering-immune topological electromagnetic states. *Nature*, 461(7265):772–775, October 2009.

[101] M. Hafezi, S. Mittal, J. Fan, A. Migdall, and J. M. Taylor. Imaging topological edge states in silicon photonics. *Nature Photonics*, 7(12):1001–1005, December 2013.

[102] Tzuhsuan Ma and Gennady Shvets. All-Si valley-Hall photonic topological insulator. *New J. Phys.*, 18(2):025012, February 2016.

[103] Zhaoju Yang, Fei Gao, Xihang Shi, Xiao Lin, Zhen Gao, Yidong Chong, and Baile Zhang. Topological Acoustics. *Phys. Rev. Lett.*, 114(11):114301, March 2015.

[104] Cheng He, Xu Ni, Hao Ge, Xiao-Chen Sun, Yan-Bin Chen, Ming-Hui Lu, Xiao-Ping Liu, and Yan-Feng Chen. Acoustic topological insulator and robust one-way sound transport. *Nature Physics*, 12(12):1124–1129, December 2016.

[105] Roman Süsstrunk and Sebastian D. Huber. Observation of phononic helical edge states in a mechanical topological insulator. *Science*, 349(6243):47–50, July 2015.

[106] Lisa M. Nash, Dustin Kleckner, Alismari Read, Vincenzo Vitelli, Ari M. Turner, and William T. M. Irvine. Topological mechanics of gyroscopic metamaterials. *PNAS*, 112(47):14495–14500, November 2015.

[107] Javier Vila, Raj Kumar Pal, and Massimo Ruzzene. Observation of topological valley modes in an elastic hexagonal lattice. *Phys. Rev. B*, 96(13):134307, October 2017.

[108] H. Chen, H. Nassar, and G. L. Huang. A study of topological effects in 1D and 2D mechanical lattices. *Journal of the Mechanics and Physics of Solids*, 117:22–36, August 2018.

[109] H. Chen, H. Nassar, A. N. Norris, G. K. Hu, and G. L. Huang. Elastic quantum spin Hall effect in kagome lattices. *Phys. Rev. B*, 98(9):094302, September 2018.

[110] Li Xin, Yu Siyuan, Liu Harry, Lu Minghui, and Chen Yanfeng. Topological mechanical metamaterials: A brief review. *Current Opinion in Solid State and Materials Science*, 24(5):100853, October 2020.

[111] Hua Jiang, Lei Wang, Qing-feng Sun, and X. C. Xie. Numerical study of the topological Anderson insulator in HgTe/CdTe quantum wells. *Phys. Rev. B*, 80(16):165316, October 2009.

[112] H.-M. Guo, G. Rosenberg, G. Refael, and M. Franz. Topological Anderson Insulator in Three Dimensions. *Phys. Rev. Lett.*, 105(21):216601, November 2010.

[113] Juntao Song and Emil Prodan. AIII and BDI topological systems at strong disorder. *Phys. Rev. B*, 89(22):224203, June 2014.

[114] Alexander Altland, Dmitry Bagrets, Lars Fritz, Alex Kamenev, and Hanno Schmiedt. Quantum Criticality of Quasi-One-Dimensional Topological Anderson Insulators. *Phys. Rev. Lett.*, 112(20):206602, May 2014.

[115] Ian Mondragon-Shem, Taylor L. Hughes, Juntao Song, and Emil Prodan. Topological Criticality in the Chiral-Symmetric AIII Class at Strong Disorder. *Phys. Rev. Lett.*, 113(4):046802, July 2014.

[116] Eric J. Meier, Fangzhao Alex An, Alexandre Dauphin, Maria Maffei, Pietro Massignan, Taylor L. Hughes, and Bryce Gadway. Observation of the topological Anderson insulator in disordered atomic wires. *Science*, 362(6417):929–933, November 2018.

[117] Simon Stützer, Yonatan Plotnik, Yaakov Lumer, Paraj Titum, Netanel H. Lindner, Mordechai Segev, Mikael C. Rechtsman, and Alexander Szameit. Photonic topological Anderson insulators. *Nature*, 560(7719):461–465, August 2018.

[118] Farzad Zangeneh-Nejad and Romain Fleury. Disorder-Induced Signal Filtering with Topological Metamaterials. *Advanced Materials*, 32(28):2001034, 2020.

[119] W. P. Su, J. R. Schrieffer, and A. J. Heeger. Solitons in Polyacetylene. *Phys. Rev. Lett.*, 42(25):1698–1701, June 1979.

[120] Filippo Cardano, Alessio D'Errico, Alexandre Dauphin, Maria Maffei, Bruno Piccirillo, Corrado de Lisio, Giulio De Filippis, Vittorio Cataudella, Enrico Santamato, Lorenzo Marrucci, Maciej Lewenstein, and Pietro Massignan. Detection of Zak phases and topological invariants in a chiral quantum walk of twisted photons. *Nature Communications*, 8:15516, June 2017.

[121] Maria Maffei, Alexandre Dauphin, Filippo Cardano, Maciej Lewenstein, and Pietro Massignan. Topological characterization of chiral models through their long time dynamics. *New J. Phys.*, 20(1):013023, January 2018.

[122] Roman Süsstrunk and Sebastian D. Huber. Classification of topological phonons in linear mechanical metamaterials. *PNAS*, 113(33):E4767–E4775, August 2016.

[123] Andrea Crisanti, Giovanni Paladin, and Angelo Vulpiani. *Products of Random Matrices*. Springer-Verlag, Berlin, 1993.

[124] John A. Scales and Erik S. Van Vleck. Lyapunov Exponents and Localization in Randomly Layered Media. *Journal of Computational Physics*, 133(1):27–42, May 1997.

[125] A. MacKinnon and B. Kramer. One-Parameter Scaling of Localization Length and Conductance in Disordered Systems. *Phys. Rev. Lett.*, 47(21):1546–1549, November 1981.

[126] A. MacKinnon and B. Kramer. The scaling theory of electrons in disordered solids: Additional numerical results. *Z. Physik B - Condensed Matter*, 53(1):1–13, March 1983.

[127] János K. Asbóth, László Oroszlány, and András Pályi. *A Short Course on Topological Insulators*. Springer, Cham, 2016.

[128] Marc Serra-Garcia, Valerio Peri, Roman Süsstrunk, Osama R. Bilal, Tom Larsen, Luis Guillermo Villanueva, and Sebastian D. Huber. Observation of a phononic quadrupole topological insulator. *Nature*, 555(7696):342–345, March 2018.

[129] Ze-Guo Chen, Licheng Wang, Guanqing Zhang, and Guancong Ma. Chiral Symmetry Breaking of Tight-Binding Models in Coupled Acoustic-Cavity Systems. *Phys. Rev. Applied*, 14(2):024023, August 2020.

[130] Zhi-Qiang Zhang, Bing-Lan Wu, Juntao Song, and Hua Jiang. Topological Anderson insulator in electric circuits. *Phys. Rev. B*, 100(18):184202, November 2019.

[131] Xiaotian Shi, Ioannis Kiorpelidis, Rajesh Chaunsali, Vassos Achilleos, Georgios Theocharis, and Jinkyu Yang. Disorder-induced topological phase transition in a one-dimensional mechanical system. *Phys. Rev. Research*, 3(3):033012, July 2021.

[132] D. J. Thouless, M. Kohmoto, M. P. Nightingale, and M. den Nijs. Quantized Hall Conductance in a Two-Dimensional Periodic Potential. *Phys. Rev. Lett.*, 49(6):405–408, August 1982.

[133] A. Rycerz, J. Tworzydło, and C. W. J. Beenakker. Valley filter and valley valve in graphene. *Nature Physics*, 3(3):172–175, March 2007.

[134] Di Xiao, Wang Yao, and Qian Niu. Valley-Contrasting Physics in Graphene: Magnetic Moment and Topological Transport. *Phys. Rev. Lett.*, 99(23):236809, December 2007.

[135] Si-Yuan Yu, Cheng He, Zhen Wang, Fu-Kang Liu, Xiao-Chen Sun, Zheng Li, Hai-Zhou Lu, Ming-Hui Lu, Xiao-Ping Liu, and Yan-Feng Chen. Elastic pseudospin transport for integratable topological phononic circuits. *Nat Commun*, 9(1):3072, August 2018.

[136] Jian Li, Rui-Lin Chu, J. K. Jain, and Shun-Qing Shen. Topological Anderson Insulator. *Phys. Rev. Lett.*, 102(13):136806, April 2009.

[137] Hua Jiang, Lei Wang, Qing-feng Sun, and X. C. Xie. Numerical study of the topological Anderson insulator in HgTe/CdTe quantum wells. *Phys. Rev. B*, 80(16):165316, October 2009.

[138] J. H. Bardarson, P. W. Brouwer, and J. E. Moore. Aharonov-Bohm Oscillations in Disordered Topological Insulator Nanowires. *Phys. Rev. Lett.*, 105(15):156803, October 2010.

[139] Kentaro Nomura and Naoto Nagaosa. Surface-Quantized Anomalous Hall Current and the Magnetoelectric Effect in Magnetically Disordered Topological Insulators. *Phys. Rev. Lett.*, 106(16):166802, April 2011.

[140] Gerald Schubert, Holger Fehske, Lars Fritz, and Matthias Vojta. Fate of topological-insulator surface states under strong disorder. *Phys. Rev. B*, 85(20):201105, May 2012.

[141] Juntao Song, Haiwen Liu, Hua Jiang, Qing-feng Sun, and X. C. Xie. Dependence of topological Anderson insulator on the type of disorder. *Phys. Rev. B*, 85(19):195125, May 2012.

[142] Koji Kobayashi, Tomi Ohtsuki, and Ken-Ichiro Imura. Disordered Weak and Strong Topological Insulators. *Phys. Rev. Lett.*, 110(23):236803, June 2013.

[143] Bing Yang, Bing Yang, Hongfang Zhang, Hongfang Zhang, Qiang Shi, Tong Wu, Yong Ma, Zengtao Lv, Xia Xiao, Ruixin Dong, Ruixin Dong, Xunling Yan, Xunling Yan, and Xiangdong Zhang. Details of the topological state transition induced by gradually increased disorder in photonic Chern insulators. *Opt. Express, OE*, 28(21):31487–31498, October 2020.

[144] Gui-Geng Liu, Yihao Yang, Xin Ren, Haoran Xue, Xiao Lin, Yuan-Hang Hu, Hong-xiang Sun, Bo Peng, Peiheng Zhou, Yidong Chong, and Baile Zhang. Topological Anderson Insulator in Disordered Photonic Crystals. *Phys. Rev. Lett.*, 125(13):133603, September 2020.

[145] Hongfang Zhang, Wenjie Sui, Yu Zhang, Gangcheng Liu, Qiang Shi, Zengtao Lv, Dong Zhang, Chuicai Rong, and Bing Yang. Disorder-Driven Collapse of Topological Phases in Photonic Topological Insulator. *physica status solidi (b)*, n/a(n/a):2200214, May 2022.

[146] Weixuan Zhang, Deyuan Zou, Qingsong Pei, Wenjing He, Jiacheng Bao, Houjun Sun, and Xiangdong Zhang. Experimental Observation of Higher-Order Topological Anderson Insulators. *Phys. Rev. Lett.*, 126(14):146802, April 2021.

[147] Hui Liu, Boyang Xie, Haonan Wang, Wenwei Liu, Zhancheng Li, Hua Cheng, Jianguo Tian, Zhengyou Liu, and Shuqi Chen. Acoustic topological Anderson insulators. *arXiv preprint arXiv:2111.06520*, November 2021.

[148] Long-Hua Wu and Xiao Hu. Topological Properties of Electrons in Honeycomb Lattice with Detuned Hopping Energy. *Sci Rep*, 6(1):24347, April 2016.

[149] Huaqing Huang and Feng Liu. Quantum Spin Hall Effect and Spin Bott Index in a Quasicrystal Lattice. *Phys. Rev. Lett.*, 121(12):126401, September 2018.

[150] Huaqing Huang and Feng Liu. Theory of spin Bott index for quantum spin Hall states in nonperiodic systems. *Phys. Rev. B*, 98(12):125130, September 2018.

[151] Antonin Coutant, Vassos Achilleos, Olivier Richoux, Georgios Theocharis, and Vincent Pagneux. Robustness of topological corner modes against disorder with application to acoustic networks. *Phys. Rev. B*, 102(21):214204, December 2020.

[152] Yuanchen Deng, Hao Ge, Yuan Tian, Minghui Lu, and Yun Jing. Observation of zone folding induced acoustic topological insulators and the role of spin-mixing defects. *Phys. Rev. B*, 96(18):184305, November 2017.

[153] P. W. Anderson. Absence of Diffusion in Certain Random Lattices. *Phys. Rev.*, 109(5):1492–1505, March 1958.

[154] Raj Kumar Pal, Javier Vila, Michael Leamy, and Massimo Ruzzene. Amplitude-dependent topological edge states in nonlinear phononic lattices. *Phys. Rev. E*, 97(3):032209, March 2018.

[155] Rajesh Chaunsali and Georgios Theocharis. Self-induced topological transition in phononic crystals by nonlinearity management. *Phys. Rev. B*, 100(1):014302, July 2019.

[156] Amir Darabi and Michael J. Leamy. Tunable Nonlinear Topological Insulator for Acoustic Waves. *Phys. Rev. Applied*, 12(4):044030, October 2019.

[157] David D. J. M. Snee and Yi-Ping Ma. Edge solitons in a nonlinear mechanical topological insulator. *Extreme Mechanics Letters*, 30:100487, July 2019.

[158] Rajesh Chaunsali, Haitao Xu, Jinkyu Yang, Panayotis G. Kevrekidis, and Georgios Theocharis. Stability of topological edge states under strong nonlinear effects. *Phys. Rev. B*, 103(2):024106, January 2021.

[159] Joshua R. Tempelman, Kathryn H. Matlack, and Alexander F. Vakakis. Topological protection in a strongly nonlinear interface lattice. *Phys. Rev. B*, 104(17):174306, November 2021.

[160] David J. Apigo, Kai Qian, Camelia Prodan, and Emil Prodan. Topological edge modes by smart patterning. *Phys. Rev. Materials*, 2(12):124203, December 2018.

[161] David J. Apigo, Wenting Cheng, Kyle F. Dobiszewski, Emil Prodan, and Camelia Prodan. Observation of Topological Edge Modes in a Quasiperiodic Acoustic Waveguide. *Phys. Rev. Lett.*, 122(9):095501, March 2019.

[162] Raj Kumar Pal, Matheus I. N. Rosa, and Massimo Ruzzene. Topological bands and localized vibration modes in quasiperiodic beams. *New J. Phys.*, 21(9):093017, September 2019.

[163] Matheus I. N. Rosa, Raj Kumar Pal, José R. F. Arruda, and Massimo Ruzzene. Edge States and Topological Pumping in Spatially Modulated Elastic Lattices. *Phys. Rev. Lett.*, 123(3):034301, July 2019.

[164] Di Zhou, Leyou Zhang, and Xiaoming Mao. Topological Boundary Floppy Modes in Quasicrystals. *Phys. Rev. X*, 9(2):021054, June 2019.

[165] Yiwei Xia, Alper Erturk, and Massimo Ruzzene. Topological Edge States in Quasiperiodic Locally Resonant Metastructures. *Phys. Rev. Applied*, 13(1):014023, January 2020.

[166] Wenting Cheng, Emil Prodan, and Camelia Prodan. Experimental Demonstration of Dynamic Topological Pumping across Incommensurate Bilayered Acoustic Metamaterials. *Phys. Rev. Lett.*, 125(22):224301, November 2020.

[167] Marc Martí-Sabaté and Dani Torrent. Edge modes for flexural waves in quasi-periodic linear arrays of scatterers. *APL Materials*, 9(8):081107, August 2021.

[168] Matheus I. N. Rosa, Yuning Guo, and Massimo Ruzzene. Exploring topology of 1D quasiperiodic metastructures through modulated LEGO resonators. *Appl. Phys. Lett.*, 118(13):131901, March 2021.

[169] Matheus I. N. Rosa, Massimo Ruzzene, and Emil Prodan. Topological gaps by twisting. *Commun Phys*, 4(1):1–10, June 2021.

[170] Yunhong Liao and Xiaoming Zhou. Topological Pumping in Doubly Modulated Mechanical Systems. *Phys. Rev. Applied*, 17(3):034076, March 2022.

[171] Huaqing Huang, Jiahao Fan, Dexin Li, and Feng Liu. Generic Orbital Design of Higher-Order Topological Quasicrystalline Insulators with Odd Five-Fold Rotation Symmetry. *Nano Lett.*, 21(16):7056–7062, August 2021.

[172] János K. Asbóth, László Oroszlány, and András Pályi. Berry phase, chern number. In *A Short Course on Topological Insulators: Band Structure and Edge States in One and Two Dimensions*, pages 23–44. Springer International Publishing, Cham, 2016.

[173] L. Balicas, S. Nakatsuji, Y. Machida, and S. Onoda. Anisotropic Hysteretic Hall Effect and Magnetic Control of Chiral Domains in the Chiral Spin States of ${\mathrm{Pr}}_{2}{\mathrm{Ir}}_{2}{\mathrm{O}}_{7}$. *Phys. Rev. Lett.*, 106(21):217204, May 2011.

[174] S. P. Beeby, M. J. Tudor, and N. M. White. Energy harvesting vibration sources for microsystems applications. *Meas. Sci. Technol.*, 17(12):R175–R195, October 2006.

[175] Yiqun Ding, Zhengyou Liu, Chunyin Qiu, and Jing Shi. Metamaterial with Simultaneously Negative Bulk Modulus and Mass Density. *Phys. Rev. Lett.*, 99(9):093904, August 2007.

[176] Jiuyang Lu, Chunyin Qiu, Liping Ye, Xiying Fan, Manzhu Ke, Fan Zhang, and Zhengyou Liu. Observation of topological valley transport of sound in sonic crystals. *Nature Physics*, 13(4):369–374, April 2017.

[177] B. Q. Lv, S. Muff, T. Qian, Z. D. Song, S. M. Nie, N. Xu, P. Richard, C. E. Matt, N. C. Plumb, L. X. Zhao, G. F. Chen, Z. Fang, X. Dai, J. H. Dil, J. Mesot, M. Shi, H. M. Weng, and H. Ding. Observation of Fermi-Arc Spin Texture in TaAs. *Phys. Rev. Lett.*, 115(21):217601, November 2015.

[178] Binayak Mukherjee, Eleonora Isotta, Carlo Fanciulli, Narges Ataollahi, and Paolo Scardi. Topological Anderson Insulator in Cation-Disordered Cu2ZnSnS4. *Nanomaterials*, 11(10):2595, October 2021.

[179] José Sánchez-Dehesa, Victor M. Garcia-Chocano, Daniel Torrent, Francisco Cervera, Suitberto Cabrera, and Francisco Simon. Noise control by sonic crystal barriers made of recycled materials. *The Journal of the Acoustical Society of America*, 129(3):1173–1183, March 2011.